The Role of Non-Bonding Interactions and Bonding Schemes in the Structure and Properties of Multi-Component Polymer Systems

A Dissertation presented for the

Doctor of Philosophy

Degree

The University of Tennessee, Knoxville

Caleb Will Dyer

August 2012

DEDICATION

Dedicated to my son

Andrew Edward Dyer

And to the memory of my Grandfathers,

Duane Edward Dyer

and

Robert Darrell Smith

"In my Father's House are many mansions:

if it were not so, I would have told you.

I go to prepare a place for you." –John 14:2

ACKNOWLEDGEMENTS

This work would not have been possible without my advisor, Professor Mark Dadmun. He has been very patient and kind throughout my graduate career. I will forever be indebted for his understanding and guidance throughout graduate school. I would also like to thank Professor Jimmy Mays, Professor Joe Bozell, and Professor RJ Hinde for their support throughout this work. Others I would like to thank: Dr. Xiaojun Wang, Dr. Dias Linton, Dr. Nathan Henry, Dr. Rujul Mehta, Dr. Sudesh Kamath, Dr. Yin Wen, Dr. Huipeng Chen, Dr. Dilru Ratneweera, Dr. Paraskevi Driva, Dr. Scott Sides, Dr. Bobby Sumpter, Brent Magnusson, Dr. Josh Abbott, Dr. Patrick Moehlen, Dr. Royce Dansby-Sparks, Brad Miller, Lesley Thompson, Adam Imel, Brian Bachner, Dana Algaier, Say Lee Teh, Onome Swader, and Dr. Nick Vence.

I want to thank my family: My father and mother who have worked so hard for so many years to provide me with the opportunities to succeed and be happy while asking for so little in return. From them I have learned that, even though life does not always go as planned, an open heart will always find family and love. My sister, Charlie, who continues to be a positive influence in my life, and her husband Alex with whom I have many similar interest (such as a good, long trail run). My brother, Lou, who is very different than me yet, in many ways the same and loves me anyway and my sister Canaan who we all love so much. I want to show my love and gratitude to all of my family and friends back home where I found true appreciation of rural life in the North Georgia Mountains. There, I learned how to slow down and appreciate the simpler things in life:

the kindness and giving heart of a neighbor, a cold swimming hole on a hot summer's day, and the value of a hard day's work.

Most of all I want to thank my wife, Lisa, for her love and support throughout graduate school. I would not have made it through without her. Moreover, our son Andrew is the light of our life and for that I could never thank her enough.

ABSTRACT

This dissertation addresses three aspects of multi-component polymer systems. Chapter 2 details work on understanding the effect of precise polymeric structure on the phase behavior of blends containing cellulose acetate chains with different levels of acetate substitution. The difference in degree substitution (Delta DS) between the two components in the blend is systematically changed from .06 to .63, where each blend is found to be partially miscible. The samples containing higher acetate content demonstrate decreased miscibility as Delta DS increases. The sample with the most hydroxyl groups, however, has greater miscibility than samples of similar Delta DS, but fewer hydroxyl groups, indicating that hydroxyl groups promote mixing through favorable hydrogen bonding between blend components, highlighting the significant impact that specific interactions have on the miscibility of cellulose acetate blends.

The effect of non-bonding interactions is further investigated in Chapter 3, detailing the impact of thermodynamic interactions on the dynamics of a series of homopolymer/copolymer blends of 90% poly(methyl methacrylate) and 10% poly(methyl methacrylate)-co-poly(styrene). The copolymer composition varies from 60% to 90% MMA, effectively tuning the blend's thermodynamic interactions. The analysis indicates that the thermodynamic interactions in the system significantly impact copolymer dynamics. Comparison to the Lodge-McLeish model indicates that the local environment around the copolymer is richer in styrene than the model predicts. These homopolymer/copolymer blends indicate that the local composition and dynamics are significantly impacted by the repulsive interactions between styrene and methyl

methacrylate. These results emphasize the importance of thermodynamic interactions on the dynamics of miscible homopolymer/copolymer blends.

Chapter 4 further explores structure-property relationships of multi-component polymer systems utilizing neat polystyrene (PS)-polyisoprene (PI) block copolymers. The volume fraction of PS, PI, and molecular weight are held constant, varying the connectivity of the components from a linear PS-PI diblock copolymer to three different miktoarm star architectures: PS2-PI, PS-PI2, and PS2-PI2. The investigation indicates a change in morphological features due to excluded volume effects at the junction point of the star. Experimentally observed morphologies for different chain architectures are generally consistent with self-consistent field theory simulations, and agree with analytical theory predictions that account for architectural and conformational asymmetry.

TABLE OF CONTENTS

LIST OF TABLES

Table Page

LIST OF FIGURES

CHAPTER 1:INTRODUCTION

Polymeric applications are being integrated into our daily lives in increasingly frequent and sophisticated ways. The need for ever-improving products has driven research and development in both industrial and academic settings. It was realized in the latter part of the last century that creating chemically new polymers was a cost prohibitive endeavor. Blending two polymers, however, offers an economically feasible alternative due, in part, to the reduced capital expense of an R&D effort that uses previously existing polymers. The advantage of blending two polymers together is that the property profile of the blend resembles a combination of the property profiles of each of the two components, allowing tailored properties at relatively low cost. In rapidly emerging markets and changing technology, polymer blends offer a faster response than the R&D involved in new monomer production and scale-up.

Despite their vast success in many applications, polymer blends have drawbacks that are especially complex and difficult to overcome. Top among these drawbacks is the incompatibility involved in blending two chemically different components together. An incompatible blend experiences phase separation giving coarse phase morphologies with weak interfaces between the two phases. This leads to inferior physical properties such as brittleness and poor adhesion. One method employed to overcome this problem involves covalently bonding the two incompatible ends together to create a block copolymer. When the block copolymer is added to the blend it may act as a compatibilizer between the two phases, leading to improved properties. The ability of a block copolymer to make an otherwise incompatible blend into a material with mechanically useful properties has spurred much research in this area of polymer science.

Another aspect of block copolymers that is unique in the polymer world is their ability to self-organize into highly ordered systems leading to interesting and useful properties. In this way, block copolymers have found great utility as thermoplastic elastomers (TPEs). As compatibilizers[1-4] and as TPEs,[5,6] the block copolymer industry has experienced remarkable growth and commercial importance.

From the short discussion above, one can see that copolymers and polymer blends have enjoyed much growth and success in the past few decades. Many questions remain, however, regarding the effect that one component has on the dynamics and structure of the other component when combined (covalently or as a blend). The remaining body of this work will address several topics that are still unknown in the structure and properties of polymer blends and block copolymers. Chapter 2 will explore the structure-property relationships of a blend of two chemically different components. Specifically, the impact of non-bonding interactions on the miscibility of the two components in the blend will be examined and discussed. Chapter 3 will continue to investigate the impact of non-bonding interactions, focusing on the role thermodynamic interactions play in the segmental dynamics of a homopolymer/copolymer blend. Chapter 4 further explores the structure-property relationship of a series of copolymers where the connectivity is varied in each sample to determine the impact of this variable on the morphology of the resultant block copolymer.

1.2 Polymer Blends and Phase Behavior

Natural polymers provided some of the earliest polymer blend applications. Natural polymers (e.g. natural rubber, cellulose, etc.) were first combined with other materials to achieve desired coatings and adhesives. For instance, in the early 1900's, the

physical properties of brittle phonograph records were improved when phenolic thermosetting polymers were blended with natural rubber. One of the first synthetic blends produced commercially was poly(vinyl chloride) and butadiene-acrylonitrile (NBR). The addition of the butadiene-acrylonitrile elastomers to the PVC acts to form a permanently plasticized PVC. This blend is still used today as non-latex gloves, automotive transmission belts, and printer rollers, among other uses.

In the late 1960's, interest in polymer blends increased dramatically. This is largely due to the advent of miscible polymer blends. Before this time, miscibility of polymer blends was thought to be impossible due to the very small mixing entropy of long-chain molecules. In 1966, however, General Electric commercialized the poly(2,6,-dimethyl-1,4-phenylene oxide)(PPO)/polystyrene blend under the trade name Noryl. The PPO/polystyrene blend is miscible due to the dispersive interaction between the phenyl groups of the two polymers.[7] This results in a property profile of the blend that is intermediate between that of the components.[8] The addition of PPO to polystyrene improves the impact resistance and the tensile strength. The addition of polystyrene to PPO improves polymer processing and flammability resistance of polystyrene. The price/performance profile varies with blend composition, making this blend highly successful from a commercial standpoint in that simply varying the composition can produce a variety of products. This initiated interest in other blends that have the potential to make a range of products using a blend of existing polymers. Whereas before the commercialization of the PPO/polystyrene blend miscibility was largely thought to be impossible, it was soon realized that miscibility of polymer blends is much more

prevalent than initially believed. This triggered increased commercial and academic interest in polymer blend behavior.

It is important to address the definition of miscibility. Generally, when the properties of the blend approach those expected of a homogenously mixed blend, the system is considered miscible. A blend is considered partially miscible if there exists phase separation but each phase contains a sufficient amount of the other polymer to alter the properties of that phase relative to the properties of a fully immiscible system (e.g. scattering length density or glass transition temperature). Thermodynamic relationships describe the criteria that constitute miscibility.

The most important thermodynamic relationship that determines the phase behavior of two chemically different components is the change in free energy of mixing:

$$\Delta G_m = \Delta H_m - T\Delta S_m \qquad (1.1)$$

where ΔG_m is Gibbs free energy of mixing, ΔH_m is the enthalpy of mixing (heat of mixing) and ΔS_m is the entropy of mixing. For a blend to be miscible, ΔG_m must be less than 0. When considering small-molecule or low molecular weight mixtures, the most important factor leading to miscibility is the combinatorial entropy contribution as it is very large for these mixtures. Long-chain molecules, however, have a very small entropy of mixing. This leads to the enthalpy of mixing being the dominant feature in determining miscibility. For most polymers the enthalpy of mixing is positive; resulting in immiscibility in most polymer blends. While $\Delta G_m <$ zero is necessary, it is not the only requirement for miscibility to be achieved. The second derivative of the free energy of mixing (Equation 1.2) must be greater than zero as well.

$$\left(\frac{\partial^2 \Delta G_m}{\partial \varphi_i^2}\right)_{T,P} > 0 \qquad (1.2)$$

A negative $\frac{\partial^2 \Delta G_m}{\partial \varphi_i^2}$, however, (despite $\Delta G_m < 0$) yields an area of the phase diagram where the mixture separates into two phases, where phase 1 is rich in polymer A and phase 2 is rich in polymer B. The volume fractions of each phase is represented in Equation 1.2 by φ. The relationship between ΔG_m and T in equation 1.1 dictates that increasing temperature in small molecule mixtures tends to lead to greater miscibility. In large molecules, the small $T\Delta S_m$ contribution means other factors dominate the phase behavior, such as a temperature dependent ΔH_m, which may lead to decreasing miscibility with increasing temperature. For this reason, polymer-polymer mixtures commonly exhibit lower critical solution temperatures. This behavior is illustrated in Figure 1.1. The equilibrium phase boundary between the one phase and two-phase region is given by the binodal line; the solid line in Figure 1.1b. The binodal line defines where the chemical potentials of the two phases are equal, and is represented

$$\mu_1 = \mu_2 \qquad (1.3)$$

where 1 and 2 represent the two phases. The slope of a plot of Gibbs free energy with respect to composition gives the chemical potential and is shown as the double tangent to the ΔG_m curve in Figure 1.1.[9,10] If the molecular weights of the two components are similar, the phase diagram will be symmetric, as shown in this figure. With phase separation, the solid binodal line in Figure 1.1b defines the composition of the two coexisting phases. The dashed line is the spinodal line, representing the boundary between the metastable and unstable

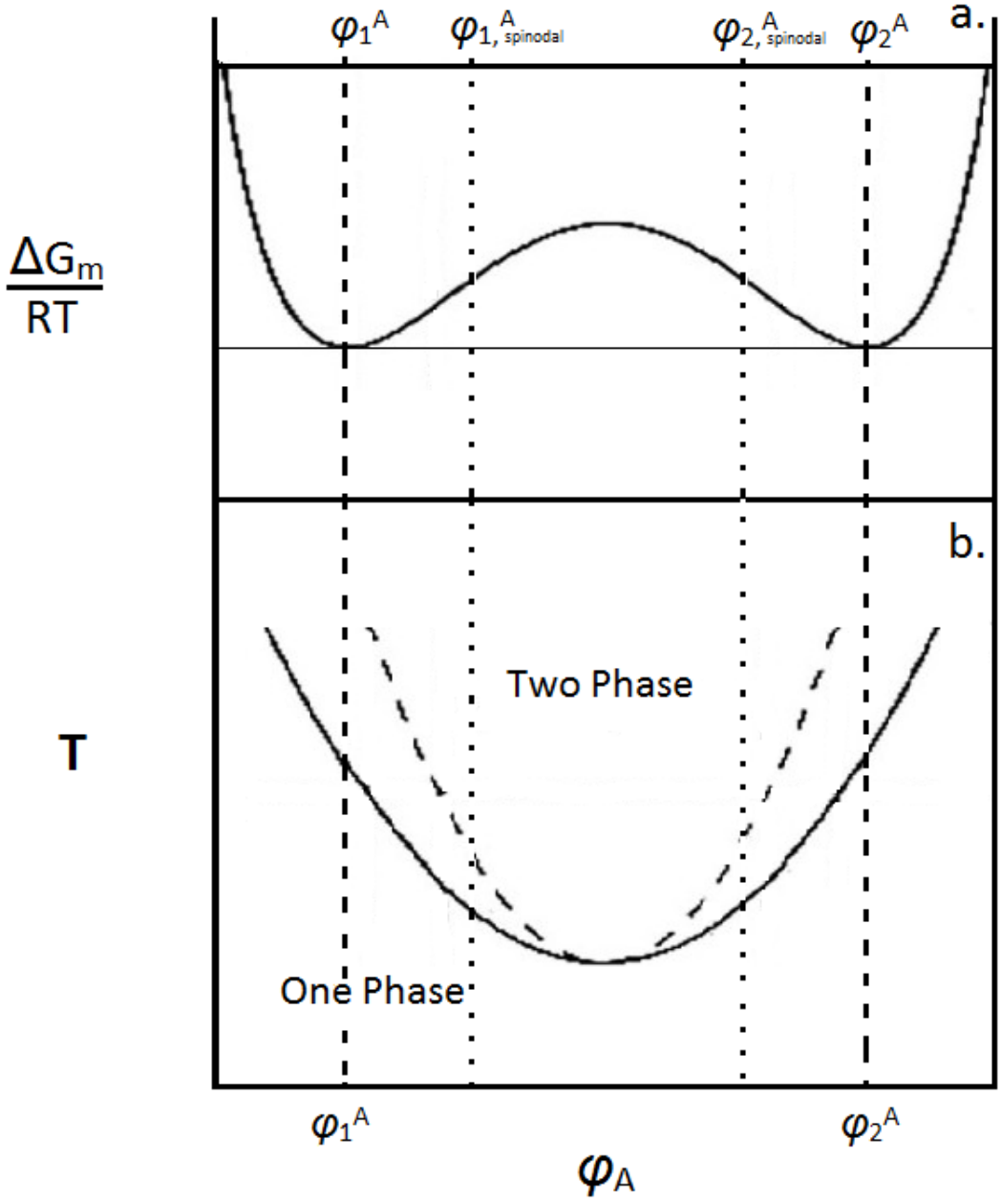

Figure 0.1(a) Generalized free energy of mixing versus volume fraction and (b) phase diagram showing both the spinodal (dashed) and binodal (solid) of a two component system

region, above which the mixture will spontaneously separate into two phases. As will be discussed in more detail later, this phase diagram can be used to determine the relative amounts of each component in each phase in a phase separated system.

1.3 Miscibility of Cellulose Acetate Blends

The discussion above describes the complexity of blending two polymeric components to achieve properties of a one phase, compatible blend. In practice, understanding the variables that determine the phase behavior of polymer blends is a surprisingly complex topic in the field of polymer science. Despite these challenges, polymer blends have seen commercial use as far back as the late 1800's. One of the first polymer blends to realize commercial use was the modification of a natural polymer, nitrocellulose. This modification requires a natural resinous product, shellac, to be blended with nitrocellulose to create a bioadhesive polymer. Similar in structure to nitrocellulose is another natural polymer, cellulose, however the properties of these two polymers, are markedly different. The commercial use of cellulose dates back over a century and, because it is found in all plant matter, cellulose is one of the most abundant biopolymers on earth. The structure of cellulose is illustrated in the bottom of Figure 1.2 and shows a linear chain of anhydro-glucopyranose ring complete with hydroxyl substituents. The derivatized cellulose chain can be partially or fully substituted at the C-2, 3, and 6 positions. Furthermore, the type and amount of substitution has a significant impact on end-use properties, thus the use of cellulose with its derivatives has broad applications including fibers, films, plastics, and coating to name a few.[11]

Cellulose acetate is a cellulose derivative that has seen wide-spread application for over a century. This cellulose derivative substitutes the hydroxyls along the cellulose

backbone with an acetate substituent at the C-2, 3, and/or 6 positions of the anhydroglucopyaranose ring as shown in Figure 1.1. The specific amount of substitution is commonly presented as the average degree of substitution on the ring, where the maximum degree of substitution (DS) is 3. Figure 1.2 shows the various substitutions of the ring, where the bottom is cellulose with zero substitutions (DS = 0), followed by mono-substituted (DS=1), di-substituted (DS=2), and, a tri-substituted cellulose acetate (DS = 3) moving up the figure. Performance of cellulose acetate is greatly affected by the variation of acetate substitution on the backbone of the chain. For instance, cellulose acetates with a DS between 2.0 and 2.5 are commonly used as fibers and membranes.[12] As the DS approaches 3.0, however, the solubility in common organic solvents and gas permeability decrease while the T_m and crystallinity increase. The impact of the change in degree of substitution on its properties is better understood for neat CA than it is for a blend of cellulose acetates having different degrees of substitution.

Much work has been completed to understand the effect of blending cellulose esters with other polymers.[13,14,15,16] For instance, Zhou *et al.* examined blends of CA with polyurethane (PU) using FT-IR. A series of blends were studied ranging from neat PU to neat CA. Relative to blend compositions on the edges, intermediate blend compositions displayed a shift to a lower wavelength of the hydroxyl peak. This shift to a lower wavelength indicates an increase of intermolecular hydrogen bonding between the Cellulose Acetate (CA) and the urethane linkages and, conversely, a decrease in self-associations of O-H groups among cellulose acetate chains. The free volume of the system does not change with the additional intermolecular interactions.[17] Kokot *et al.* combined 2-D correlation analysis of temperature dependent FTIR with Principal

Component Analysis (PCA) to monitor the temperature dependence of hydrogen bonding in cellulose.

Number of Substitutions	Molecular Structure
3	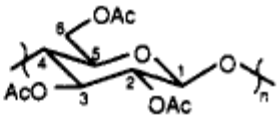 triacetyl
2	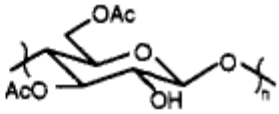 3,6-diacetyl
1	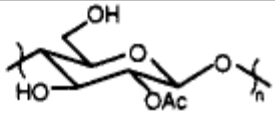 2-monoacetyl
0	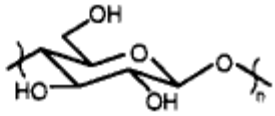 unsubstituted

Figure 0.2 Cellulose Acetate of varying degrees of substitution going from cellulose on the bottom (0 substitutions), to Cellulose triacetate on top (three substitutions)

The study found that interchain hydrogen bonding is generally stronger than intrachain hydrogen bonding, however over a temperature range 40-150°C, the hydrogen bonding is largely unaffected.[18] Rao *et al.* investigated cellulose acetate hydrogen phthalate (CAP) and poly methyl methacrylate (PMMA) by solution viscometry and differential scanning calorimetry and found that CAP forms a miscible blend with PMMA over the entire composition range. They attribute the compatibility to the formation of hydrogen bonds between the carbonyl group of the PMMA and free hydroxyl groups of the CAP.[19]

Whereas these studies focus on creating novel blends of CA with other polymers, studies of blends of cellulose esters with different degrees of substitution have been more limited. Slonimskii has reported that blends of CA with a DS of ~ 3 and of CA with DS of *ca.* 2.5 are incompatible.[20] Buchanan *et al*. have completed a considerable amount of work on understanding the biodegradability of cellulose acetates.[21,22] In one study, CA with DS=2.06 was blended with another CA with DS=2.49. The Tg of the 50/50 blend is significantly broadened, indicating this blend consists of two phases. The optical clarity and useful physical properties further indicate a degree of partial miscibility in the middle composition range and complete miscibility when either component is the minor phase.[23] These results show that the blend of CA (DS=2.06) and CA (DS=2.5) is miscible, while the blend of CA (DS~2.5) and CA (DS~3.0) are immiscible , thus the extent of miscibility between two cellulose acetates with different degrees of substitution is not just governed by the difference in the degree of substitution of the two cellulose acetates. Unraveling the roles of various interactions that promote miscibility in these blends is very difficult because of the structural similarities of the two components. Moreover, small differences in degree substitution can lead to immiscibility of the blend, which may

lead to batch-to-batch inconsistencies during processing. Therefore, understanding the driving force involved in the miscibility behavior of CA blends and the effect of the degree of substitution of the two CA components on this miscibility will lead to better processing and greater commercial utility.

1.4 Dynamics of Miscible Homopolymer/Copolymer Blends

The structure-property relationships discussed thus far have considered the impact of varying the structure of the blend components (and the resulting non-bonding interactions involved) on the miscibility of a blend. These non-bonding interactions can additionally affect many blend properties, including polymer dynamics. In fact, non-bonding interactions are one of the many factors that contribute to the complexity of dynamic processes in polymer blends. This is important because, in a polymer blend, the effect of the presence on one component on the dynamics of the second component is not well understood.

From a fundamental and technological point of view, the dynamics of a polymer blend is a very important topic. Understanding the dynamics of each component in a miscible blend can provide predictability of the impact of blending on the response of the resultant blend to an applied stress and on its rheological properties (and thus processing). Developing a molecular level understanding of the effects of blending on the segmental dynamics of each component in the blend is therefore needed to predict the end-use properties of these tailor-made materials. Therefore, there is a need to fully understand how the dynamics of each component of the blend are modified when blended.

The dynamic behavior of pure polymers is complex in that the relevant length scales vary from atomic distances to the length of the polymer macromolecule. Likewise,

the timescales involved vary from atomistic vibrations and rotations on the sub-picosecond timescale, to "macroscopic" times associated with whole-chain relaxation. The faster relaxations include processes such as methyl group rotations, vibrations and other fast rearrangements on the atomic scale. Studies have shown, however, that blending does not appreciably affect these fast motion processes.[24-27] The most relevant dynamic process to a polymer blend is segmental dynamics, due to the fact that the local dynamics of polymer chains on the segmental length scale governs the "transition" into a glassy state (i.e. the glass transition temperature, Tg).[28] The Tg of a polymer is of primary importance as it impacts macroscopic properties such as hardness, modulus and flow behavior. Thus the Tg and, in turn, the dynamics of a polymer blend, are crucial material characteristics as they define the processing and end-use properties of the polymeric material. This importance has motivated a range of intensive theoretical and experimental investigations to understand the effect of blending on the local dynamics of both blend components.

Efforts to characterize the segmental relaxation of blend components have utilized a variety of miscible blends and techniques. One of the more extensively studied blends is poly(isoprene) (PI)/ poly(vinyl ethylene) (PVE).[29, 30-50] The failure of time-temperature superposition is often observed when blending PI at very low concentrations in a PVE matrix and also when PVE is blended in a PI matrix at low loadings.[45] Even at these extreme compositions, the temperature dependences of the dynamics of each component in the PI/PVE blend exhibit unexpected behavior. Miscible blends of poly(vinyl methyl ether)/polystyrene (PS) have also been widely investigated.[51-58] Quasi-elastic neutron scattering and nuclear magnetic resonance studies indicate that each polymer blend

component in the poly(vinyl methyl ether)/PS blend exhibit distinct segmental relaxations (i.e. different glass transition temperatures).[27] More recently, poly(ethylene oxide)/poly(methyl methacrylate) (PMMA) blends have garnered much attention[59-62], where this miscible blend has also been shown to exhibit two distinct glass transition temperatures.[63] A wide range of other miscible systems have also been studied including (PI)/PS,[46,58] poly(ethylene oxide)/poly(vinyl acetate),[64-66] PS/poly(butadiene),[58] poly(isobutylene)/head-to-head poly(propylene) (hhPP)[67,68], and poly(ethylene propylene)/hhPP.[24,69]. These studies indicate that polymer blends that can be characterized as homogenously mixed blends on the molecular level often exhibit a 'dynamic heterogeneity' corresponding to two distinct relaxation times associated with each component of the blend. This heterogeneity persists even for tracer blends where one component is present in very small quantities. For example, PI/PVE exhibits dynamic heterogeneity as the tracer PI component exhibits faster dynamics than the (slower) PVE matrix with which it is blended. This dynamic heterogeneity indicates that the local environment of a polymer segment is different than the average bulk composition.[45]

Recently, the importance of the local environment of a polymer segment on this dynamic heterogeneity has been studied. Perhaps one of the more successful models that has been presented to explain dynamic heterogeneity comes from Lodge and McLeish, which has also inspired a significant effort by many experimental and theoretical groups to test and expand this model.[46,58,65,70-86] This model successfully captures some important dynamic aspects of miscible polymer blends and only requires knowledge of the structure of the individual blend components and the composition of the blend.[41,44,45,54,87]

The Lodge-McLeish (L-M) model utilizes the Kuhn length as the characteristic dimension which, when cubed, gives a "dynamic volume" that defines the length scale of the segmental relaxation process. This volume corresponds to the effective space within which a polymer segment is able to move. Within this small, local volume of a segment, the model incorporates the fact that the composition of the blend will be biased due to chain connectivity, creating a local "self-concentration" that is different than bulk composition. More importantly the Lodge-McLeish (L-M) model asserts that this local "self-concentration" controls the segmental dynamics of each component in a miscible polymer blend. Many experimental results support the self-concentration concept, though it should be noted that interchain interactions are neglected in this model.

This detail is important because recent studies of miscible blends that contain a homopolymer and copolymer indicate that thermodynamic interactions between the two components in the blend can affect the local concentration, and therefore segmental dynamics, of a polymer chain in a miscible blend. Studies in this lab and others have sought to understand the effect of copolymer composition on copolymer dynamics in miscible homopolymer/copolymer blends.[81,88-90] Monte Carlo simulations demonstrate that random copolymers distribute more uniformly in a homopolymer matrix than other copolymer sequence distributions (alternating, diblock, etc.). The work indicates that 50/50 copolymers with ordered sequences such as diblock and alternating copolymers form aggregates in the homopolymer matrix in order to minimize unlike contacts which, in turn, slows the dynamics of the copolymer relative to those of a random copolymer.[90] Additional Monte Carlo simulations studied the effect of copolymer composition on the structure and dynamics of a miscible blend that consists of a random copolymer in a

homopolymer matrix. The study indicates that the copolymer composition impacts the structure as well as dynamics of the copolymers within the homopolymer matrix, which is attributed to the presence and impact of thermodynamic interactions between the homopolymer and copolymer chains. In this study,[88] a copolymer chain rich in monomer "A" that is dispersed in a matrix of homopolymer "A" has a more open structure than a copolymer with a majority "B" monomer, leading to faster dynamics. Copolymer chains having a lower "A" content (i.e. higher "B" content) forms more compact structures, which move more slowly than copolymers with more open structures. An important thermodynamic driving force in this system is the minimization of unlike contacts, where the copolymers with higher B content more readily form favorable B-B intrachain and interchain interactions, slowing the copolymer chain motion.

The effective monomeric friction factor, ζ_{eff}, is an important parameter to characterize the dynamics of polymer chains. ζ_{eff} describes the friction of a polymer segment as it diffuses through a polymer matrix, where the average chain length between contour changes defines a polymer segment. For homopolymers, which have identical repeat units, the segment length is constant; however, copolymers do not have identical repeat units and thus the segment length changes with copolymer composition. Thus, the monomeric friction factor will change with copolymer composition.

This is exemplified in previous studies that monitored the viscosity of disordered linear diblock copolymers of styrene (Sty) and methyl methacrylate (MMA) with varying composition.[89] This system exploits the large difference in friction factors of the two components, where styrene has a lower friction factor, which may be due to being less substituted and less polar than MMA. This study shows that the friction factor of the

copolymer varies with copolymer composition, where ζ_{eff} increases with increasing MMA content. ζ_{eff} of the disordered diblock copolymer is the log weighted average of ζ_{PMMA} and ζ_{PS} where the composition of the copolymer ranges from 9 % to 91 % Sty.[89]

While the temperature and composition dependence of the dynamics of pure copolymers have been well studied, the dynamic behavior of a copolymer that is homogeneously dispersed in a homopolymer matrix is much less studied experimentally. The importance of thermodynamic interactions in a copolymer/homopolymer blend to its structure and dynamics has been studied using neutron reflectivity (NR).[88] In this study, the repulsive interaction between styrene and MMA is utilized to tune the thermodynamic interaction between the two components. This study also found that increasing the MMA content in the copolymer results in slower dynamics (i.e. an increase in the monomeric friction factor). However, the random copolymers exhibit faster dynamics than block copolymers with identical composition and molecular weight. This clearly shows that the copolymer composition is not the only factor that determines the dynamics of the copolymer in this miscible system. Further analysis shows that the local environment is richer in styrene than what is predicted by the L-M model. One explanation for this discrepancy is that the thermodynamic interaction between styrene and MMA leads to alteration in copolymer conformation, leading to a friction factor that more resembles the faster dynamics of the styrene segments.

The previous simulation and NR studies each indicate that the thermodynamic interaction between the styrene and MMA impact the structure and dynamics of the copolymer in the homopolymer matrix. There is therefore a need to more thoroughly understand the role of thermodynamic interactions on the dynamics of miscible polymer

blends, to enable rational estimations of their dynamics. This understanding is especially important in light of the fact that successful theories such as the L-M model do not account for such intermolecular interactions. The benefit of comparing the experimental results to the L-M theory, then, is twofold: the model's ability to accurately predict blend dynamics will be tested while also providing insight into the fundamental aspects that govern dynamics of the blends employed in this study. Overall, the structure-property relationships of the blends investigated here will provide a better understanding of the impact that thermodynamic interactions have on the dynamics of multi-component blends.

1.4 Effect of Architecture on Block Copolymer Morphology

Structure-property relationships are discussed above considering a blend of two separate components. This section further explores structure-property relationships of multicomponent polymers, but shifting to a system where the two polymer chains are covalently bonded, block copolymers. As opposed to blending, covalently bonding two components together to create a block copolymer leads to an important phenomenon in polymer chemistry: ordered microphase separation. Considerable research efforts have been made in the scientific community to better understand block copolymer morphology and have led to a better understanding of microphase separation. The formation of these morphologies, typically spheres, cylinders, bi-continuous gyroid, and lamellae for two component block copolymers,[91] is affected by a number of molecular characteristics such as molecular weight, molecular architecture, molecular structure, segregation strength, composition, as well as sample preparation. In general, morphological control of linear

diblock copolymers is now well understood[92,93] and has led to useful applications of block copolymers as thermoplastic elastomers (TPEs)[5,6] and polymer blend compatibilizers.[1-4]

In contrast to the case for linear diblock copolymers, structure-morphology relationships for nonlinear block copolymers are much less explored, largely due, until recently, to a lack of synthetic methods for their tailored synthesis. In the 1970s, Bi and Fetters[94] synthesized and studied the morphologies and properties of star-block copolymers of polystyrene (PS) and polyisoprene (PI). Star-block copolymers are star polymers where each arm is itself a block copolymer, and these materials exhibited superior tensile strength relative to linear triblock copolymers having similar composition and molecular weights. Also in the 1970s, the synthesis of fairly well-defined multi-graft copolymers having diene backbones and PS side chains was reported.[95-101] However, studies of the bulk morphology of these TPE materials were not described.

Beginning in the early 1990s, systematic studies aimed at elucidating the effect of branched architecture on the morphology and properties of block copolymers were initiated.[101] This work was made possible by the development of synthetic routes to well-defined miktoarm star architectures (chemically different arms linked together to form a star),[102-105] as well as to a variety of more complex branched block copolymer architectures.[106-110] Morphology studies on miktoarm stars indicate that macromolecular architecture can be used to tune morphology independent of the volume fraction of the two components.[111,112]

The morphological behavior of a miktoarm star in the strong segregation limit (SSL) has also been described in a theoretical study by Milner.[113] The Milner theory accounts for the fact that the A and B blocks may differ in conformation, which will

result in a variation in the arms stretching at the junction point. This computational result predicts morphologies of the miktoarm that are based on the volume fraction of component B, φ_B (= 1- φ_A), and a molecular asymmetry parameter, ε. Incorporating both architectural and conformational asymmetries, ε is calculated as $\varepsilon = (n_A/n_B)(l_A/l_B)^{1/2}$ where n_A and n_B are the numbers of A and B arms, which are linked at a junction point, and l_A and l_B reflect differences in conformational flexibility of the two polymeric species.

In the strong segregation limit (SSL), the interphase region between domains is about 2-5 nm.[114-116] Compared to the domain sizes, which are typically tens of nanometers, this interphase region can be considered two-dimensional and has curvature properties that can be approximately correlated to the volume-filling characteristics of the opposing blocks of the copolymer. As one moves from a convex to a concave curvature, the volume available to a polymer chain decreases. For a diblock copolymer, the magnitude of the interfacial curvature is proportional to the relative volumes available to the two blocks. Thus, the most asymmetric diblock copolymers will form morphologies having the highest curvature, spheres. As the volume fraction of the two blocks becomes more similar, the interfacial curvature decreases, and symmetrical diblock copolymers form a lamellar morphology with a flat interface. Similarly, there is a shift in interfacial curvature if there is architectural asymmetry at a junction point. For example, an A_2B miktoarm star copolymer exhibits architectural asymmetry creating more lateral crowding and stretching on the side with the two A arms. Such architectural asymmetry has been found to promote the formation of morphologies that place the two A chains on the convex side of the interface, while inhibiting the formation of morphologies that place the two A chains on the concave side of the interface. The theoretically predicted shift of

the morphological behavior with architectural asymmetry is in agreement with experimentally observed morphologies of several PS_2-*star*-PI block copolymers where the connectivity is held constant, varying only the arm length and composition of the copolymer.[112] The agreement between theory and experiment is encouraging but more studies are needed in order to fully understand the impact of macromolecular architecture on the morphology of nonlinear block copolymers.

In the present work, a series of PS-PI block copolymers were synthesized, holding copolymer composition constant (~70 vol % PS) while varying copolymer architecture from a linear diblock copolymer to PS_2PI, $PSPI_2$, and PS_2PI_2 miktoarm stars. The morphologies of these block copolymers were characterized using transmission electron microscopy (TEM) and small-angle x-ray scattering (SAXS). The experimentally observed morphologies are also compared with those expected based on Milner theory and simulations in order to achieve a greater understanding of the effect of macromolecular architecture on block copolymer morphology.

Overall, the research presented in this dissertation focuses on attaining a better understanding the variables that impact the dynamics and phase behavior of multi-component polymer systems Chapters 2 and 3 explore structure-property relationships of blending two chemically different components in terms of miscibility and dynamics, providing greater understanding of the impact of non-bonding interactions in polymer blends. Chapter 4 investigates the morphology of a series of styrene-isoprene copolymers by varying the bonding scheme of each copolymer, providing insight into how this recently experimentally controllable parameter affects morphology. These studies provide a more complete understanding of the variables that affect polymer blends and

block copolymers, contributing to a better understanding of how copolymer architecture and thermodynamic interactions affect miscibility, dynamics and phase separation of multi-component polymer systems.

CHAPTER 2:EFFECT OF POLYMER STRUCTURE ON THE MISCIBILITY OF CELLULOSE ACETATE BLENDS: A SMALL-ANGLE NEUTRON SCATTERING STUDY

2.1 Introduction

This chapter presents the results and interpretation of a set of experiments designed to provide insight into the fundamental interactions that control the miscibility of blends that contain cellulose acetates with different degrees of substitution. From a processing and applications standpoint, there are several advantages to converting cellulose to its organic esters (such as cellulose acetate) such as improved end-use properties.

One important aspect of cellulose acetate derivatives that are incompletely substituted is that the cellulose acetate chain is effectively a copolymer. Due to the variation in the number of substituents on the monomer and their respective positions on the anhydroglucopyaranose ring (Figure 1.2), the cellulose acetate copolymer may be composed of as many as 8 different monomers within the copolymer chain. This leads to a polymer backbone with a distribution of monomers along the chain, where the composition and distribution of the substituents often determines the physical properties of the cellulose acetate. Surprisingly, even subtle differences in the degree of substitution of two copolymers can lead to phase separation. A reasonable understanding of this phenomenon is lacking, and is needed to provide guidance to direct the synthesis and fabrication of cellulose acetates with targeted properties.

Though much work has been completed to understand the effect of blending cellulose and cellulose acetates with other polymers, few studies have focused on blends where both components are cellulose acetates that vary only in the number of acetate substituents on the two components. This is primarily because it is difficult to differentiate one cellulose acetate from another experimentally. In this experiment, the

unique ability of neutron scattering to introduce contrast between similar (or identical) polymers by selective deuteration is exploited. Therefore, small angled neutron scattering (SANS) is used to characterize the structure and miscibility of a series of blends where the average degree of substitution of the components of each blend is varied. (as shown in Figure 1.2). In this manner, the systematic variation of the difference in the degree of substitution of the two components provides a pathway to determine the impact of this variable on the miscibility of the blend. Further, the determination of the Flory interaction parameter, χ of each blend quantifies the overall favorability of non-bonding interactions present in the system, providing fundamental insight into the correlation between cellulose acetate structures, difference in degree of substitution between components, intermolecular interactions that exist between blend components and the miscibility of the resultant blend.

2.2 Experimental

2.2.1 Cellulose Acetate Synthesis

Cellulose acetate with various degrees of substitution were prepared by the hydrolysis of cellulose triacetate[117] according to a previously described procedure.[118,119] In general, 1.5 gram of cellulose triacetate is added to a 100 mL round bottom flask containing 30 mL glacial acetic acid, and the mixture is stirred at 50°C to achieve complete dissolution. Catalyst (36.0 mg of concentrated sulfuric acid in 4mL of distilled water) is added drop-wise to the flask at 80°C and the hydrolysis process is completed for various time periods. When the reaction is complete, the solution is added dropwise to a 1000 mL beaker containing 400 mL distilled water, and the white, fibrous precipitate is collected

by filtration. The filtrate is then washed twice with 100 mL distilled water, once with 100 mL 1:1 distilled water/methanol, and finally with 50 mL of methanol. The cellulose acetates are then placed in a warm vacuum oven (around 60°C) to remove any residual water. Determination of the degree of substitution of the cellulose acetates was completed with ^{1}H NMR using a Varian 400MHz NMR. NMR samples were prepared by dissolving approximately 15 mg of cellulose acetate in 1 mL of DMSO-d6. The degree of substitution of each CA is calculated according to a previously described procedure[118] and are listed in Table 2.1 where each CA sample is denoted by the number of hours of the hydrolysis reaction. The DS of the resultant cellulose acetates is also plotted as a function of hydrolysis time in Figure 2.1, showing the expected linear dependence. The blends that are studied are also listed in Table 2.1 where the d-24hr CA (DS=2.19) is one component in every blend. The resulting difference in the degree substitution (ΔDS) of the deuterated CA and the protonated cellulose acetate are listed as well, where ΔDS varies from .06 to .63.

2.2.2 Small-angle neutron scattering (SANS)

This experiment utilizes neutron scattering and selective deuteration, a very powerful and versatile technique to determine the structure of polymeric materials in the melt of concentrated solution. As such, this section introduces some basic concepts of neutron scattering.

Neutrons exhibit particle-wave duality similar to photons (in light scattering) and X-rays (in X-ray scattering). Unlike X-ray and light scattering, which interact with the electrons of a scattering particle, neutrons interact with nuclei via the strong nuclear force and/or with magnetic moments via dipole-dipole coupling.[120]

Table 2.1. Cellulose triacetate hydrolyzed for the amount of hours indicated in the left column. The degree of substitution (middle column) refers to the average number of acetate groups per anhydroglucopyaranos ring, difference in degree substitution (right column) between the deuterated 24hr homopolymer and the protonated homopolymer with which it is blended.

Sample Name (by hours reacted)	Degree Substitution (DS)	Difference in Degree Substitution (ΔDS)
d-24hr	2.19	0
21hr	2.25	0.06
33hr	2.04	0.15
15hr	2.51	0.32
12hr	2.61	0.42
42hr	1.56	0.63

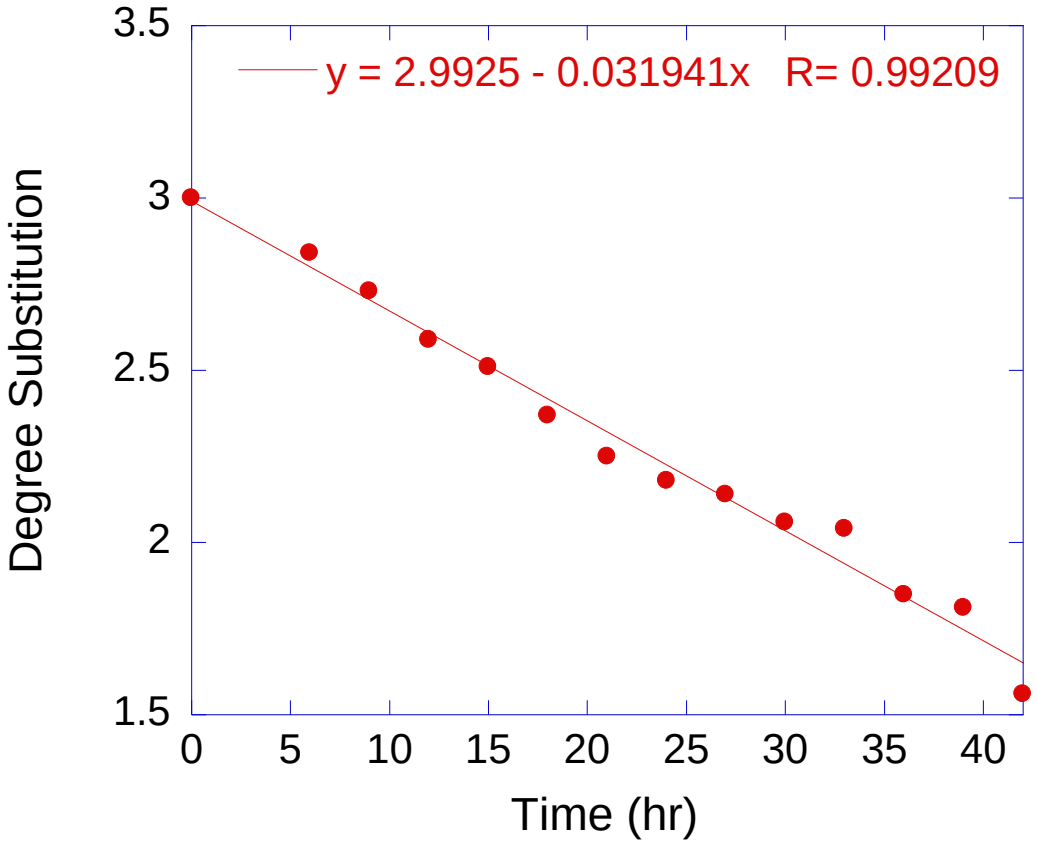

Figure 2.1 Degree substitution of cellulose acetate as a function of hydrolysis reaction time.

A schematic representation of elastic scattering or a scattering event where the radiation does not change wavelength is represented in Figure 2.2. When neutrons in the incident beam impinge on the sample, some of the neutrons pass through the sample and some of them are scattered. The scattered neutrons are of particular interest as they carry structural information of the specimen. In the elastic interaction, the momentum transfer between scattering particle and neutron is given by $\vec{q} = \vec{k} - \vec{k}_0$, where $\vec{k}$ and $\vec{k}_0$ are the momentum (magnitude $2\pi/\lambda$) of the scattered beam and the incident beam, respectively. The magnitude of the momentum transfer between incident and scattered waves (as presented in Figure 2.2) is given by,

$$|\vec{q}| = \frac{4\pi}{\lambda}\sin\theta \qquad (2.1)$$

where λ is the wavelength of the neutron and 2θ is the angle of the scattered beam. Equation 2.1 illustrates that $\vec{q}$ is controlled by two parameters: wavelength and scattering angle. This experiment utilizes a scattering angle that is small (0.1-10°), which correlates to probing larger structures. The interaction between the neutron-nuclei interaction depends on two parameters: the neutron scattering length, b, and the scattering cross section, σ.[121]

The amplitude (A) of scattered neutrons from a single particle is given by

$$A(x,t)=A_0 \cos(\omega t - 2\pi x/\lambda) \quad (2.2)$$

where ω is the angular frequency of the incident wave and t is time. The amplitude of the wave that is scattered at a nucleus that is a a distance *r* from another identical nucleus is

$$A(x,t) = b\cos(\omega t - q\cdot r) \qquad (2.3)$$

$$= b\exp(i(\omega t - q\cdot r)) \qquad (2.4)$$

$$= b\exp(i\omega t)\exp(-iq\cdot r) \qquad (2.5)$$

where b is the scattering length of the both nuclei, $i = \sqrt{-1}$ and *r* is the vector between the two nuclei. The amplitude of the scattered waves from multiple nuclei pairs with identical scattering length, b, is

$$A(q) = b\sum_{i=1}^{N}\exp(-iq\cdot r_i) \qquad (2.6)$$

where r_i is the distance between the two scattering particles of a given pair. The probability that neutrons impinging on the sample are scattered into a unit solid angle in a given direction is known as the differential scattering cross section, $\left(\frac{\partial\sigma}{\partial\Omega}\right)$, where σ is the scattering cross section and Ω is the solid angle. $\left(\frac{\partial\sigma}{\partial\Omega}\right)$ manifests experimentally as the intensity of the scattered radiation (I(*q*)), and is related to the square of the amplitude, A(q), as shown in Equation 2.7. In this equation, A*(q) is the complex conjugate of A(q) and <…> denotes an ensemble average.

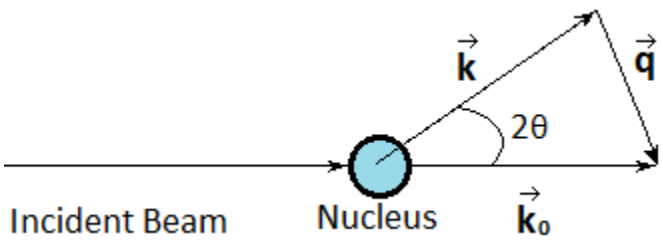

Figure 2.2 Relationship between wave vectors and momentum transfer for elastic scattering.

$$\frac{d\sigma}{d\Omega} = I(q) = A(q)A^*(q) = \sum_{ij} < b_i b_j \exp\left(-iq\left(r_i - r_j\right)\right) > \qquad (2.7)$$

where q is the momentum transfer and r_i is the distance of particle i from an arbitrary origin (x=y=z=0). The scattering length density (ρ) of a scattering particle is determined as the scattering length, b, per given molar volume, ν, of all atoms within the scattering particle.

The experimentally measured scattered intensity is proportional to the difference in scattering length densities (Δρ) between scattering domains as shown in equation 2.8.

$$I(q) = \frac{d\sigma}{d\Omega} = N\nu^2(\Delta\rho)P(q) \qquad (2.8)$$

Equation 2.8 dictates that scattering intensity is also determined by the number of scattering particles, N and the form factor, P(q) of the scattering object. The form factor of the scattering object is a result of intramolecular interferences and is characteristic of the size and shape of the scattering object.[120] P(q) is the Fourier transform of the density distribution of the scattering particles in the scattering object.

Neutron scattering of polymeric materials takes advantage of the large scattering length difference between hydrogen (-3.7406 fm) and deuterium (6.671 fm), which provides the contrast required in a neutron scattering experiment. The SANS experiments were completed at the High Flux Isotope Reactor (HFIR) using the CG3 Bio-SANS instrument at Oak Ridge National Laboratory.[122] Each blend and sample was prepared by dissolving ~.25g of deuterated and protonated cellulose acetate in a 50/50 mixture of

MeOH/$MeCl_2$. The blend was then drop cast into a mold of comparative size to the neutron sample holder. Each blend was dried at ambient temperatures and pressure for ~3 hours, then dried under high vacuum for ~6 hours and further dried for another 6 hours under high vacuum at 100 °C. This preparation procedure forms a disk of ~1mm thickness that is then placed between detachable quartz windows. Two different instrument configurations were employed to collect scattering data over the range of scattering vectors $0.006 < q < 0.06 Å^{-1}$, where q is the momentum transfer vector defined in Equation 1 and 2θ is the scattering angle. These configurations include sample-to-detector distances of .3 and 6m, both with a neutron wavelength (λ) of 6 Å. In each case the center of the area detector was offset by 150 mm. The results presented in the main body of this paper utilize data collected at 100 °C. (Appendix contains SANS results at other temperatures). The instrument resolution is defined by the relative wavelength spread, $\Delta\lambda/\lambda = 0.14$. The scattering intensity I(q) as a function of q is obtained by azimuthally averaging the two-dimensional scattering images, which were normalized to incident-beam monitor counts and corrected for detector dark current and pixel sensitivity and background scattering from the quartz cell. Normalizing the data to thickness and scaling the scattered intensity to that of a Porasil B standard provides the scattered intensity in absolute units.

2.3 Results

Small angle neutron scattering experiments were carried out on a series of cellulose acetate (CA) blends. The scattering curves of the blends at 100°C are displayed in Figure 2.3, plotted as the absolute scattering intensity as a function of q. Excluding the

blend that contains the 42 hr protonated CA, the scattering at low q of each blend decreases with a decrease in ΔDS. The lower scattering intensity at low q is associated with a higher degree of miscibility.

Neutron scattering data of miscible polymer blends are customarily fit to the Ornstein-Zernike scattering function. Fitting the scattering curves in Figure 2.3 with the Ornstein-Zernike equation, however, yields poor fits and negative q=0 intercepts indicating the components are not miscible, and that the blends contain two phases. Two-phase systems are analyzed using the Debye-Bueche[121] equation, which is completed in Figure 2.3, allowing a quantitative analysis of the two-phase blend.

The compositions of the two phases in each blend, however, are not immediately known, but provide additional information on the miscibility of the two components. The blends may be fully immiscible, where the two phases are pure component A or component B, or partially miscible. In a partially miscible system, there exist two phases where one is rich in component A (say, the deuterated component) and the other is rich in component B (the protonated component), however the phase rich in component A has a small amount of component B and the phase rich in component B has a small amount of

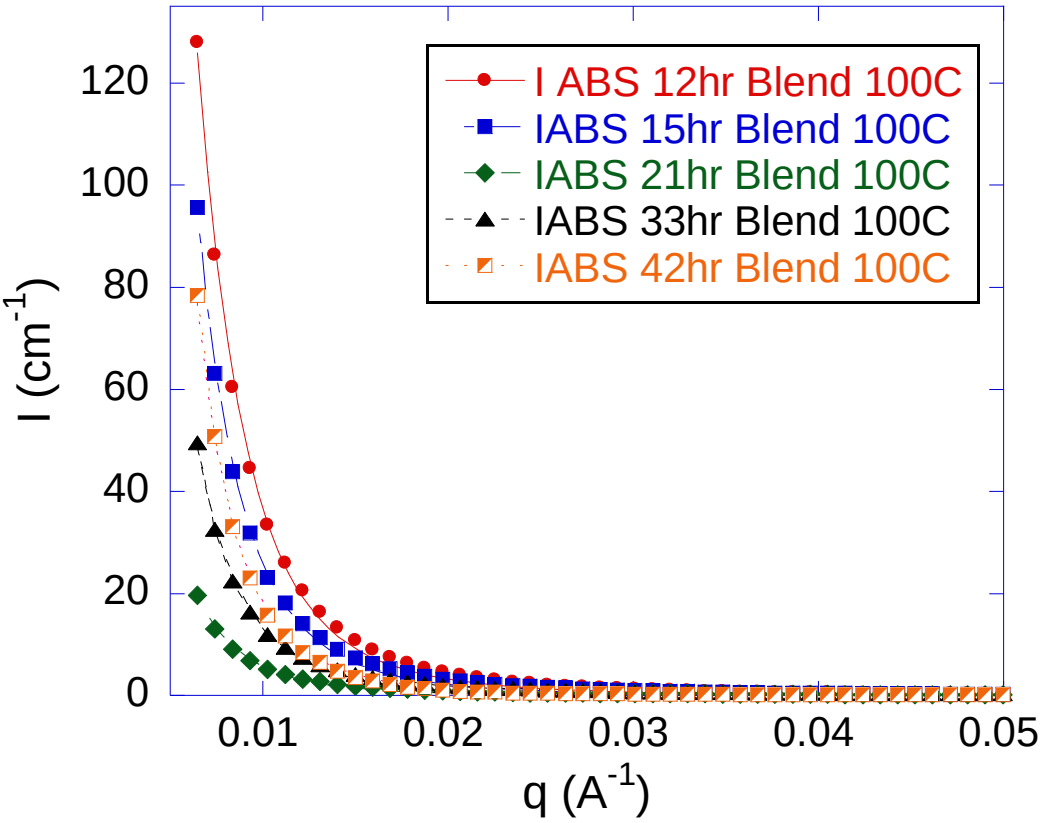

Figure 2.3. 100°C SANS data of Cellulose Acetate Blends fit to Equation 2.12

component A in it. A cartoon demonstrates this in Figure 2.4. Figure 2.4a represents a fully immiscible system where phase 1 is pure component A represented by white and phase 2 is component B represented by black. Figure 2.4b is a partially miscible system where there still exist 2 phases (phase 1 and 2) however now there is a small volume fraction of A that exists in phase 2 (φ_2^A) which is primarily component B, and a small volume fraction of component B in phase 1 (φ_1^B) which is primarily component A. This is represented in the cartoon as a mostly black phase 2 in Figure 2.4b, however the small fraction of white in the phase leads to a dark grey, and the small volume fraction of black in the white phase 1 leading to a light grey.

As mentioned in the previous section, Equation 2.8 demonstrates that the measured scattering intensity is proportional to the difference in scattering length density of the two scattering domains, which are the two phases in this system. For a two-phase system, the largest difference in scattering length density, $\Delta\rho$, or maximum contrast is achieved when the two components are fully immiscible with each other. Going to the other extreme, if the two components are weakly immiscible, there is significantly less contrast due to the fact that the compositions of the two phases are very similar. Thus the weakly immiscible system corresponds to a lower difference in scattering length density ($\Delta\rho$ in Equation 2.8). The difference in scattering length density of the two phases in a partially miscible system is therefore less than that of a fully immiscible, two-phase system. Moreover, the neutron scattering results presented in Figure 2.3 will be analyzed to assess $\Delta\rho$ of the blends studied to determine the composition of the two phases present, and provide evidence of the extent of immiscibility of the two cellulose acetates in each blend.

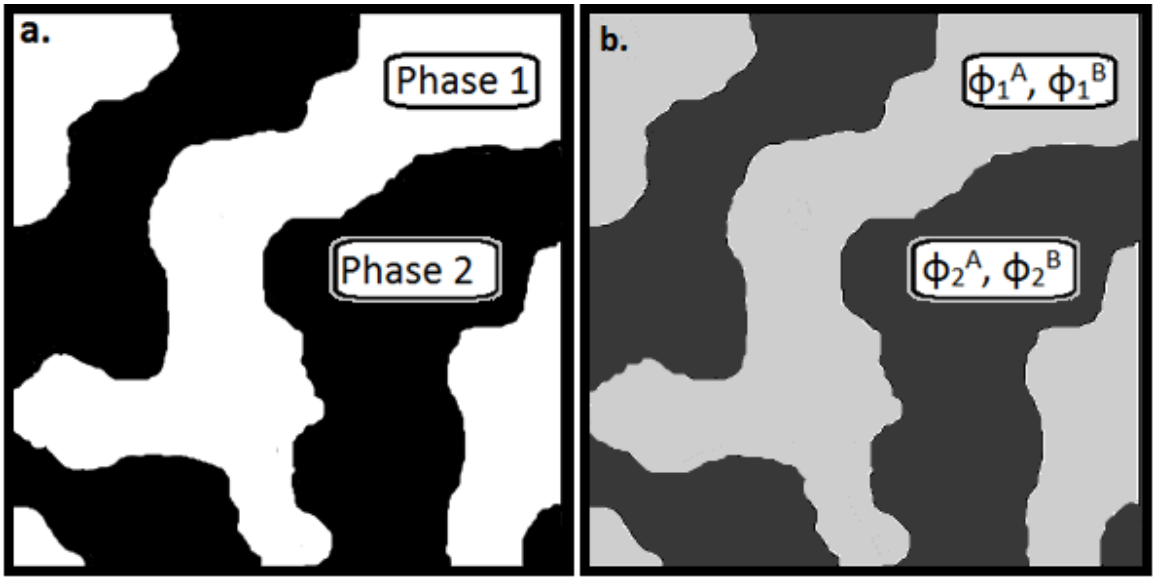

Figure 2.4. Two components, A (White) and B (Black) in a blend that are a) a two phase immisible system of phase 1 and 2 and b) a two phase partially miscible system of phase 1 (light grey) and 2 (dark grey) where a volume fraction of each component exist in each phase

In this analysis, a theoretical difference in scattering length density $\Delta\rho_{Theoretical}$ of a fully immiscible two phase system is calculated and compared to the experimentally determined difference in scattering length density ($\Delta\rho_{exp}$) of each blend. This comparison of $\Delta\rho_{Theoretical}$ to the $\Delta\rho_{exp}$ assesses the miscibility of each blend, where a decrease in $\Delta\rho_{exp}$ relative to a $\Delta\rho_{Theoretical}$ is a sign of increased miscibility.

$\Delta\rho_{Theoretical}$ and $\Delta\rho_{exp}$ are therefore determined by the following methods: in a theoretical, fully immiscible, two-phase system, the scattering length density contrast is defined as

$$\Delta\rho_{Theoretical} = \rho_2 - \rho_1 \qquad (2.9)$$

where ρ_1 and ρ_2 are the scattering length densities of phase 1 and phase 2, respectively. The calculation of $\Delta\rho_{Theoretical}$ requires calculation of ρ for each blend component, which is based solely on the components specific structure and molar volumes. ρ of a given molecule is given by

$$\rho = \frac{\sum_{i=1}^{n} b_{c_i}}{V_m} \qquad (2.10)$$

where b_{ci} is the scattering length of each atom in the repeat unit and V_m is its molar volume. Calculation of ρ via Equation 2.10 often only requires a single repeat unit to be considered. However, the average substitution of the CA components in each blend is not a whole number, which means multiple repeat units need to be considered to accurately reflect ρ of each cellulose acetate studied. For instance, considering 100 repeat units

where 51 units of the CA have a DS of 3 (top structure in Figure 1.2) and 49 units have a DS of 2 (second-to-top structure in Figure 1.2) gives an average DS of 2.51 which reflects the actual DS of the 15 hr sample, as seen in Table 2.1. The scattering length density of the 15hr cellulose acetate is thus given as 0.51 x $b_{DS=3}$ + 0.49 x $b_{DS=2}$, where the molar volume (=mass [m]/density [d]) is given as (0.51 x $m_{DS=3}$ + 0.49 x $m_{DS=2}$)/(0.51 x $d_{DS=3}$ + 0.49 x $d_{DS=2}$). The densities of cellulose and cellulose triacetate are taken as 1.5g/cm^3 and 1.27g/cm^3, as reported in the literature.[123,124] The calculation of ρ for each protonated sample and ρ of the 24 hr deuterated sample (see appendix for details of the deuterated ρ calculation) are used to determine $\Delta\rho_{Theoretical}$ for each blend studied and are listed in Table 2.1.

The $\Delta\rho_{exp}$ of each blend is obtained by analyzing the experimental data, by fitting each scattering curve to the Debye-Bueche equation, which is shown in Equation 2.11.[121]

$$I(q) = \frac{I(0)}{\left(1 + l_p^2 q^2\right)^2} \qquad (2.11)$$

These fits are presented in Figure 2.3 where each fit has a corresponding R value $\geq$ 0.99. In Equation 2.11, I(0) is the extrapolated scattering intensity of each blend at q=0, l_p is the average chord length, and *q* is the wave vector. The chord length is the average length through each individual phase, and is a measure of average domain size. $\Delta\rho_{exp}$ is determined from the invariant, $< \eta^2 >$, which quantifies the total scattering power of a sample. The invariant is useful in the experimental evaluation of $\Delta\rho_{exp}$[121] as it relates the two quantities, I(0) and l_p, as

$$I(0) = 8\,\pi\, l_p^3 < \eta^2 > \qquad (2.12)$$

Values of l_p and $<\eta^2>$ determined from the fitting of the SANS data are given in Table 2.2. The average chord length and the invariant generally increase with increasing ΔDS, where the increasing $<\eta^2>$ intensity indicates decreasing miscibility. The scattering length density contrast, $\Delta\rho_{exp}$, is related to the invariant by

$$\langle \eta^2 \rangle = (\Delta\rho_{exp})^2 \varphi_1 \varphi_2 \qquad (2.13)$$

Where $\Delta\rho_{exp}$ is the difference in scattering length density of the two phases and φ_1 and φ_2 are the volume fractions of the two phases. Analysis of the invariant in Table 2.2 provides a method to determine $\Delta\rho_{exp}$, which can then be compared to the theoretical scattering length density difference of a fully immiscible system ($\Delta\rho_{Theoretical}$). $\Delta\rho_{exp}$ for each blend is presented in Table 2.2. The difference between $\Delta\rho_{exp}$ and $\Delta\rho_{Theoretical}$ gives a qualitative measure of the blend miscibility, where an non-zero value of $\Delta\rho_{Theoretical}$ - $\Delta\rho_{exp}$ provides evidence that a blend is partially miscible.

$\Delta\rho_{Theoretical} - \Delta\rho_{exp}$ as a function of the difference in degree substitution of the two components (ΔDS) in the blend is presented in Figure 2.4. If this difference were zero, the blend would have no miscibility resulting in a fully immiscible two-phase system. For each blend in the study, however, there is a decrease of approximately an order of magnitude in the experimentally determined $\Delta\rho_{exp}$ relative to $\Delta\rho_{Theoretical}$. The 21hr, 33hr, 15hr, and 12hr blends decrease linearly with $\Delta\rho_{Theoretical} - \Delta\rho_{exp}$ upon increasing ΔDS. The magnitude of $\Delta\rho_{Theoretical} - \Delta\rho_{exp}$ for the 42hr blend is less than the 12hr and 15hr blend, however, indicating greater miscibility than these blends, despite having a greater ΔDS. The decrease observed in Figure 2.4 is significant in that it demonstrates that there

Table 2.2. l_p values obtained from fitting the cellulose acetate scattering curves using Eq. 2.11. $\langle\eta^2\rangle$ values are obtained using Eq. 2.12. $\Delta\rho_{exp}$ is calculated using Eq. 2.13.

Blend (Hours reacted)	ΔDS	l_p (Å)	$\langle\eta^2\rangle$ (Å^{-2})	$\Delta\rho_{exp}$	$\Delta\rho_{Theoretical}$
21hr	.06	189.06	7.045E-15	1.679E-07	2.383E-06
33hr	.15	210.4	1.699E-14	2.607E-07	2.377E-06
15hr	.32	214.19	3.274E-14	3.619E-07	2.393E-06
12hr	.42	196.52	4.548E-14	4.265E-07	2.397E-06
42hr	.63	268.6	2.568E-14	3.205E-07	2.367E-06

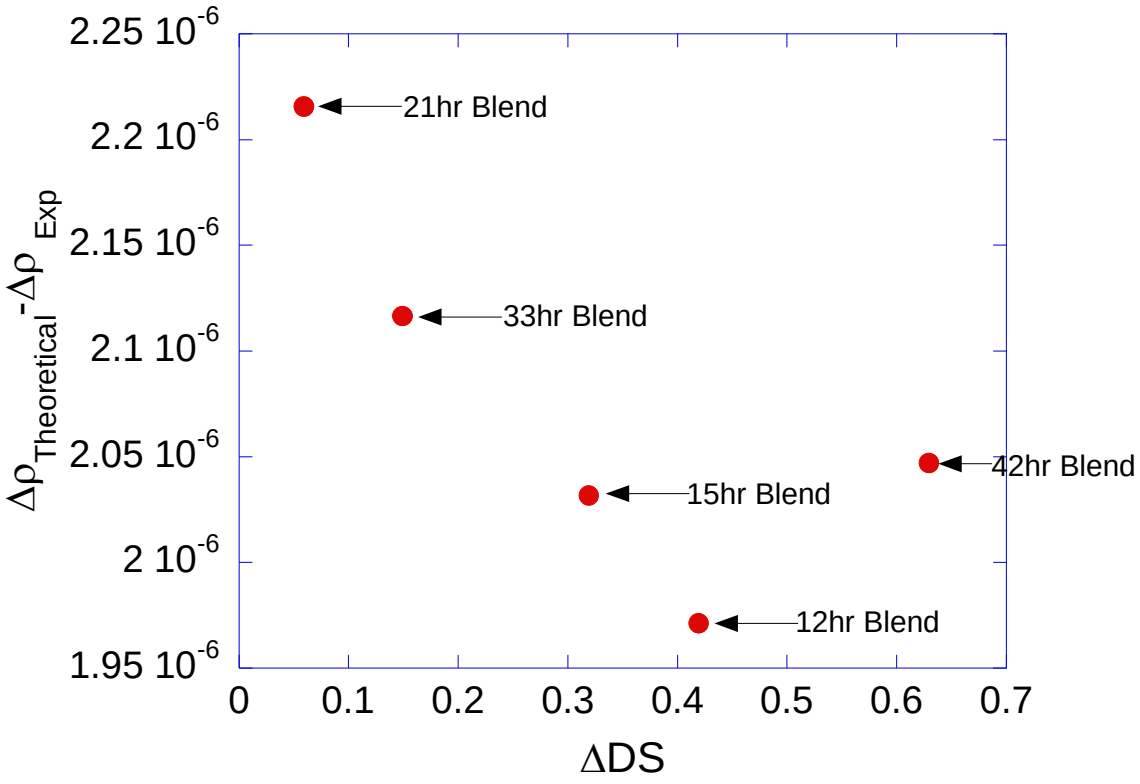

Figure 2.4. Difference between the difference in ideal scattering length density and difference in experimentally determined scattering length density as a function of the difference in degree of substitution of the two CA components that make up the two phases in the blend.

is a change in miscibility of the cellulose acetates that is dependent on the difference in DS of the two cellulose acetates in the blend.

To quantify the impact of cellulose acetate structure and ΔDS on blend miscibility, this data can be further analyzed to determine the composition of the coexisting phases in each blend. Knowledge of $<\eta^2>$ listed in Table 2.2 and $\Delta\rho_{exp}$ provides the required information to determine the composition of each phase in each studied blend. Each blend contains 2 phases, phase 1 and phase 2, where the volume fraction of each component (A and B) within the two phases are labeled φ_1^A, φ_1^B for phase 1 and φ_2^A, φ_2^B for phase 2. In the partially miscible system,

$$\varphi_2^A + \varphi_2^B = 1 \qquad (2.15)$$

and

$$\varphi_1^A + \varphi_1^B = 1 \qquad (2.16)$$

Each blend studied in this experiment is a 50/50 (v/v) blend such that the volume fractions of each cellulose acetate are equal and due to the nature of the synthesis of these copolymers the molecular weights of each copolymer is the same. With these criteria, Flory-Huggins theory is used to construct a phase diagram that summarizes the phase behavior of the mixture, and can be analyzed to determine the compositions of the two coexisting phases in the phase separated blend. This coexistence curve is determined from Equation 2.17

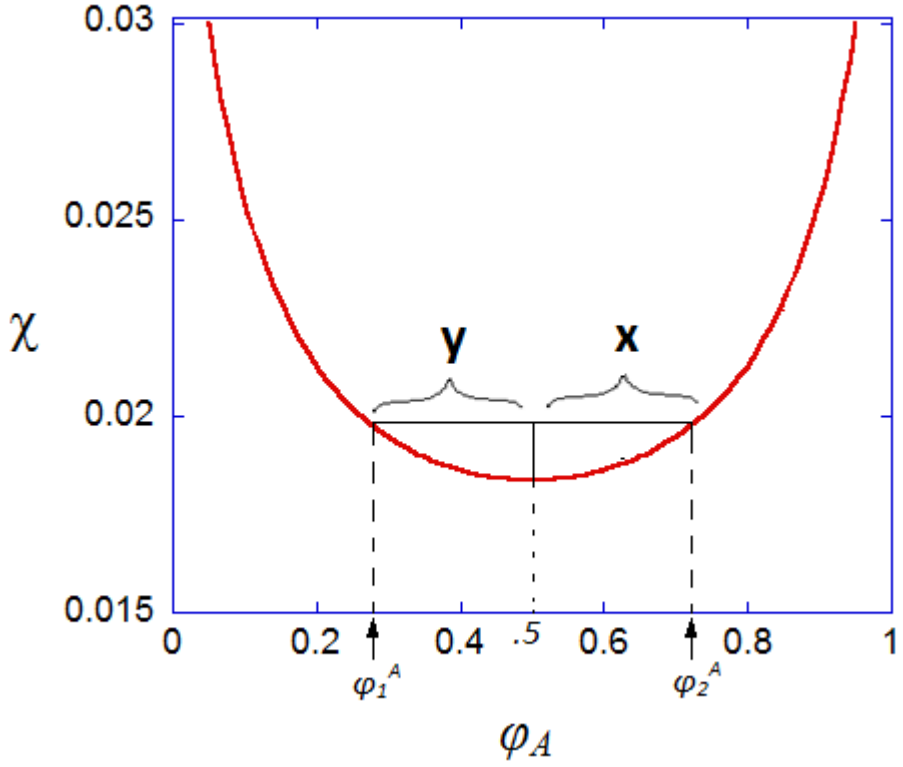

Figure 2.5 Calculated phase diagram of the binodal boundary of 50/50 Cellulose Acetate blends where $N_A=N_B=109$

$$\chi = \frac{\ln(\frac{\varphi}{1-\varphi})}{(2\varphi - 1)/N} \qquad (2.17)$$

where φ in Equation 2.17 is the volume fraction of one phase and N is the number of repeat units in the chain (109 for the cellulose acetate polymers used in this study).

The Flory interaction parameter, χ, characterizes the enthalpic interactions in the blend. This calculated phase diagram is shown in Figure 2.5 where χ is plotted as a function of φ_A. The area below the parabolic curve represents a 50/50 sample in a miscible, one phase region. But above the parabolic curve, the system phase separates into two phases, the properties of which can be readily determined from this phase diagram. For instance, at χ= 0.0195, the sample consists of two partially miscible phases, where the arrows indicate the compositions of polymer A in phase 1 and phase 2, denoted as φ_1^A and φ_2^A in the Figure. Moreover, the volume fractions of each phase that exists in this phase-separated system can be determined by the Lever Rule as

$$f_1 = \frac{x}{x+y} \qquad (2.18)$$

and

$$f_2 = \frac{y}{x+y} \qquad (2.19)$$

where *x* and *y* are the length of the lines shown in Figure 2.5. The symmetric 50/50 nature of the blend affords a degree of simplification of these relationships, which in turn allows

the determination of φ_1^A and φ_2^A from $\Delta\rho_{exp}$. The symmetry of the system gives $x = \varphi_2^A - .5$ and $y = .5 - \varphi_1^A$. The fact that $f_1=f_2$ leads to

$$\varphi_1^A + \varphi_2^A = 1 \quad (2.20)$$

combining Equations 2.15 and 2.20 gives the relation

$$\varphi_1^A = \varphi_2^B \quad (2.21)$$

These relationships and Equation 2.9 can then be used to determine the $\Delta\rho$ of any partially miscible blend with such symmetry as

$$\Delta\rho = (\rho_1 - \rho_2) = (\varphi_1^A \rho_A + \varphi_1^B \rho_B) - (\varphi_2^A \rho_A + \varphi_2^B \rho_B) \quad (2.22)$$

Factoring out ρ_A and ρ_B and substituting Equations 2.15, 2.16, and 2.21 into Equation 2.9 gives

$$\Delta\rho = (\rho_A - \rho_B)(2\varphi_1^A - 1) \quad (2.23)$$

Equation 2.23 will now be substituted into Equation 2.13 giving

$$< \eta^2 > = \frac{1}{4}(\rho_A - \rho_B)^2 (2\varphi_1^A - 1)^2 \quad (2.24)$$

Where ρ_A and ρ_B are the scattering length densities of the deuterated and protonated cellulose acetates in each blend, respectively, and are listed in Table 2.3. Applying the $\Delta\rho_{exp}$ values listed in Table 2.2 as $\rho_A - \rho_B$ in equation 2.24 and $< \eta^2 >$ values (also listed in Table 2.2.) Equation 2.24 provides the composition, φ_1^A, of each blend in the study.

These phase compositions are listed in Table 2.4, which further quantifies the change in miscibility with increasing ΔDS between cellulose acetate blend components. It is notable that the range of ΔDS of the blends used in this study gives measurable changes in the phase behavior of cellulose acetate blends. This is a key aspect of this study; the invariant extracted from the SANS data using Equation 13 allows the partial miscibility of each blend to be quantitatively determined.

Table 2.3. Degree substitution and calculation of the $\rho_{Theoretical}$ utilizing Equation 2.9 for cellulose acetate component used in the study.

Sample Name (by hours reacted)	Degree Substitution (DS)	$\Delta\rho_{Theoretical}$ (A^{-2})
d-24hr	2.19	4.178e-06
21hr	2.25	1.795E-06
33hr	2.04	1.801E-06
15hr	2.51	1.785E-06
12hr	2.61	1.780E-06
42hr	1.56	1.811e-06

2.4 Discussion

The miscibility of each cellulose acetate blend in this study is quantified by determining the composition of each phase in the blends as a function of ΔDS, and are presented in Table 2.4. Two components with very similar DS that are mixed are expected to be more soluble than two components with very different DS. Therefore a decrease in miscibility is expected with an increase in ΔDS. The results in Table 2.4 initially follow this trend where an increase in ΔDS of the blends leads to a decrease in miscibility. For instance, the 24hr sample (ΔDS=0.05) exhibits the highest miscibility of component A in phase 1 (φ_1^A=46%), while an increase of ΔDS=0.42 (the 12hr sample) results in a corresponding decrease in miscibility (φ_1^A=39%). The decrease in miscibility with ΔDS displays an almost linear trend, except for the 42hr sample. The miscibility of the 42hr blend increases (φ_1^A=42%) relative to the 12hr and 15hr samples, despite having the highest ΔDS (=.63). The 42hr blend, exemplifies that blending two cellulose acetates of varying DS is surprisingly complex. Despite the similarity between the repeat units in each component (all of cellulose acetate monomers) a slight change in the average acetate substituents along the backbone of the cellulose acetate chain can significantly affect the miscibility of the system.

This miscibility is controlled by the thermodynamic interactions that exist in these blends, and thus their inspection can provide insight into the underlying factors that control miscibility in cellulose acetate blends. Correlating the observed miscibility behavior of these blends to the structure of the components and their thermodynamic

Table 2.4. φ_1^A and φ_1^B of each cellulose acetate blend, which are the volume fraction of component A and B in phase 1

ΔDS	φ_1^A (x100)	φ_1^B (x100)
.05	46.2	53.8
.15	42.4	57.6
.32	41.1	58.9
.42	39.2	60.8
.63	42.2	57.8

interactions can therefore guide the rational control of the miscibility, properties, and structure of cellulose acetate blends.

The miscibility between two components in a blend is governed by thermodynamics. The mixing behavior of two components is determined by the change in free energy with mixing which is given by Equation 2.25.

$$\Delta G_m = \Delta H_m - T\Delta S_m \qquad (2.25)$$

where ΔG_m is the Gibbs free energy of mixing, ΔH_m is the enthalpy of mixing (also sometimes called the heat of mixing), which is determined by the enthalpic interactions in the system, and ΔS_m is the entropy of mixing. For a blend to be miscible, ΔG_m must be less than 0. When considering small-molecule or low molecular weight thermodynamics, the most important factor leading to miscibility is the entropy of mixing, as it is very large for many mixtures. Long-chain molecules, however, have a very small entropy of mixing. This leads to the enthalpy of mixing being dominant in determining miscibility and is directly related to the specific interactions among the blend components. Achieving miscibility ($\Delta G_m < 0$) of high molecular weight polymers, then, usually requires a negative ΔH_m to produce a negative ΔG_{mix}.

The specific interactions in the CA blends studied here are directly affected by changing the substituents along the chain backbone, which in turn alters ΔH_m. Therefore, the degree substitution of the blend components plays a key role in the determination of ΔH_m and miscibility. There are several types of intermolecular interactions present in cellulose acetate blends, which increase or decrease ΔH_m depending on their strength and extent of formation. Three types of interactions present in the cellulose acetate blends in

this study are dipole-dipole (Keesom) forces, London dispersion forces and hydrogen bonding.

Dipole-dipole forces occur between two permanent dipoles (such as the carbonyl groups in the acetate substituents) and, though stronger than dispersion forces, typically contribute less to ΔH_m simply due to the limited number of permanent dipoles relative to the instantaneous dipoles that can exist throughout the entire system. Thus, London-dispersion forces are considered the most significant van der Waals interaction in the CA blends used in this study.

London-dispersion forces occur between pairs of instantaneous dipoles or multi-poles. These correlated electronic movements induce favorable interactions promoting interaction between atoms and molecules. London-Dispersion forces are present in all chemical groups and typically represent the majority of interactions between components in a blend. The strength of the dispersive forces is determined by the correlation of electron movements between two entities, which is dependent on their electronic structure. The electronic structure of two similar molecules tends to have good correlation between movements of electrons and thus, significant dispersive forces, promoting mixing between the two components. Two components that are dissimilar (having different electronic structures), however, have poor correlated movements of electrons between the two entities and thus have very weak dispersive forces. In the cellulose acetate blends studied here, the blend that has the lowest ΔDS in Table 2.1 corresponds to a blend having the two most similar components of all the blends. The similarity between components then, promotes correlation of movement between electrons, which gives favorable dispersive forces and promotes miscibility between

blend components. As ΔDS is increased, the two blend components become increasingly dissimilar, leading to increasingly poor correlation between electron movements of the two dissimilar components while maintaining good correlation between self-similar components leading to a decrease in miscibility. Thus an increase in ΔDS yields weaker dispersive forces between the two blend components leading to a less miscible blend. This can be seen initially in Table 2.4 where the decreasing volume fraction of component B in phase 1 gradually moves toward immiscibility (i.e. 100% of B in phase 1 would be a fully immiscible system) as ΔDS increases.

Hydrogen bonding is another favorable non-bonding interaction between polymer chains in the CA blends. Attractive hydrogen bonding between two different components in a blend decreases ΔH_{mix} and thus promotes miscibility. Moreover, the extent of hydrogen bonding that can form between two polymers is dependent on the number of hydrogen bonding groups on the chain, which for cellulose acetates corresponds to the number of –OH groups. Inspection of Figure 1.2 shows that cellulose acetates with lower DS have more –OH groups, and thus should have more opportunity to participate in hydrogen bonding. Decreasing the degree substitution decreases the average number of acetate substituents per monomer and increases the average number of hydroxyls. Increasing the average number of hydroxyls promotes hydrogen bonding, leading to more favorable interactions in the system, presumably promoting miscibility. The interactions discussed above imply that an interplay between hydrogen bonding and van der Waals forces determines the extent of miscibility of the two cellulose acetates in the blend

Equation 2.25 establishes the thermodynamic criteria for miscibility and is primarily influence by ΔH_{mix} since the entropy of mixing for large molecules is minimal.

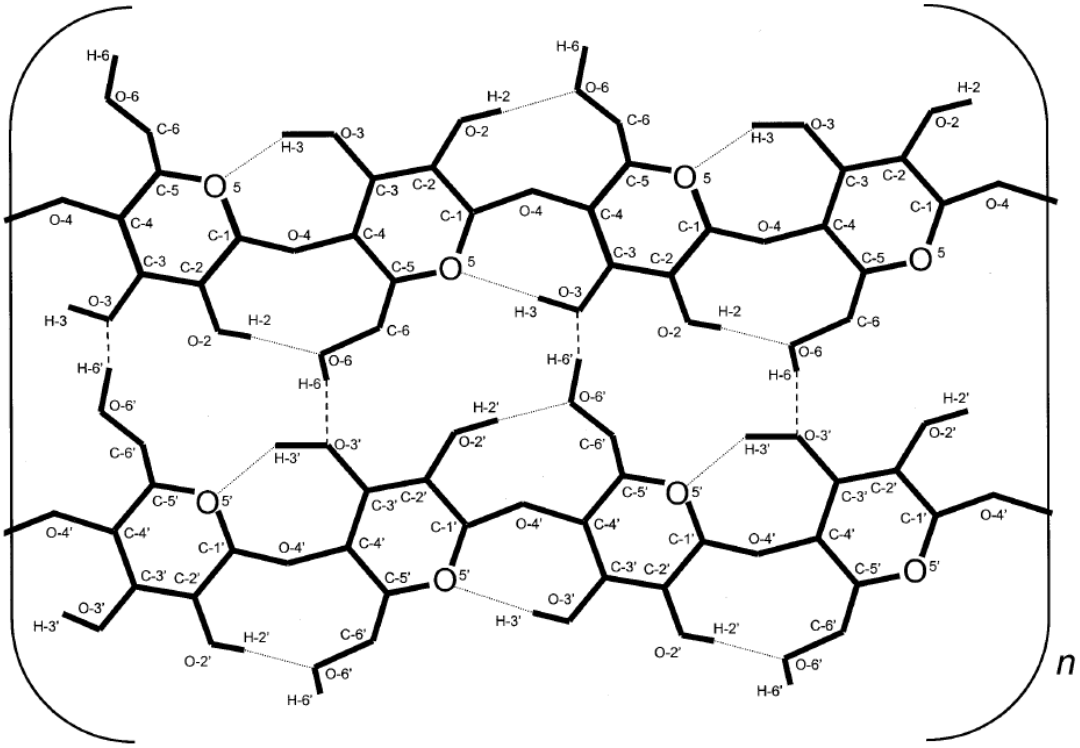

Figure 2.6. Hydrogen bonding scheme of inter and intrachain hydrogen bonding between cellulose chains from Gardner and Blackwell data.[125]

Equation 2.26 expands ΔH_{mix} to denote how it depends on the specific interactions present in the CA, demonstrating the role of Van der Waals interactions and hydrogen bonding in determining ΔH_m

$$\Delta H_{mix} = \left[\frac{1}{2}(H_{11} + H_{22}) - H_{12}\right]_{H-Bonding} + \left[\frac{1}{2}(H_{11} + H_{22}) - H_{12}\right]_{VDW} \qquad (2.26)$$

where H_{11} and H_{22} represent interactions between identical molecules, while H_{12} represents interactions between unlike molecules. Since the deuterated sample remains constant throughout the experiment, interactions among itself are constant, i.e. H_{22} is a constant. Equation 2.26 indicates that favorable, intermolecular hydrogen bonding and Van der Waals interactions will yield a decrease in ΔH_{mix} and thus promote miscibility; increased intramolecular interactions (H_{11} and H_{22}) are unfavorable leading to an increase in ΔH_{mix} and less miscibility.

Equation 2.26 highlights the difference between inter and intramolecular Hydrogen bonding and van der Waals forces; it will be useful to quantify the implicit energies associated with these interactions to better understand their impact on ΔH_{mix} and miscibility. The Flory interaction parameter, χ, is directly related to ΔH_m and quantifies the difference of interaction energies in a blend. $\chi < 0.5$ indicates the interactions are favorable and promote miscibility, while $\chi > 0.5$ indicates that the interactions are unfavorable with respect to miscibility, yielding a phase-separated system. The Flory parameter for a blend where each component has the same molecular weight at the binodal line is given by[121]

$$\chi_b = \frac{1}{2\varphi - 1}\left[\frac{\ln(\varphi)}{N} - \frac{\ln(1-\varphi)}{N}\right] \qquad (2.27)$$

where φ represents the volume fraction of component A in phase 1 (φ_1^A) and N is the degree of polymerization of the polymers (= 109 in this study). The χ of each CA blend is calculated using Equation 2.27 and is plotted in Figure 2.7, where χ initially increases with increasing ΔDS. The increase in χ indicates that the interactions are becoming less favorable with respect to miscibility as ΔDS increases.

As mentioned above, the DS of each component correlates to the number of hydroxyls that are present on the CA chain, and thus relates to the amount of functional groups that are present that can form hydrogen bonds. As the DS of the CA decreases, the number of hydroxyl groups increase, leading to a rise in the groups available to hydrogen bond. Figure 2.8 illustrates this qualitative trend of available hydrogen bonding functional groups with degree of substitution.

The number of functional groups that are available to form hydrogen bonds becomes important when considering the favorability of interactions in the system as van der Waals forces diminish in blends with higher ΔDS. The diminished van der Waals interactions may be mitigated, however, by the formation of favorable intermolecular hydrogen bonding interactions. In other words, an abundance of hydrogen bonding (from hydroxyls in the low DS components) can mitigate diminished intermolecular van der Waals forces by forming fewer, but stronger intermolecular hydrogen bonding between the two components, which lead to greater miscibility. The higher DS components, however, have significantly fewer hydroxyls and thus less opportunity to form hydrogen bonds and improve miscibility in blends with higher ΔDS.

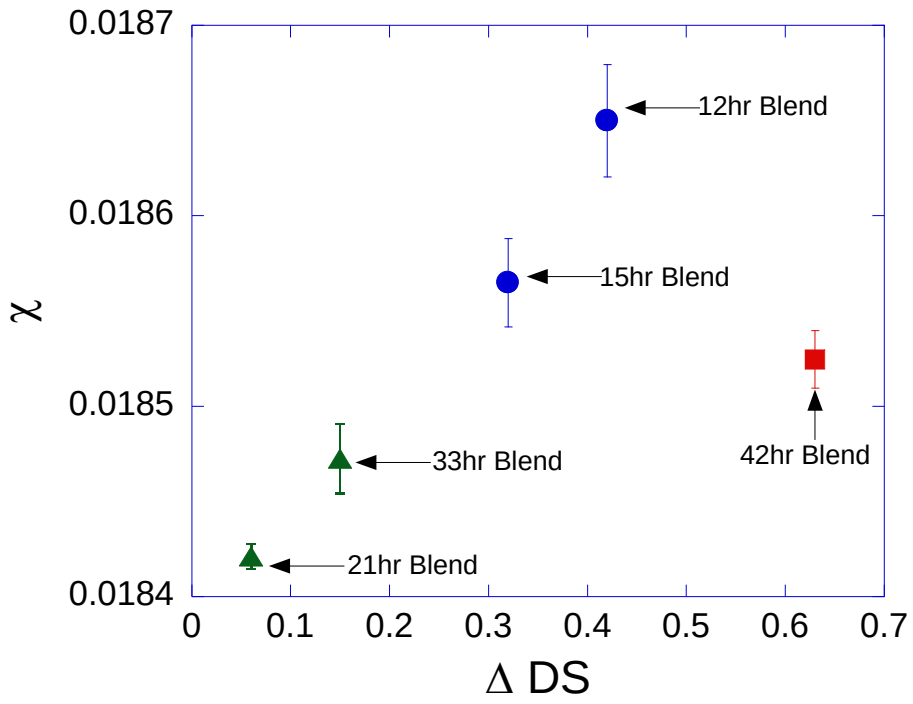

Figure 2.7. χ of the 21hr and 33hr blends (triangles), 12hr and 15hr blends (circles), and 42hr blend (square)

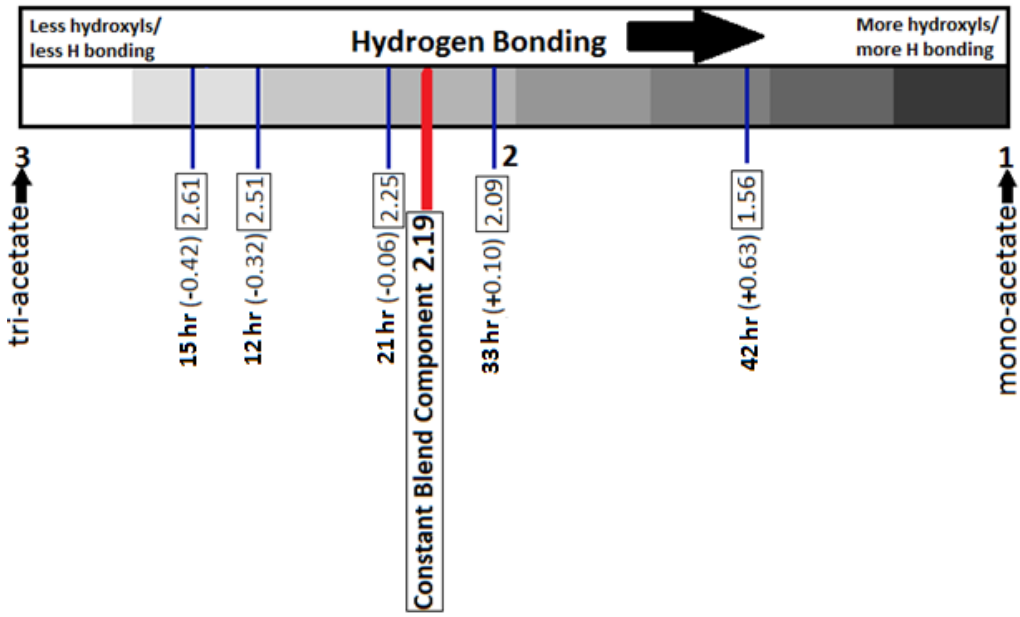

Figure 2.8. Degree of substitution of each polymer where the protonated cellulose acetates (blue lines) are each blended with the deuterated cellulose acetate. The arrow denotes an increase in the available hydrogen bonding when going from a triacetate to a monoacetate monomer structure.

The interaction parameter of the blends presented in Figure 2.7 underscore the interplay of the interactions discussed above. As ΔDS initially increases there is an overall increase in χ. This is explained by an overall decrease in favorable van der Waals forces due to the increasingly different electronic structure of the two components. The decrease in favorable van der Waals forces is most evident in the 12hr and 15hr blends, which have the highest χ values, indicating that there are fewer interactions that favor miscibility in the blend. The higher ΔDS, (thus weakened van der Waals forces) of these two blends lead to a decrease in favorable interactions. This is compounded by the fact that the 12hr and 15hr components have a high DS (meaning few hydroxyls) thus cannot readily form attractive hydrogen bonds that could improve miscibility. Conversely, the 42hr blend, has the highest ΔDS of all the blends, implying the largest difference between component structures of all the blends. This leads to the weakest favorable van der Waals forces, however it has a more favorable χ parameter than both the 12hr and 15hr blends. This is explained by an increase in favorable hydrogen bonding due to the extensive hydroxyl groups that are present, which can form attractive hydrogen bonds. The 21hr and 33hr blends have the lowest interaction parameter, indicating the most favorable interactions and greatest propensity for miscibility. This is explained by their lower ΔDS, and thus favorable Van der Waals interactions coupled with a significant number of hydroxyls that can form hydrogen bonds. The more favorable van der Waals forces and available hydrogen bonding each contribute to the interaction parameter, causing it to be lower than all other blends.

The above interpretation relies on the assumption that blends that contain cellulose acetates with higher DS will realize more intermolecular hydrogen bonding than similar blends that contain CAs with fewer hydroxyls. Fortunately, this can be tested with the cellulose acetates available for this study. Two blends with very similar ΔDS, but very different amount of hydroxyl groups present will be utilized in the study. The two blends are a blend of a CA with DS=2.19 blended with a CA with DS= 2.61 and a blend of the same CA with DS=2.19 and a CA with DS = 1.78. Both blends have a ΔDS ~ 0.41-0.42, but the CA with DS=1.78 has significantly more –OH groups present that the CA with DS = 2.61. Thus, if the presented interpretation is correct, the second blend will exhibit more intermolecular hydrogen bonding than the first.

Previous studies have utilized FTIR as a method to provide insight into the role of hydrogen bonding in cellulose acetates that can be used as guides. For instance, Yin *et al.* studied the role of thermodynamic interactions on the miscibility in cellulose diacetate/poly(vinyl pyrrolidone) (PVP) blends.[126] Their results provide evidence of a strong interaction between the hydroxyl groups of the cellulose diacetate and the carbonyl groups in the PVP. The characteristic hydroxyl peak in FTIR exhibits a broadening and shift of about 30 cm^{-1} toward a lower frequency with the addition of 20% PVP to cellulose acetate, which is interpreted to indicate an increase in hydrogen bonding.

Similarly, the FTIR spectra of the DS=2.19/DS=2.61 and the DS=2.19/DS=1.78 blends are obtained and displayed in Figure 2.9, which shows the characteristic –OH peaks in the range of 3250 cm^{-1}-3675 cm^{-1}. It is well known that free hydroxyls (i.e. not hydrogen bonded) show a characteristic peak at a higher frequency (~ 3660 cm^{-1}) than hydroxyls that are hydrogen bonded.[10,126,127] Thus, an increase in hydrogen bonding shifts

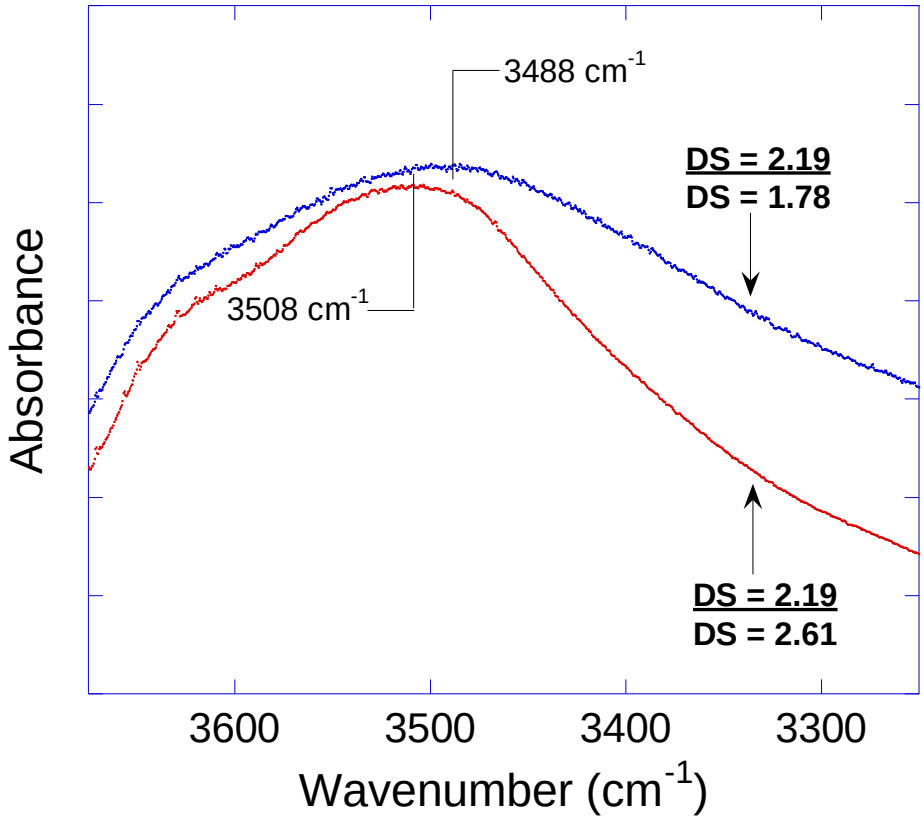

Figure 2.9. FTIR spectra of 12hr/24hr and 36hr/24hr blends in the range of 3250 cm^{-1} to 3675 cm^{-1}

the hydroxyl peak to a lower frequency, while simultaneously broadening the peak. The peak in the spectrum of the DS=2.19/DS=1.78 blend shifts by 20 cm^{-1} toward lower frequency relative to the peak of the DS=2.19/DS=2.61 blend spectrum. The broadening of the –OH peak and shift to a lower frequency indicates an increase of hydrogen bonding.[10,126-128]

Thus, these two blends have approximately the same ΔDS, however FTIR shows that the blend with more –OH groups exhibits more intermolecular hydrogen bonding. These results also support the interpretation that the 42hr blend that is examined in the SANS experiment will also exhibit very similar interactions. This supports the interpretation that hydrogen bonding is prevalent in the 42hr blend, which leads to more favorable interactions and greater miscibility than the 12hr and 15hr blends, despite the fact that the 42hr blend has the highest ΔDS.

Our results clearly show that the difference in degree of substitution between two cellulose acetate copolymers impacts the miscibility of the blend. Moreover, careful analysis of the data indicates that the actual structure of the components is also important in that it determines the ability to form intermolecular interactions that promote miscibility. The results indicate that the extent of miscibility for given ΔDS will be higher when the DS is lower (0.5-1.5) than when DS is higher (2-3). Therefore, this study concludes that the blend miscibility of cellulose acetate is highly dependent on ΔDS and on the copolymer substituents, giving improved miscibility at lower ΔDS values and where hydroxyls are more abundant, thus providing insight into the impact of interactions on the miscibility of cellulose acetate blends.

2.5 Conclusion

The miscibility of a series of cellulose acetate blends has been studied using small-angle neutron scattering. These results demonstrate that the difference in acetate substituents along the copolymer backbone (difference in degree of substitution, or ΔDS) between the two blended cellulose acetate copolymers significantly impacts miscibility of the blend. The miscibility decreases with increasing difference in degree substitution indicating a decrease in favorable interactions. The Flory interaction parameter quantifies the intermolecular interaction energies as they relate to miscibility. Analysis of the Flory parameter indicates that increasing structural differences between blend components produces less favorable interactions with increasing ΔDS. An explanation of this decrease is that the increasingly different copolymer structures of the blend components lead to diminishing favorable van der Waals forces. These results also indicate that the structure of the individual blend components is an important factor in blend miscibility, where the result show that substituents that can form beneficial intermolecular interactions promote mixing between components.

Moreover, these results provide evidence that specific interactions can lead to improved miscibility for blend components having more hydroxyl substituents (i.e. a DS between ~0.5-1.5) but not for blend components having more acetate substituents (i.e. a higher DS between ~2-3). One explanation is that the hydroxyls in the lower DS components actuate favorable hydrogen bonding, augmenting interactions between the

blend components. This is consistent with FTIR data, which indicates an increase in hydrogen bonding of a blend having a lower DS component. We interpret these results to mean that the presence of hydroxyls and their participation in hydrogen bonding promotes miscibility of the blend to mitigate diminishing van der Waals forces between components. The results presented here demonstrate that both ΔDS and the precise structure of the individual components impact the interactions that determine miscibility in cellulose acetate blends. These results provide detailed insight into the impact of degree substitution on blend miscibility, highlighting the role of specific interactions and their impact the phase behavior of cellulose acetate blends.

CHAPTER 3: UNDERSTANDING THE INFLUENCE OF THERMODYNAMIC INTERACTIONS ON MISCIBLE POLYMER BLEND DYNAMICS

3.1 Introduction

The previous chapter focused on the impact of non-bonding interactions on the miscibility of a polymer blend. These non-bonding interactions can also affect many other properties, including the polymer blend dynamics. Multiple studies have shown that the composition of the region surrounding a polymer segment, or local environment strongly affects the dynamics of each component in a miscible polymer blend. This fact provides the basis for recent models, such as the Lodge-McLeish (L-M) model, that predict the dynamics of the components in a miscible polymer blend based on the estimation of the composition of the local environment around each polymer segment.

These models only take into account the structure of the polymers and the composition of the blend, but do not include the impact of any intermolecular interactions that may exist between the two components. This is important because recent studies indicate that thermodynamic interactions can significantly alter the local environment and, in turn, the dynamics of the blend components.[81,88,90] There is therefore a need to more thoroughly understand the role of thermodynamic interactions of the dynamics of miscible polymer blends.

With this in mind, we have completed a rheological study to document the effect of thermodynamic interactions on the dynamics of a miscible blend that contains a copolymer in a homopolymer matrix. A homopolymer/copolymer blend is used to complete this study, focusing on a styrene/methyl methacrylate system since the thermodynamic interactions between the two polymers in this blend will vary with copolymer composition, which is easily manipulated. The presence of the repulsive interaction between S and MMA monomers allows the controlled introduction of

thermodynamic interactions into the system. Further, we correlate the results to the L-M theory, testing the underlying principles that govern this model.

3.2 Experimental

3.2.1. Polymer Synthesis

The PS-*ran*-PMMA copolymers (synthesized by Dr. Dias Linton) and PMMA homopolymer used in this study were synthesized by atom transfer radical polymerization. In this reaction, CuBr, ethyl α-bromoisobutyrate (EBIB), and 2,2 bypyridine were added first to a reaction vessel and then the monomer and solvent were added to ensure no CuBr remained on the side of the flask. The flask was then frozen, pumped free of air, thawed and repeated for a total of three times to ensure no air remained in the flask. The reaction was kept at 80 °C for 3 hours and stopped at 30% conversion. Methyl methacrylate, CuBr, EBIB, and 2,2 bypyridine were purchased from Sigma Aldrich. The EBIB and 2,2 bypyridine were used as received. CuBr was purified by dissolving in glacial acetic acid and washing in absolute ethanol. The inhibitor was removed from the MMA monomer by distillation, starting at room temperature and increasing the temperature by ~5^{0}C increments. The first fraction (~10%) was discarded and the rest was distilled as pure MMA monomer.

3.2.2. Polymer Characterization

3.2.2.1.Nuclear Magnetic Resonance

The composition and sequence distribution of the PS-*ran*-PMMA copolymers was determined by ^{1}H NMR spectroscopy (Varian 300 MHz). ^{1}H NMR verified the random nature of the linear copolymers as in previous studies.[129] Sample concentrations were 10

mg/mL in deuterated Chloroform and the chemical shift scale was referenced to the tetramethylsilane peak at 0 ppm. A typical spectrum is presented in the appendix.

3.2.2.2. Size Exclusion Chromatography

The molecular weight characteristics of the polymers were obtained by size exclusion chromatography (SEC). SEC analysis of the PS-*ran*-PMMA and PMMA homopolymer were performed at room temperature (20°C) with a flow rate of 1ml/min using polystyrene standards. Measurements were completed on a Polymer Labs GPC-20 instrument equipped with two 300mm x 7.5mm Polymer Labs 5μm Mixed C columns and a 50 mm x 7.5 mm Polymer Labs 5 μm guard column with a Knauer K-2301 differential refractometer as a detector. Samples (filtered through a 0.45 μm syringe filter prior to injection) were at 1 mg/mL concentration and HPLC grade THF (100 ppm BHT stabilized) was used as the mobile phase.

3.2.2.3. Rheological Measurements

Dynamic viscosity measurements were completed with an ARES rheometer (Rheometric Scientific) using 25 mm parallel plate geometry. Each sample consists of 10% (v/v) copolymer and 90% (v/v) homopolymer. Each sample was heated under vacuum to 140-150 °C for 1-2 hours, removing all air bubbles, cooled to room temperature and loaded into the rheometer at room temperature and heated to 150 °C. Gap spacings were carefully monitored, but kept to approximately 1 mm for each measurement. The sample and toolset were enclosed in a nitrogen convection oven at all times. Isothermal frequency sweeps were first performed to ensure measurements are in the linear viscoelastic regime, where the complex modulus η* was measured at

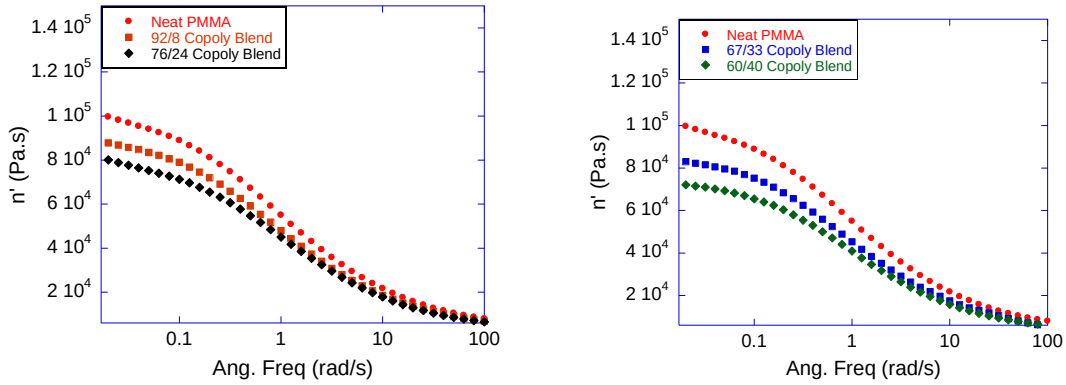

Figure 3.1. Dynamic viscosity results of the PMMA homopolymer (circles) and blends of 10% PMMA/ 90% PMMA-PS random copolymer (squares) where the PMMA-PS copolymer compositions are (a.) 92/8 (b.) 76/24 (c.) 67/33 and (d.) 60/40

frequencies, ω, between 100 and 0.01 rad/s. The zero-shear viscosity, η_o, is taken as the average of the last 4 data points at the low-frequency plateau.

3.3. Results

The composition and molecular weight of the random copolymers and homopolymers used in this study are listed in Table 3.1. Each blend in this study consists of 10% (w/w) copolymer and 90% PMMA homopolymer. The dynamic viscosity (η') of each 90/10 (w/w) homopolymer/random copolymer blend was experimentally determined rheologically. The absence of a maximum in G'' with frequency (not shown) verifies that these polymers are unentangled, as is expected given the low molecular weights of all polymers employed in this study and the known entanglement molecular weights for PS and PMMA (31,000g/mol and 30,000 g/mol, respectively).[130] For each homopolymer-copolymer blend, the zero shear viscosity plateau is observed at low frequency (ω→0). The dynamic viscosities of the samples are shown in Figure 3.1 where η' is plotted as a function of angular frequency for each PS-*ran*-PMMA /PMMA blend, and includes the flow behavior of the PMMA homopolymer. Each blend displays a η' that is lower than that of the neat PMMA matrix. This reduction reflects a decrease in viscosity due to the addition of the copolymer added to the homopolymer matrix. The extent of the viscosity decrease is somewhat unexpected in that the copolymer is only 10% of the sample, and the amount of styrene present in the system is very low. Clearly, the copolymer has a significant impact on the dynamics of the blend, even at these low loadings.

To more quantitatively analyze this behavior, the zero shear viscosity (η_o) of each blend is determined by the value of η'(ω) in the limit ω→0. Extraction of the contribution of the PS-PMMA copolymer to η_o provides a quantitative measure of the

Table 3.1. Copolymer composition, number average molecular weight, and weight average molecular weight of the random copolymers and PMMA homopolymer with which each copolymer is blended.

Copolymer Composition (mol % MMA)	M_n (g/mol)	M_w (g/mol)
1.00 (neat PMMA)	10900	17200
0.92000	16300	22600
0.76000	12300	16400
0.67000	10700	15500
0.60000	9200	13100

impact of the styrene in the copolymer on the dynamics of the homopolymer/copolymer blends.

Two approaches are often used to extract the contribution of each component of a polymer blend to the measured blend viscosity. The first approach utilizes the Rouse model[131,132] as

$$\eta_{oBlend}(\omega) = \varphi_{PMMA}\,\eta_{oPMMA}(\omega) + \varphi_{Copoly}\eta_{oCopoly}(\omega) \quad (3.1)$$

where φ_{PMMA} and φ_{Copoly} are the volume fractions of PMMA and copolymer in the blend. Equation 3.1 is first used to determine the zero shear viscosity of the copolymer as it exists in the PMMA matrix. This requires that η_{oPMMA} and η_{oBlend} be known, allowing the solution of Equation 3.1 to determine $\eta_{oCopoly}$, the zero shear viscosity of the copolymer in the blend. The results of this analysis are given in Figure 3.2, which plots the zero shear viscosity of the copolymer as a function of the composition of the copolymer. At the extremes of the plot are the zero shear viscosities of the neat PS and PMMA components, which were also determined experimentally. The line between the neat components represents the compositional average zero shear viscosity of S and MMA. Inspection of Figure 3.2 shows that the calculated values of the zero shear viscosities of the copolymers using this analysis are unrealistic, in that this analysis provides negative viscosities. Clearly, applying the Rouse model to model this aspect of the blend is not valid, and therefore another analysis must be attempted.

Another approach that can be employed is to apply the mixing rule as described by Arrhenius for the viscosities of small molecule mixtures[133,134] as given in Equation 2.

$$\mathrm{Log}(\eta_0)_{Blend} = \varphi_{PMMA}\mathrm{Log}(\eta_0)_{PMMA} + \varphi_{copoly}\mathrm{Log}(\eta_0)_{Copoly} \quad (3.2)$$

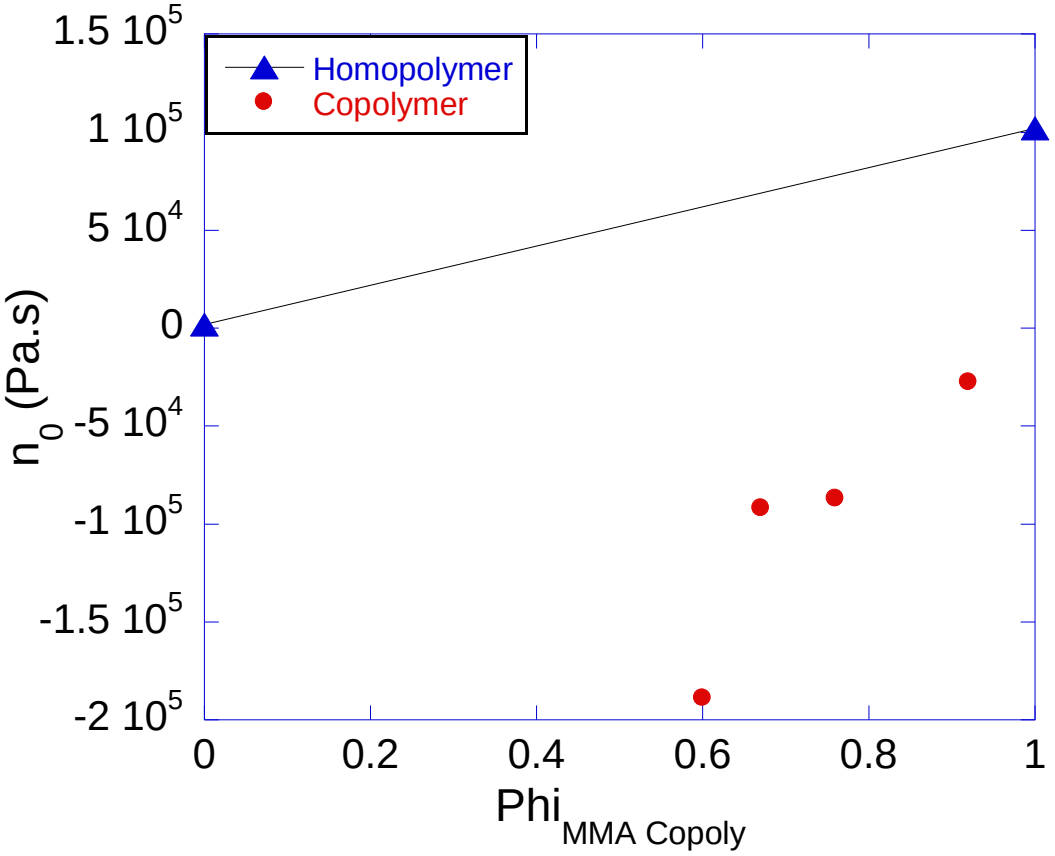

Figure 3.2. Copolymer viscosities from each homopolymer/copolymer blend (circles) obtained using Equation 3.1. Homopolymer viscosities are denoted as triangles

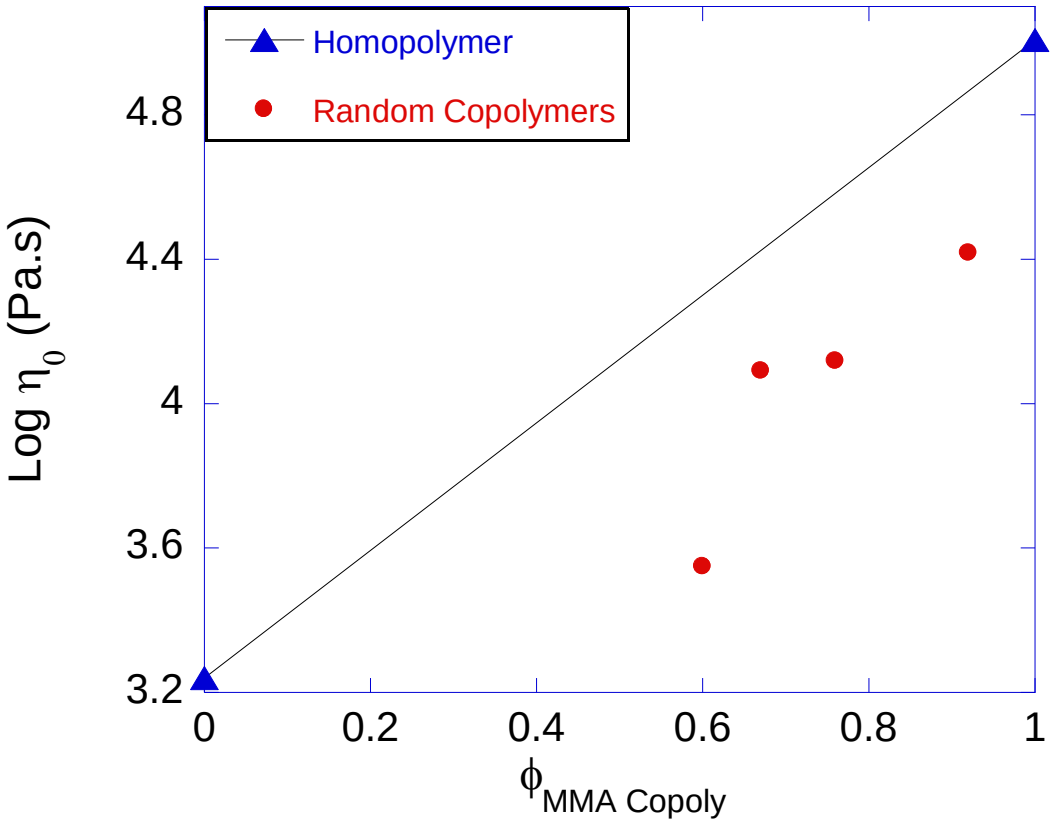

Figure 3.3. Zero-shear viscosities of the PS-*ran*-PMMA copolymers as obtained by Equation 3.2 (circles). The zero-shear viscosities of the neat PS and PMMA homopolymers are shown as triangles. The line between the neat components is merely a guide to the eye.

In this equation, φ_{PMMA} and φ_{copoly} are the volume fractions of PMMA and copolymer in the blend. The copolymer zero shear viscosities that are obtained using Equation 3.2 are presented in Figure 3.3. The line is a guide to the eye and represents a log-weighted average of the zero shear viscosities of the two homopolymers. The friction factors of PS/PMMA disordered diblock copolymers in a PMMA matrix have been shown to follow this compositional average.[89] The viscosities of the random copolymers determined by this method are reasonable values, however each viscosity falls below that of a compositionally averaged copolymer.

The segmental friction factor, ζ, provides a parameter that can be used to characterize the composition dependence of local dynamics. For the molecular weights used in this study, the Rouse model can be employed to obtain the segmental friction factor, as all components are well below their entanglement molecular weights. The Rouse model describes the chain dynamics of unentangled polymer chains and this provides a method to determine ζ of the copolymers directly.

The Rouse model describes the relationship between the zero shear viscosity and the monomeric friction factor for unentangled polymer chains as[17]

$$\zeta = \frac{m_0^2}{M}\frac{\eta_0}{\rho N_{AV} b^2} \quad (3.3)$$

Recall that the utilization of the Rouse model in Equation 3.1 produced unreasonable flow behavior of the copolymer, indicating that the distribution of relaxation times for these blends differs from Rouse behavior. However, given a reasonable zero shear viscosity of the copolymer (i.e. from the Arrhenius model) the basic relations of the Rouse model in Equation 3.3 are, in principle, applicable to linear copolymers[135] due to

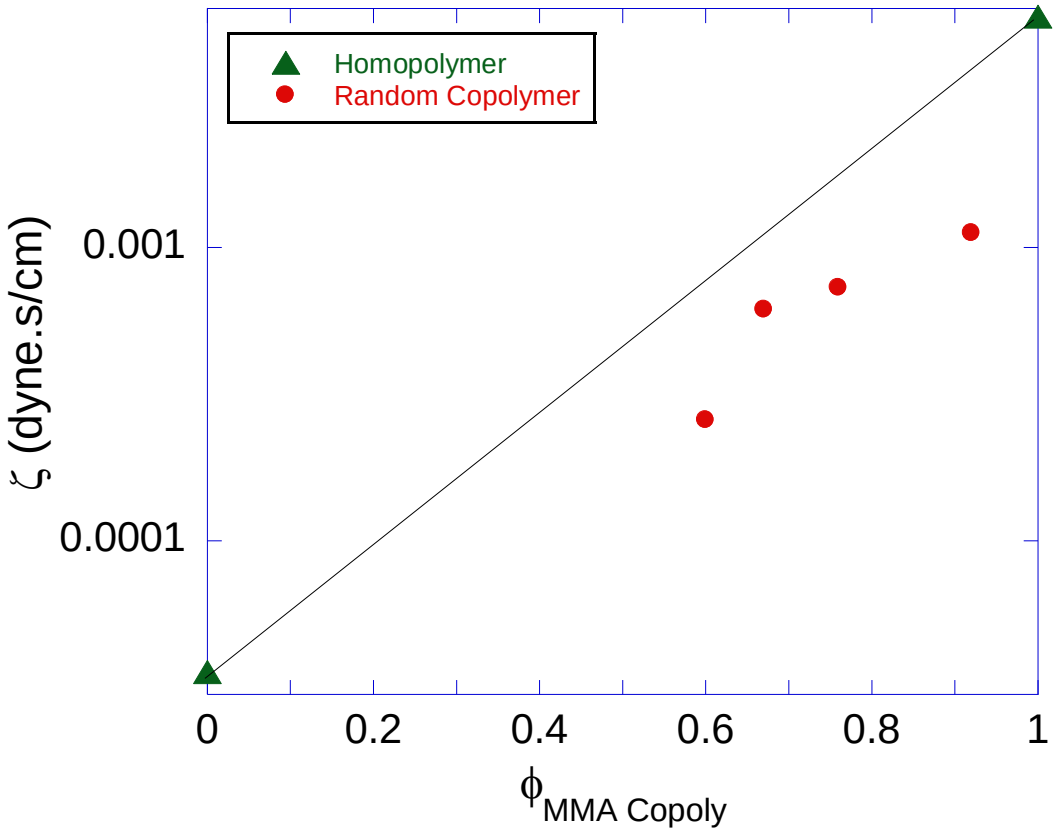

Figure 3.4. Friction factor of the copolymers (circles) determined using η_o reported in Figure 3.3 and Eq. 3.3. The friction factors of the neat PS and PMMA homopolymers are also presented as the triangles.

the unentangled nature of the sample, allowing calculation of the segmental friction factor. For the analysis employed here, the monomer molecular weight, m_0, density, ρ, and statistical segment length, b, of the copolymers are compositional averages using neat component values reported in the literature.[70] The molecular weight, M, is the molecular weight of the copolymer being considered. The friction factor for each copolymer is thus readily calculated using Equation 3.3.

The zero shear viscosity used to determine ζ using Equation 3.3 corresponds to the copolymer zero shear viscosity that is determined by evaluating the experimental data using Equation 3.2. The effective friction factor of each copolymer chain in the PMMA matrix as determined with this analysis is shown in Figure 3.4. The friction factors for PS and PMMA homopolymers are also shown in Figure 3.4 and the line is a guide to the eye that represents a log-weighted average between the segmental friction factors of the two homopolymers. Figure 3.4 demonstrates that the friction factor for the random copolymers are up to an order of magnitude lower than what is expected from a compositional average of the two homopolymers. This is consistent with our previous simulation results[88] and neutron reflectivity studies[81] which indicate that the thermodynamic interactions between immiscible polymers can have a strong impact on the dynamics and structure of random copolymers dispersed in a homopolymer matrix.

3.4. Discussion

The zero shear viscosities of the copolymers as determined by applying the Rouse model to the blend viscosity results are presented in Figure 3.2, including negative values that represent physically unrealistic results. Thus, the Rouse model does not accurately describe the dynamics of this blend system despite the fact that, to a good approximation,

the model has been shown to describe the dynamics of a polymer chain in a melt.[40,89] The Rouse model treats the dynamics of a Gaussian chain in a heat bath, which implicitly assumes that on the length and time scales of interest, all forces from local potentials of a given polymer have already decayed.[40] Entropic forces arising from the conformational entropy of the polymer chain then determine its dynamics. It is significant that copolymer viscosities are not only below the compositional average, but are less than zero, indicating that there are factors in this system, such as intermolecular interactions, that are not accounted for by this application of the Rouse model.

Using the Arrhenius equation as described above (Eq. 3.2), the zero shear viscosities of the copolymers in the blend are determined and presented in Figure 3.3. The zero shear viscosities of the copolymers determined by fitting the experimental data to the Arrhenius model still differ by up to an order of magnitude from the compositional average. One explanation for the success of the Arrhenius model is that this rule corresponds to the case where the effective activation energy of the flow process is a volume-weighted average of the pure component values. In this case, the activation energy can be considered to be the amount of energy needed for flow to occur. In this sense, various factors determine the activation energy of flow, such as the available volume of the polymer to move (free volume) and molecular interactions within the system (e.g. attraction between molecules leads to a higher activation energy for flow). This may explain why the Arrhenius model gives significantly better results, in that the repulsive interaction between styrene and MMA are partially accounted for in the increase flow behavior of the copolymer.

A major objective in understanding polymer blend dynamics is to devise a predictive scheme for the properties of miscible blends. For instance, Equation 3.3 outlines how the friction factor, ζ, relates to rheological properties; the opposite approach of predicting the friction factor in miscible polymer blends *a priori* has inspired considerable effort within the polymer community. Prediction of such friction factors provides the foundation to predict macroscopic properties that affect polymer processing and end-use properties. It is important, then, to test the ability of theoretical models to predict blend rheology, including the comparison of experimentally determined friction factors to theoretical predictions. Though first principle calculation of the ζ in miscible blends is not yet possible, considerable gains have been made to better understand the composition and temperature dependence of ζ in miscible polymer blends.[136] It is widely accepted that, in a blend of two components, ζ is influenced by the local environment, or region surrounding a component segment.

Numerous studies have documented a unique and composition dependent local environment for each component in the blend.[10] These phenomena have been attributed to local heterogeneities in composition, such that the two components experience different local environments or distributions of environments at the segmental level. The deviation of the dynamics of the PS/PMMA system employed here from a compositional average is even more dramatic than other commonly studied systems, or can be accounted for with just connectivity effects. Since PMMA has a higher friction factor than PS, it is expected that the friction factor of the system will increase with increasing global MMA content. The results presented here agree with this trend qualitatively as shown by the upward trend of zero shear viscosities in Figure 3.3 with increased MMA

content. In most miscible polymer blends, the motion of the faster component is not significantly constrained by the slower molecule, and therefore, in this system, one would expect that the styrene component would not be slowed. Interestingly, the fact that styrene is a small fraction of the blend implies that it is effectively "surrounded" by the slower PMMA component if the system were homogeneously mixed at the segmental length scale. The experimental data, however, shows that this is not the case. The deviation of the dynamics of the copolymer from the compositional average, implies that the composition around the copolymer chain is higher in styrene than what is expected from the compositional average.

the styrene and MMA monomers cause the copolymer chain to collapse upon itself to minimize these interactions, creating a higher "local" styrene concentration than the global concentration.

Comparing the experimental results here with the predictions of the L-M model provides further insight into the underlying physics that govern these results. The Lodge-McLeish theory is based on two postulates. One postulate stipulates that within a volume V centered on monomer A, there exists an excess of A monomers relative to the average bulk concentration. This is simply due to chain connectivity; a covalently bound chain of "A" monomers (i.e. a homopolymer) guarantees a certain number of other A monomers in its vicinity. Thus, in a binary blend of homopolymers, a typical A monomer (typical meaning not near a chain end) on average experiences an effective local concentration that is richer in A monomers than the bulk composition. The L-M theory seeks to quantify this local concentration and predict the dynamics of each component in miscible polymer blends based on the local concentration. The L-M theory, however, does not take

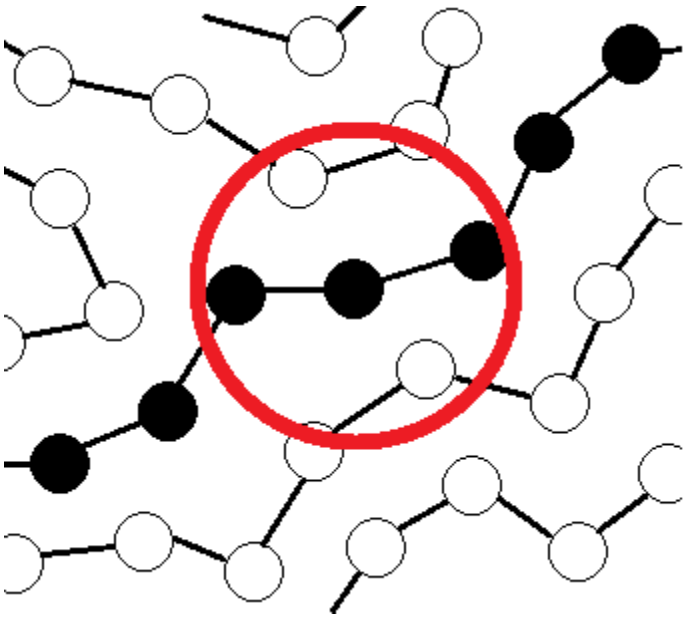

Figure 3.5. Self-concentration of a polymer chain. The red circle is centered around a monomer on the black polymer chain, which is surrounded by white chains. The concentration of black monomers in the circle is higher than the surrounding white monomers, creating an enrichment of black segments in the local volume. The composition in this circle forms the self-concentration utilized in the Lodge-McLeish model.

into account thermodynamic interactions between the two components, instead using purely geometric (connectivity) arguments to predict the effective composition around any monomer in a blend. The second postulate identifies the length scale of this local concentration. This is determined by the Kuhn length (l_K), which is a well-defined property for any polymer chain, $l_K=C_\infty l$, where C_∞ is the characteristic ratio and l is the length of the average backbone bond. The volume around a Kuhn length segment is $V\sim l_k^3$ and the fastest segmental relaxation occurs within this volume, which is influenced by the concentration of monomers within this volume. This concentration, the self-concentration, φ_s, is determined by the volume occupied by a Kuhn length's worth of monomers, divided by V:

$$\Phi_s = \frac{C_\infty M_0}{\kappa \rho N_{AV} V} \qquad (3.4)$$

where M_0 is the repeat unit molar mass, κ is the number of backbone bonds per repeat unit, ρ is the density, N_{AV} is the average number of monomers per repeat unit and $V=l_k^3$ is the volume around a Kuhn segment of length l_k. A simple explanation of self-concentration is that a polymer segment must have a certain number of neighboring segments from the same chain due to the covalent bond connecting the monomers. In this way, chain connectivity biases the composition of the environment surrounding a particular polymer segment and enriches the local environment in polymer segments of the same type, creating a self-concentration that differs from the global blend composition. Figure 3.5 illustrates the self-concentration of a polymer chain. The effective local concentration of a polymer segment in a miscible polymer blend by the L-M theory is then given by

$$\varphi_{eff} = \varphi_s + (1 - \varphi_s)\varphi \qquad (3.5)$$

where φ_s is the self-concentration and φ is the bulk composition for the two-component blend.

Comparison of experimental data to predictions of the L-M theory provides a critical test of the model's ability to make accurate predictions of the dynamics in miscible blends. If the interaction between styrene and MMA is not important, the experimental data will mimic the predictions of the L-M model. To test this, the experimental and theoretical concentration of styrene within local environment of the copolymer chain can be compared.

Determination of the composition of the local environment around a chain first requires determination of φ_s and φ_{eff} for a segment on a copolymer chain. These values are calculated for our system by assuming a compositional average of each entity in Equation 3.4 based on the respective values of PS and PMMA that are reported in literature[70]. φ_s^{copoly} and φ_{eff}^{copoly} are the self-concentration of the copolymer and the blend's predicted effective concentration of the random copolymers calculated using these average values. The effective local concentration of styrene (φ_{eff}^{s}) for the copolymer describes the concentration of styrene around a segment within the copolymer and is calculated using the L-M theory. Physically, the effective composition of styrene is the connectivity-biased composition of styrene monomers within the segmental volume $V=l_k^3$. φ_{eff}^{s} is determined using φ_{eff}^{copoly} and the stoichiometric styrene composition of the copolymer, φ_A:

$$\varphi_{eff}^{s} = \varphi_A \text{ x } \varphi_{eff}^{copoly} \qquad (3.6)$$

Table 3.2. Lodge-McLeish predictions of the self-concentration of the copolymer (φ_s^{copoly}), the effective concentration of the copolymer in the blend(φ_{eff}^{copoly}), and the effective styrene concentration (φ_{eff}^{s}) of the effective copolymer concentration.

φ_A	φ_s^{copoly}	φ_{eff}^{copoly}	φ_{eff}^{s}
0.08	0.2516	0.326	0.026
0.24	0.2548	0.329	0.079
0.33	0.2566	0.331	0.109
0.40	0.2580	0.332	0.133

The results of this calculation for all copolymers examined in this study are given in Table 3.2.

To compare this result to the experimental results, the friction factor of the copolymer as presented in Figure 3.4 is examined. These experimental results indicate that there is an effective increase of the local styrene composition near the copolymer, lowering the observed segmental friction factor. An alternative way to describe this is that the experimental results indicate an effective increase of the local concentration of the *copolymer* in the *blend*. The L-M predictions of φ_{eff}^{S} and φ_{eff}^{copoly} each reflect this experimental observation, indicating an increase in the predicted local styrene concentration relative to its global concentration. For example the experimental blends each contain 10% copolymer, however the L-M model indicates a significantly higher local copolymer concentration, predicting that the effective copolymer concentration (φ_{eff}^{copoly}) in the blend is ~33% for each copolymer blend. Of course, an increase in copolymer concentration in the blend corresponds to an effective increase in styrene concentration (φ_{eff}^{S}) in the blend. For instance the model predicts that the 92/8 copolymer blend has an effective copolymer concentration of 32.6% copolymer. A 32.6% copolymer/homopolymer blend of 92/8 PMMA/PS copolymer gives an effective styrene concentration, φ_{eff}^{S}, of 2.6% ($0.08 \times 0.326 = 0.026$) as calculated by Equation 3.6 and presented in Table 3.2. This is much higher than the global concentration of styrene in this blend, ($0.08 \times 0.02 = 0.008$). Therefore the L-M model predicts a higher local copolymer concentration and thus a higher local concentration of styrene around the copolymer than what is expected from a homogeneously dispersed blend of the same composition. The increase in styrene content reflects the model's connectivity bias on the

composition of the environment surrounding the polymer chain, indicating an enriched local environment of styrene around the copolymer. Thus, the L-M results are promising in that they qualitatively agree with the experimental results demonstrating an increase of styrene concentration around the copolymer.

Quantitative comparison between experimental results and the L-M predictions further test the applicability of this model. A method that relates φ_{eff}^{S} to the segmental friction factor first postulates an effective glass transition temperature ($T_{g,eff}$) of the chains that fill the local region near the segment. The Fox equation provides a simple relation to estimate $T_{g,eff}$ from φ_{eff}^{S}:

$$\frac{1}{T_g^{eff}} = \frac{\varphi_{eff}^{S}}{T_g^{PS}} + \frac{(1-\varphi_{eff}^{S})}{T_g^{PMMA}} \qquad (3.7)$$

Where φ_{eff}^{S} is the calculated effective styrene composition and T_g^{PS} and T_g^{PMMA} are the respective calorimetric glass transition temperature of polystyrene and PMMA. The Williams-Landell-Ferry (WLF) equation[132] is used to calculate the theoretical friction factor of the copolymer using its effective glass transition temperature

$$log\frac{\zeta(T)}{\zeta(T_g)} = \frac{-C_1(T-T_g^{eff})}{C_2+(T-T_g^{eff})} \qquad (3.8)$$

Where T is the temperature in Kelvin (T=423K), C_1 and C_2 are WLF parameters that are specific to each copolymer, and T_g^{eff} is the effective glass transition temperature calculated from Equation 3.7. $\zeta(T_g)$ and $\zeta(T)$ are the friction factors at the glass transition temperature and at the experimental temperature. We assume that the WLF parameters, as well as the friction factors at T_g, are a compositional average of those of the homopolymers as they are reported in literature.[89]

Table 3.3. Friction factor predicted from the L-M model and experimental determination of the effective styrene concentration around the copolymer

φ_A	$\zeta_{\text{L-M}}^{\text{Copoly}}$	$\zeta_{\text{exp}}^{\text{Copoly}}$	$\varphi_{\text{eff}}^{\text{Sty}}$
0.08	0.00530	0.00112	0.35
0.24	0.00293	0.00073	0.52
0.33	0.00221	0.00062	0.60
0.40	0.00181	0.00026	0.86

Equations 3.4 and 3.5 coupled with the Fox and WLF equations provide a connection between ζ and the effective local concentration, which allows a direct comparison between the L-M predictions and the experimental friction factor. These results are presented in Table 3.3. These results demonstrate that the L-M model predicts a copolymer friction factor that is significantly greater than the experimentally determined friction factor. Therefore, the friction factor predicted by the L-M model underestimates the local styrene concentration of each copolymer.

An explanation of these results calls to attention a principle assumption of the L-M model, that there is no energetic preference for A segments to be next to A segments or B segments to be next to B segments. Therefore, if thermodynamics play a role in the structure (and thus dynamics) of these blends, S and MMA segments will seek out similar monomers to minimize repulsion between the styrene and MMA. Thus the prediction of the L-M model increases styrene concentration from chain connectivity bias, however the athermal nature of the model does not account for the experimentally determined increase in the local styrene concentration, presumably a result from the minimization of unfavorable contacts. This is a strong indication that the thermodynamic interactions play a significant role in determining the dynamics of these blends.

Thus far, the discussion has primarily focused on analysis of the L-M model predictions. The focus will now turn to gaining a more complete understanding of the local concentration of the copolymers in the experimental system. The experimental friction factor provides an opportunity to gain insight into the importance of the experimental local composition around the copolymer on its observed rheological response. This requires analyzing the experimentally determined copolymer friction

factor using the WLF and Fox equations and Equation 3.6, to estimate the local styrene concentration of each copolymer chain. The progression through the WLF and Fox equations mirrors the previous analysis. First the effective glass transition temperature is determined for each copolymer using the WLF equation (Equation 3.8). Utilizing Equation 3.7 and the values of T_g^{eff} of each copolymer obtained from Equation 3.8, the effective local compositions, φ_{eff}^{S}, are calculated for each copolymer, where the results are presented in Table 3.3. These results show that the value of the effective styrene composition surrounding the copolymer chain for all four copolymers is higher than the local styrene composition of the copolymer predicted by the L-M model. This is consistent with simulation[88] and neutron reflectivity results[81], which demonstrates an enrichment of styrene around the copolymer chain relative to the global styrene composition.

The results presented here consistently demonstrate a significant impact of copolymer composition on its dynamics in miscible blends, which imply a significant alteration in its local environment. Moreover, the results clearly show that the thermodynamic interactions between polymer chains can significantly impact their dynamics. This suggests that theoretical models that seek to predict the dynamics of multi-component polymer systems develop a method to account for non-bonding interactions between components to improve correlation between theory and experiment.

3.4. Conclusion

A series of PS-*ran*-PMMA/PMMA blends were studied using rheology detailing the effect of copolymer composition on the dynamics of the copolymer in the miscible polymer blend. The zero-shear viscosity data are analyzed to obtain the effective

segmental friction factors of the copolymers, which indicate that the copolymer composition significantly impacts its dynamics. The friction factor of each copolymer increases with increasing MMA composition, reflecting the slower dynamics of PMMA. The measured friction factor of the copolymer, however, falls below what is expected from a compositional average, indicating a larger contribution from styrene than stoichiometry suggests. The Lodge-McLeish model predicts the local environment around the segment of the copolymer in the blend, which qualitatively agree with the experimental data, indicating an increase in styrene content due to the bias of chain connectivity. Calculation of the friction factor from the L-M prediction, however, demonstrates that the L-M model does not quantitatively match the experimentally determined copolymer dynamics. The L-M model predicts a copolymer friction factor that is up to an order of magnitude higher than the experimental friction factor. Further analysis of the rheology data utilizes the experimentally determined friction factor to estimate the local environment around the copolymer chain and is compared with the local environment predicted by the Lodge-McLeish model. This analysis further indicates an effective composition around a copolymer that is significantly richer in styrene than what the model predicts based solely on geometric and connectivity arguments.

One explanation of these results is that the thermodynamic interactions between styrene and methyl methacrylate monomers lead to an increase in styrene concentration in the vicinity of a copolymer chain. This explains the decrease in the monomeric friction factor of the copolymer due to thermodynamic interactions and is consistent with previous simulation and neutron reflectivity data.

Overall this study has consistently demonstrated the importance of the local concentration on copolymer dynamics. A test of the Lodge-McLeish theory demonstrates that, as the model is applied here, the underlying principles of the model do not allow quantitative predictions of the blend dynamics, as it does not capture thermodynamic interactions between components. The model is attractive in that it has had broad success and only requires two dimensionless parameters as inputs. This lends a degree of simplicity when considering extensions of the model. In an effort to fill in the gaps of this promising model, this investigation contributes insight that provide focus when considering modifications of the model.

Moreover, this study contributes to a more complete understanding of the importance of thermodynamics on the dynamics of multi-component blends, adding to a series of studies that have investigated the structure and dynamics of similar homopolymer/copolymer blends. The results of these studies consistently illuminate the local segmental environment as a key determinant of blend dynamics, specifically highlighting the role of thermodynamic interactions on the blend's local structure and dynamics. The experimental friction factor and comparison to the Lodge-McLeish model given here augment these studies, providing insight into the effects of non-bonding interactions on local concentration and its impact on homopolymer/copolymer dynamics.

CHAPTER 4:EFFECT OF MACROMOLECULAR ARCHITECTURE ON THE MORPHOLOGY OF POLYSTYRENE-POLYISOPRENE BLOCK COPOLYMERS

4.1 Introduction

In the previous two chapters, the impact of non-bonding interactions on the structure and properties of multi-component polymer systems were presented. Whereas these systems are compatible polymer blends, the current chapter explores the structure-property relationships of a multi-component polymer system that has significant repulsion between components. In this system, each component is bound to the other by a covalent bond to form a block copolymer, where the minimization of the unfavorable interactions requires the components to arrange into ordered nano-sized domains.[137] If the block copolymer consists of two chains end-bonded to form a linear diblock copolymer, this ordering, or microphase separation, is well understood as the result of extensive studies over the past three decades.[91] However, the structure-morphology relationships of nonlinear block copolymers are less well understood, primarily due to limitations on their synthesis. Therefore, this chapter will present a careful study that examines the role of connectivity on the phase behavior of a series of block copolymers, utilizing poly(styrene) (PS) and poly(isoprene) (PI) copolymers. A series of PS-PI block copolymer that vary in connectivity are presented, where the copolymer composition and molecular weight are held constant. The copolymer architectures studied include a linear diblock copolymer, and PS_2PI, $PSPI_2$, and PS_2PI_2 miktoarm stars. The morphologies of these block copolymers were characterized using transmission electron microscopy (TEM) and small-angle x-ray scattering (SAXS). The experimentally observed morphologies are also compared with those expected based on Milner theory and self-consistent field theory in order to achieve a greater understanding of the fundamental principles that correlate macromolecular architecture to block copolymer morphology.

4.2 Experimental and Simulation

4.2.1 Synthesis and Characterization

The four copolymers were synthesized by Dr. Paraskevi Driva using anionic polymerization and high vacuum techniques in all glass reactors with breakseal transfers and sampling via constrictions.[138] The linear PS-PI copolymer was synthesized via sequential addition of styrene and isoprene according to standard anionic procedures.[139] The synthesis of PS_2PI, $PSPI_2$, and PS_2PI_2 miktoarm stars was conducted as described in the literature.[102-105] A portion of each arm was isolated and characterized prior to linking using chlorosilane chemistry. Excess arms used to drive the linking reaction to completion were removed by solvent/nonsolvent fractionation (toluene/methanol). A Polymer Laboratories PL-50 size exclusion chromatography (SEC) system, equipped with a Precision Detectors two-angle light scattering detector, was used to measure absolute molecular weights and polydispersity indices (PDI) of the polymers. The SEC system was operated in tetrahydrofuran (THF) at a flow rate of 1 mL/min. Refractive index increment (dn/dc) measurements were completed in THF using a Wyatt Technology Optilab differential refractometer. Proton nuclear magnetic resonance (Bruker Avance 400MHz wide-bore spectrometer, samples in d-$CHCl_3$) experiments were completed to determine the composition of the final fractionated copolymers.

SEC chromatograms of the intermediate products during the synthesis of $PSPI_2$ are shown in Figure 4.1, and are typical and representative of those taken during the synthesis of all the block copolymers. The PS and PI arms were sampled and

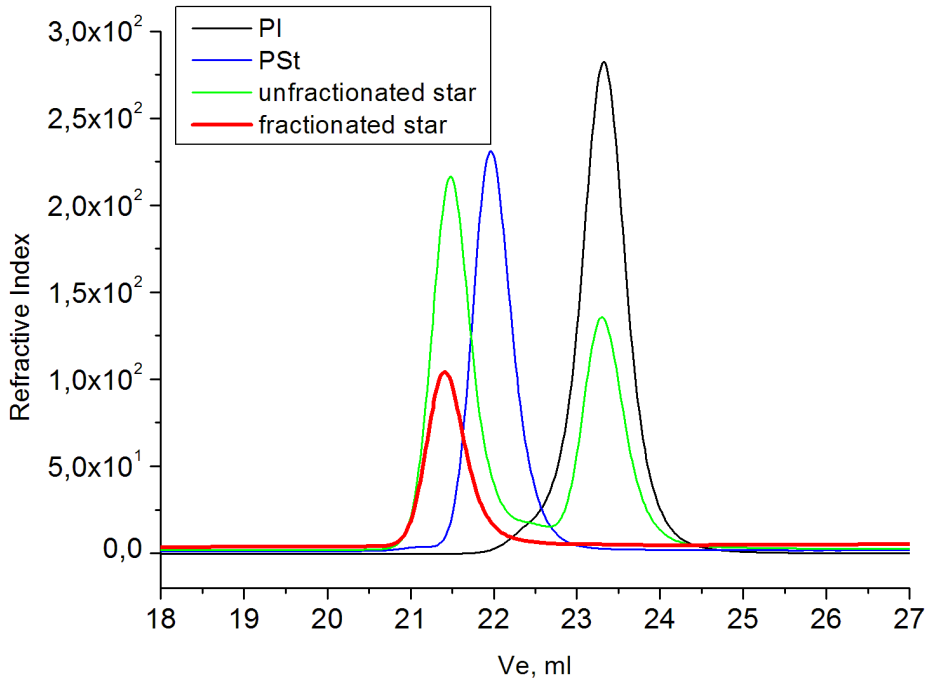

Figure 4.1. SEC chromatograms of the intermediate products in the synthesis of $PSPI_2$

Table 4.1. Volume fractions of the block copolymers as determined by nuclear magnetic resonance and light scattering using a measured and calculated differential index of refraction

Sample	v_{PS} NMR	v_{PS} LS with calculated dn/dc	v_{PS} from measured dn/dc
PS-PI	0.71	0.66	0.67
PS_2PI	0.65	0.67	0.68
$PSPI_2$	0.70	0.66	0.68
PS_2PI_2	0.67	0.65	-

independently characterized for absolute weight-average molecular weight (M_w) and polydispersitie determination prior to linking.

The living PS arm was reacted with a ~100:1 excess of methyltrichlorosilane to create dichlorosilyl-terminated PS, where excess methyltrichlorosilane was removed from the reactor by prolonged pumping on the vacuum line, and then reacted with excess living PI to create the miktoarm star. Excess PI was removed by fractionation, and the final product exhibits a narrow and symmetrical peak in SEC. The molecular characteristics of the precursor linear polymers and the final copolymers are provided in Table 4.1. Absolute M_w values were determined by SEC with light scattering detection, while the PDI values were determined based upon the SEC refractive index detector response. The weight percent of PS in the block copolymer as determined by NMR, by light scattering (from M_w of the arms and the final block copolymers), and by refractive index increments (in THF) are listed in Table 4.1. Table 4.2 lists the experimentally determined PS *volume* fractions of the four block copolymers based on the three different techniques: NMR spectroscopy, absolute molecular weight determinations, and dn/dc measurements.[99] Clearly, all four block copolymers are quite similar in composition. Good agreement, within a few %, is observed for the measured compositions of a given sample by the different techniques.

4.2.2 Annealing

The ability of a copolymer to microphase separate into ordered domains first requires the chains to be mobile and second requires time for the chains to order into the most energetically favorable conformation. To ensure an equilibrium morphology, a rigorous

annealing process was employed.[112] Solid films approximately 2 mm thick were cast from tetrahydrofuran solutions of 5 wt% polymer in 30 mL beakers allowing chain mobility within a solution as the solvent slowly evaporates over time. The evaporation of the solvent was controlled via small holes in aluminum foil covering the beaker and a larger beaker covering the 30mL beaker in a fume hood, forming a solid film within 10-14 days. These films were then held for two days at room temperature and atmospheric pressure and then placed under vacuum to remove residual solvent. Raising the temperature above the Tg of PS and PI gives chain mobility within the melt, thus the vacuum oven temperature was ramped to 120 °C over the period of 3 days and kept there for 1 week. After annealing, the temperature was slowly ramped down to 80 °C over 2 days and then quickly lowered to room temperature. This casting and annealing procedure was designed to promote the development of equilibrium strongly segregated morphologies.[112]

4.2.3. Transmission Electron Microscopy

Block copolymer morphology can be directly investigated by transmission electron microscopy (TEM). This technique uses a focused beam of electrons to image a specimen, allowing significantly better resolution due to the small de Broglie wavelength of electrons. An emission source (such as a tungsten filament) at the top of the microscope is connected to a voltage source, giving sufficient current to emit the electrons into a vacuum column. A series of electromagnetic lenses then manipulate the electron beam, focusing the beam onto the sample where the electrons are transmitted if the sample is sufficiently thin.

Table 4.2 Molecular weight characteristics of precursor homopolymers and final PS-PI block copolymers. a) via SEC-LS; b) via SEC-DRI

Sample	M_w PS[a] arm Kg/mol	M_w PI[a] arm Kg/mol	M_W final[a] Kg/mol	PDI final[b] (M_w/M_n)	%w/w_{PS} (NMR)	%w/w_{PS} (LS)	dn/dc_{exp}	dn/dc_{calc}
PS-PI	70.9	-	104.1	1.06	71	68	0.1691	0.168
PS_2PI	32.1	27.5	90.3	1.06	69	70	0.1697	0.169
$PSPI_2$	73.4	16.2	104.4	1.05	73	70	0.1696	0.169
PS_2PI_2	36.4	17.4	105.9	1.07	70	68	-	0.168

Depending on the density of the material present, some of the electrons are scattered. At the bottom of the microscope the unscattered electrons hit a fluorescent screen, giving rise to a "shadow image" of the specimen with its different parts displayed in varied darkness according to their electron density. The image is viewed directly by the operator and then the "shadow" is imaged with a camera.

A TEM image requires that some of the electrons that contact the sample be scattered and some to pass right through, which requires an electron density difference between the components being imaged. Preferentially staining one component in a multi-component polymer system with a heavy metal allows the density of one component to be sharply contrasted with the density of the other. Exposure of the PS/PI copolymers to the vapor of a 4% osmium tetroxide solution for 30 minutes stains the PI portion of the copolymer. The OsO_4 preferentially reacts with the double bond of the poly(isoprene), creating a larger electron density in the PI phase, which scatters the electron beam. This results in dark PI domains and light poly(styrene).

The TEM samples were prepared by lowering the temperature of the sample to -90 °C and microtomed, collecting thin sections, using a Boeckeler PowerTomeX UltraMicrotome. The slices (<100 nm thick) were collected on a copper grid and stained as described above. The morphologies were determined using a Hitachi H800 (TEM) at a voltage of 75KeV.

4.2.4. Small-Angle X-Ray Scattering

Small angle X-ray scattering (SAXS) is an analytical technique that is capable of delivering structural information of macromolecules in the nanometer range. In SAXS experiments, the sample is irradiated by a well-defined, monochromatic X-ray beam. When a non-homogeneous medium is irradiated, structural information of the scattering particles can be derived from the angular dependence of the intensity of the scattered beam. Scattering occurs due to the interaction of the x-ray beam with the electron clouds. The shape and intensity of the scattering intensity as a function of scattering angle is dependent on the specific density distribution of the electrons in the scattering sample. This technique is fast and straightforward and does not require any special sample preparation. It can be utilized to analyze most samples under ambient conditions without any chemical or mechanical pre-treatment. Bragg's law states that the scattering from an ordered crystal is given by:

$$n\lambda=2d\sin\theta \qquad (4.1)$$

Where d is the distance between the atomic layers in a crystal, λ is the wavelength of the incident radiation, θ is half of the scattering angle measured from the incident beam and n is an integer. According to Bragg's law, the structural size is inversely proportional to the scattering angle, thus high angle relates to smaller structure and low angle relates to larger structures.[121]

For the block copolymers used in this study, SAXS is used to determine the morphology of each sample and the domain spacing. The domain spacing is determined by plotting scattering intensity as a function of q (scattering vector), where

$$q=4\pi/\lambda\sin(\theta) \qquad (4.2)$$

Combining equations 4.1 and 4.2, the relationship between the q-position of a peak in the scattering curve and d-spacing of the microphase separated domains is:

$$q=2\pi/d \qquad (4.3)$$

The spacing of the PS and PI domains can thus be determined from a SAXS pattern using Equation 4.3. The ordering of the microphase separated domains exhibit characteristic peaks in the SAXS scattering pattern, where the positions of the peaks are correlated to specific morphologies. More precisely, the experimentally determined ratio of the q values of the secondary Bragg peaks (q_i) to the q of the primary peak (q^*) q_i/q^* can be compared to those that are predicted for a given morphology. In this manner, the SAXS pattern is used to monitor the morphologies of the samples examined in this study.

The SAXS pattern for the samples was recorded on a Molecular Metrology small angle x-ray instrument equipped with a two-dimensional position sensitive proportional detector of circular shape (radius = 2.5 cm), using Cu Kα radiation (λ=1.5418 A). A monochromatic x-ray source from the x-ray sealed tube is focused by a pair of Kirkpatrick-Baez microfocusing mirrors. The sample to detector distance was 1.5 m with the scattering vector (q) range of 0.01 A^{-1} to 0.15 A^{-1}.

4.2.5 Self-Consistent Field Theory

To augment the experimental work seen in this manuscript, Dr. Scott Sides has carried out Numerical self-consistent field theory (SCFT) simulations. SCFT for dense polymer melts has been highly successful in describing complex morphologies in block copolymers.[140] Field-theoretic simulations such as these are able to access large length and time scales that are difficult or impossible for particle-based simulations such as

molecular dynamics, while still incorporating more realistic polymer models than many macroscopic, continuum simulations. The model and simulation method will be briefly described for a dense melt of AB copolymers in bulk. For the experimental system in this paper, the A species represents monomers of PS and the B species represent monomers of PI. The chemical specificity of PS and PI is captured in the model through the value of the Flory parameter χ, which controls the strength of the chain segregation that drives the formation of nanoscale morphologies. The Hamiltonian of a dense melt gives the free energy of the ordered states within the melt. The lowest free energy gives the most likely conformation of the copolymers where, typically, the most well-ordered structure has the lowest free energy.

A "spectral filtering"[141] algorithm has been shown to help reduce the presence of topological defects in numerical SCFT calculations of block copolymer structures by removing certain frequency components of the chemical potential fields during their relaxation towards the lowest free-energy configuration. The spectral filtering essentially keeps the largest components of the frequency spectrum of the transformed chemical potential field, which then acts as an effective estimate for the self-consistent algorithm. Of course, this assumes that the topological defects one is trying to remove will tend to have the smallest frequency components.

In order to compare the SCFT results to experimental data, the PS-PI interaction energy and length scales must be matched to the SCFT simulation parameters. The length scale enters the theory through the unperturbed radius of gyration:

$$R_{g0}^2 = \frac{b^2 N}{6} \qquad (4.4)$$

where N is the chain length (number of independent chain segments) and b is the statistical segment length. The energy scale enters through the temperature dependent Flory parameter $\chi(T)$. The temperature dependent Flory-Huggins parameter for polyisoprene and polystyrene has been reported as[142]

$$\chi_{IS}(T) = \frac{26.4}{T[°C] + 273.15} - 0.0287 \qquad (4.5)$$

based on a common segment volume of 118 A^3. Using the annealing temperature of 120 °C gives an interaction parameter of $\chi = 0.0385$. To estimate the number of segments in the copolymer chains, the following homopolymer densities are used (at 140 °C)[143] ρ_I = 0.830 g/cm^3 ρ_S = 0.969 g/cm^3 with an average molecular weight of M_n = 100,000 Da. Using these parameters gives a segregation strength of $\chi N = 54.0$, which indicates strong segregation. Very large segregation strengths can introduce numerical instabilities in the SCFT calculations, so to improve the stability in the simulations, a lower value of χN = 30.0 is used. However, the well-known phase diagram for linear diblocks suggests that phase morphologies change little once the chains are strongly segregated. The SCFT simulations also account for the different Kuhn segment lengths for PS and PI, where b_{PS} = 5.47 Å and b_{PI} = 6.07 Å are used in the simulation.

To augment the SCFT results, Dr. Bobby Sumpter has performed a full-scale molecular dynamics (MD) simulation of a diblock PS-*b*-PI copolymer using LAMMPS MD simulation package.[144] The MD simulation are carried out at melt density, $\rho^* = 0.85$ for a system of 200 chains of chain length 100. Each chain consists of 70 PS and 30 PI monomers.

4.3 Results and Discussion

The morphologies of the copolymers are characterized by TEM and SAXS, where the SAXS data for the samples are displayed as the circularly averaged, one-dimensional plots of intensity (I) in absolute units (cm^{-1}) as a function of q. Each of the SAXS patterns includes points that denote the expected position of higher order peaks of the preliminarily assigned morphology. The position of the primary peak, q*, for the PS-*b*-PI, PS_2PI, and PS_2PI_2 are 0.0115, 0.0146, and 0.0142 $Å^{-1}$ respectively, corresponding to d-spacings of 54, 43, and 44 nm, respectively. Obtaining a SAXS pattern of the PS-PI_2 sample is currently underway (and will be published in a future article), though TEM of the PS-PI_2 unequivocally establishes the morphology of this sample, as will be discussed below.

A TEM image of the linear PS-*b*-PI sample is presented in Figure 4.2. A brief inspection of this figure may lead to an initial assignment of a lamellar morphology. However upon closer inspection, the poly(isoprene) domains (dark lines) appear to be narrower than the polystyrene domains (lighter lines), which is consistent with the projection of hexagonally packed cylinders that are cut along the tube axis, but not lamellae. SAXS data provides additional insight, as shown in Figure 4.3, where the ratio of the peak positions of higher order peaks to that of the primary peak are denoted. The SAXS data clearly indicates that this diblock copolymer exhibits a hexagonally-packed cylinder morphology. This result is in accord with the expected morphology for a PS-PI

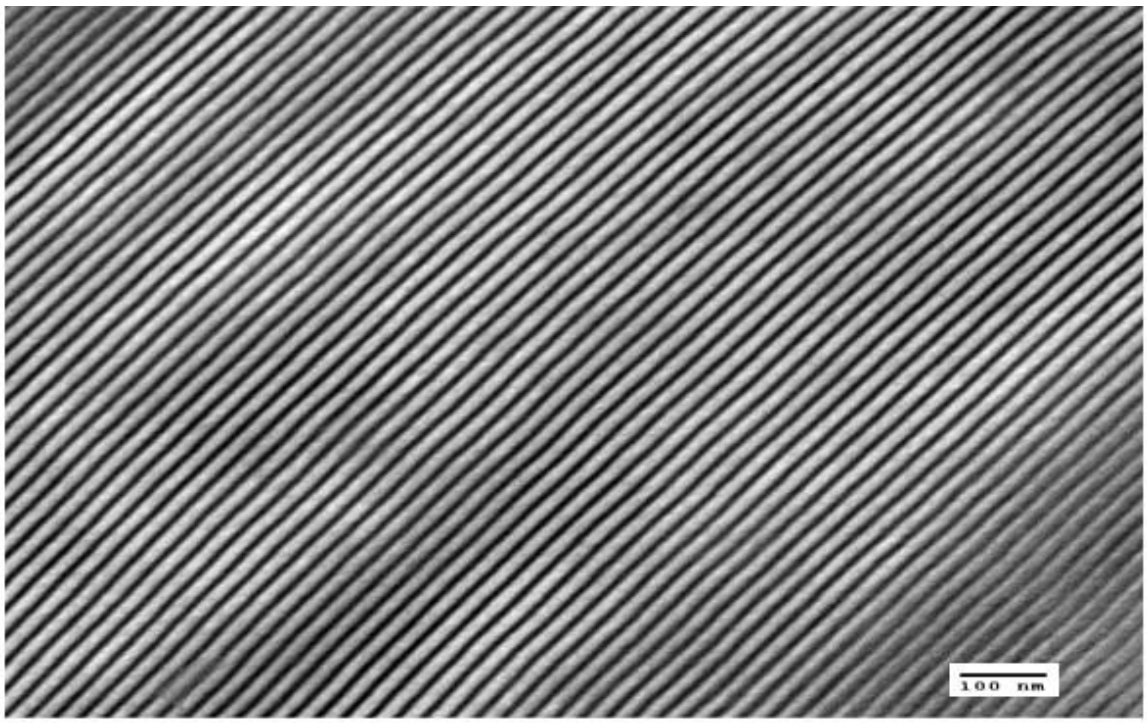

Figure 4.2. TEM of the linear PS-b-PI diblock copolymer, exhibiting features that are consistent with cylindrical morphology

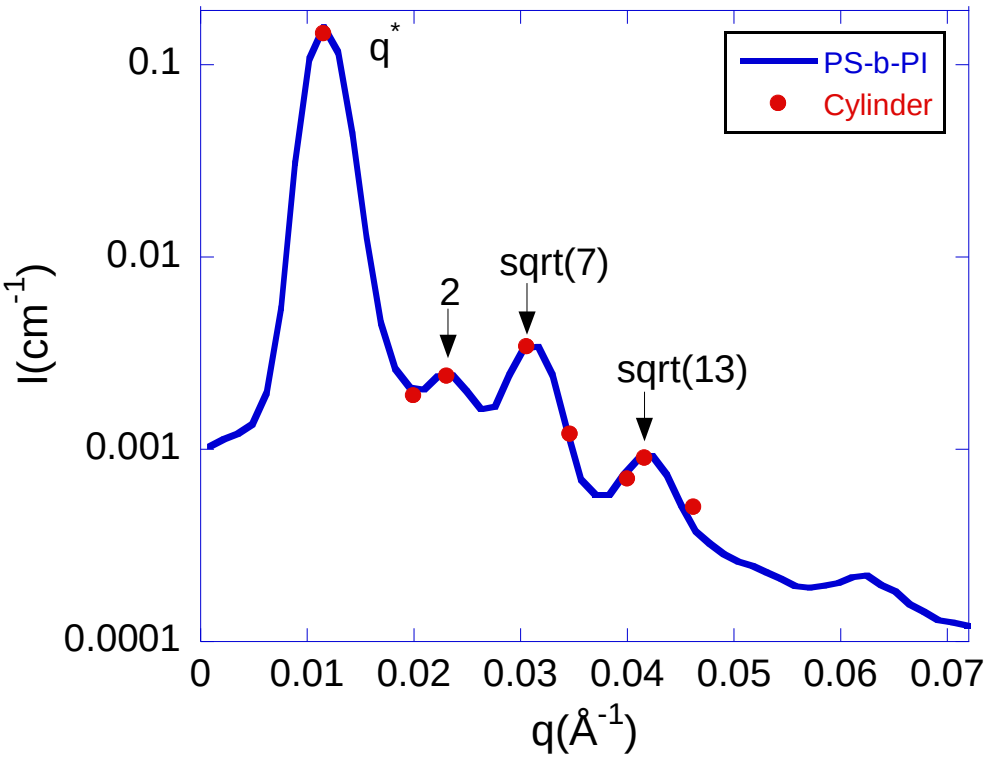

Figure 4.3. SAXS curve of the linear PS-*b*-PI copolymer plotted with peaks that are expected for the cylindrical morphology as red circles.

diblock copolymer of 0.68 volume fraction PS – the composition that represents the average of the three values reported in Table 4.2.[91] The numerical SCFT results for the PS-PI diblock (Figure 4.4.) also clearly show hexagonally packed cylinders for 0.70/0.30 PS/PI linear diblock copolymer, while LAMMPS molecular dynamics simulation data show (Figure 4.5) the presence of similar morphologies for 0.70/0.30 PS-*b*-PI linear block copolymers. Therefore, all experimental and computational studies clearly demonstrate that the PS-PI linear diblock synthesized for this study forms the expected cylindrical morphology.

The structure of the PS_2PI_2 miktoarm copolymer can be thought of as two linear diblock copolymers that are joined at their junction points, but are half the length of the original diblock. Based on this picture and its architectural symmetry, the morphology of this copolymer should mimic that of the PS-*b*-PI linear diblock. The TEM images of this sample, examples of which are shown in Figures 4.6 and 4.7, exhibit structures that are consistent with a cylindrical morphology.

As mentioned above, the 4-arm star can be envisioned as approximating a linear diblock copolymer that is half the length, as each arm of the PS block and PI block of the PS_2PI_2 is one half the length of the PS-PI copolymer. If this decrease in molecular weight were the only factor governing the phase domain structure, the domain size of the PS_2PI_2 should be 63% ($D \sim N^{2/3}$) of the PS-PI diblock. Analysis of the SAXS data (Figure 4.8) however, indicates that the PS_2PI_2 domain size is 10 nm (44 nm vs. 54 nm) smaller than that of the PS-*b*-PI domain size, a decrease of 18%.

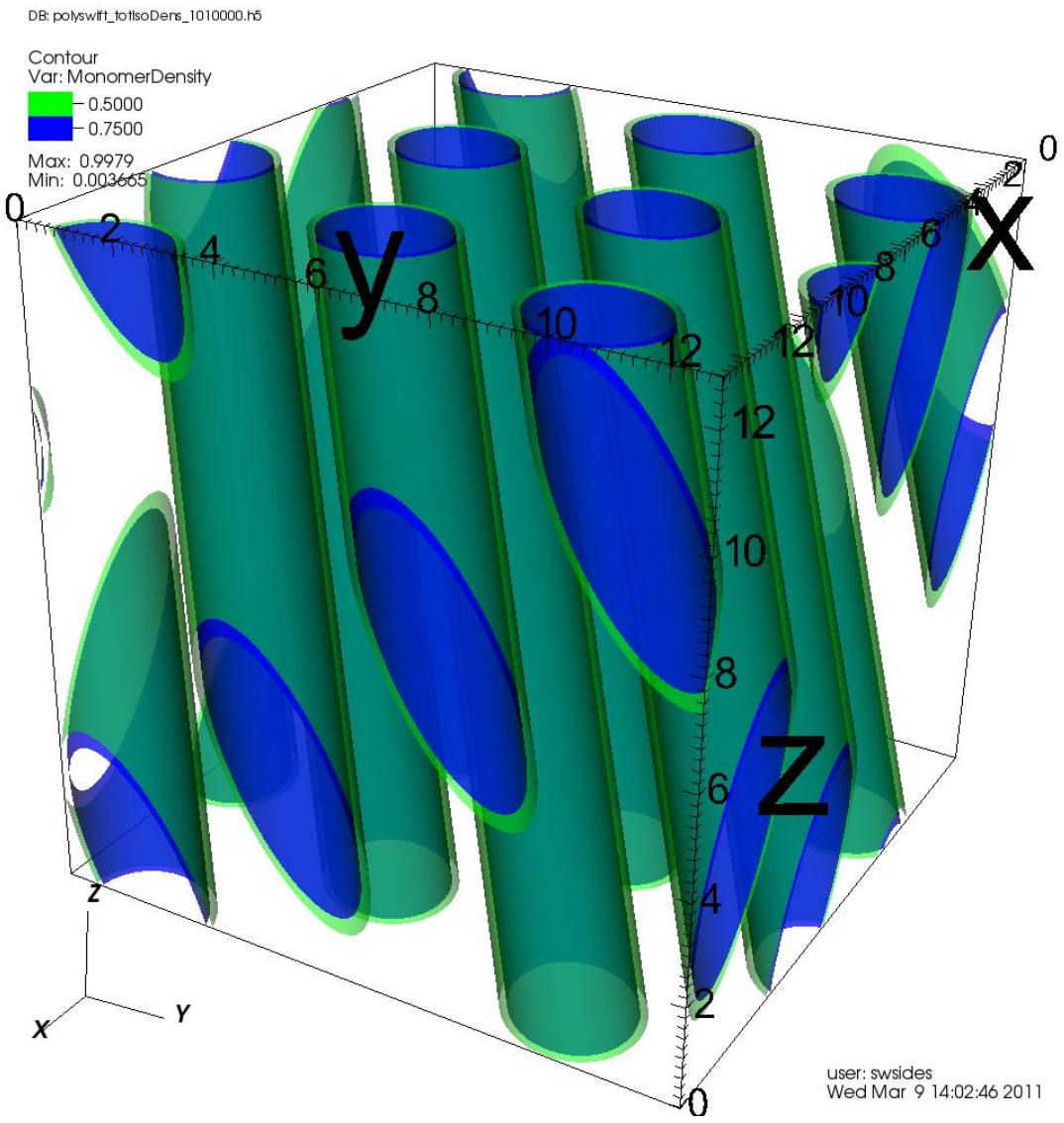

Figure 4.4 Density contours from numerical SCFT simulation of PS-PI diblock in bulk (PS volume fraction = 0.70 PI volume fraction = 0.30). Spectral filtering is turned on, which results in the lowest free-energy among all runs performed on this sample.

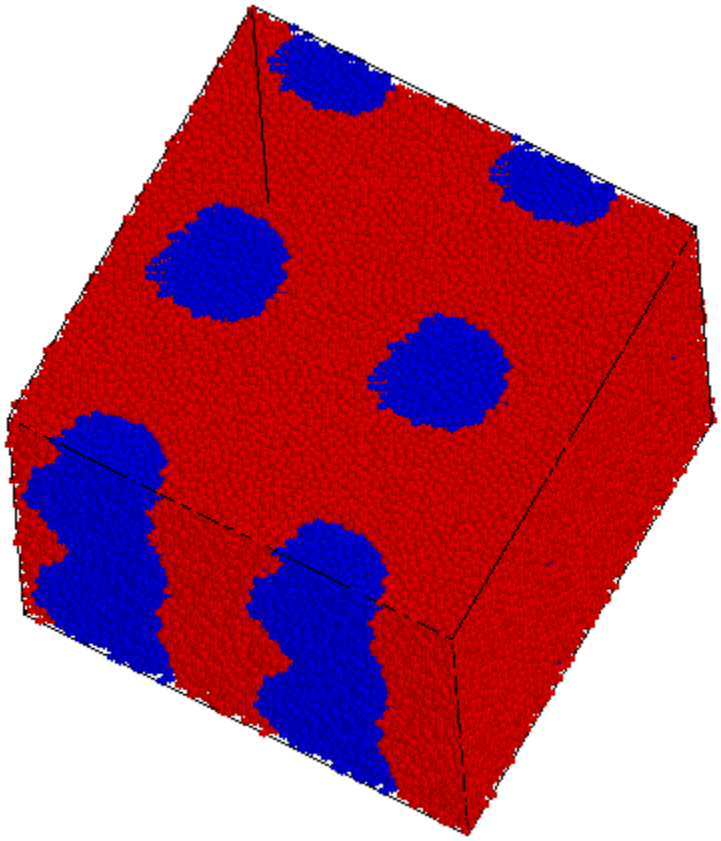

Figure 4.5. Full scale MD simulation of 70-30 PS-b-PI diblock showing the similar morphology as obtained by SCFT. LAMMPS molecular dynamics package has been used to generate this morphology. The red dots are 0.7 PS block and the blue dots are 0.3 PI block. The PI block forms the cylinders and the PS block forms the bulk.

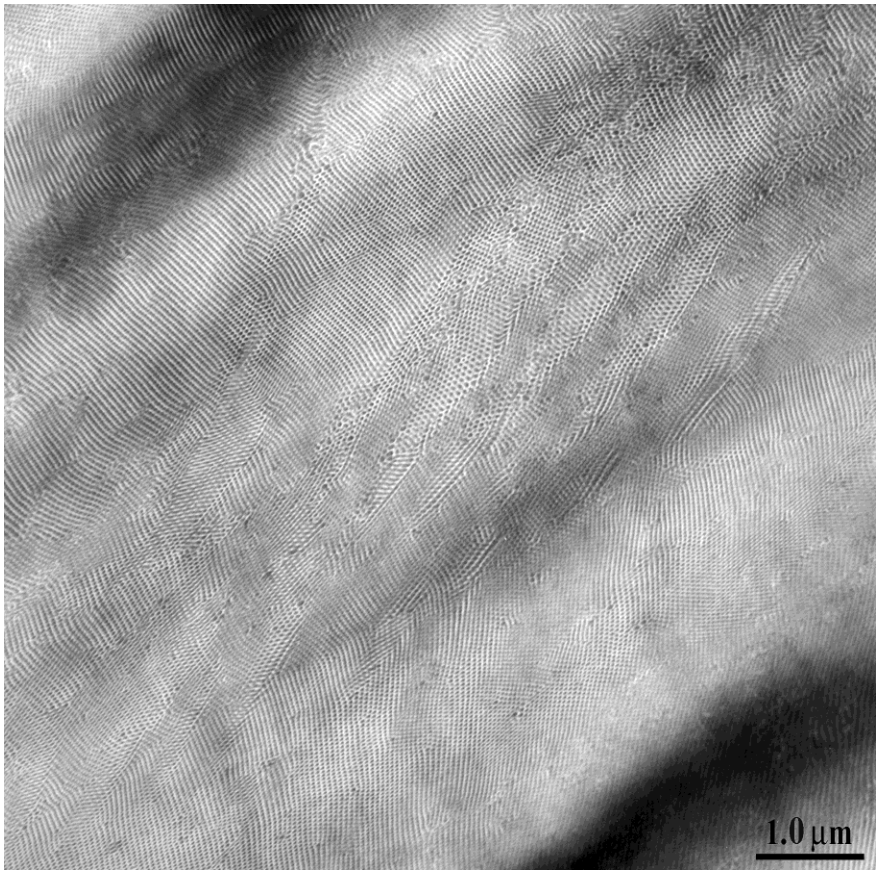

Figure 4.6. TEM images of the PS_2PI_2 miktoarm star, exhibiting features that are consistent with a cylindrical morphology.

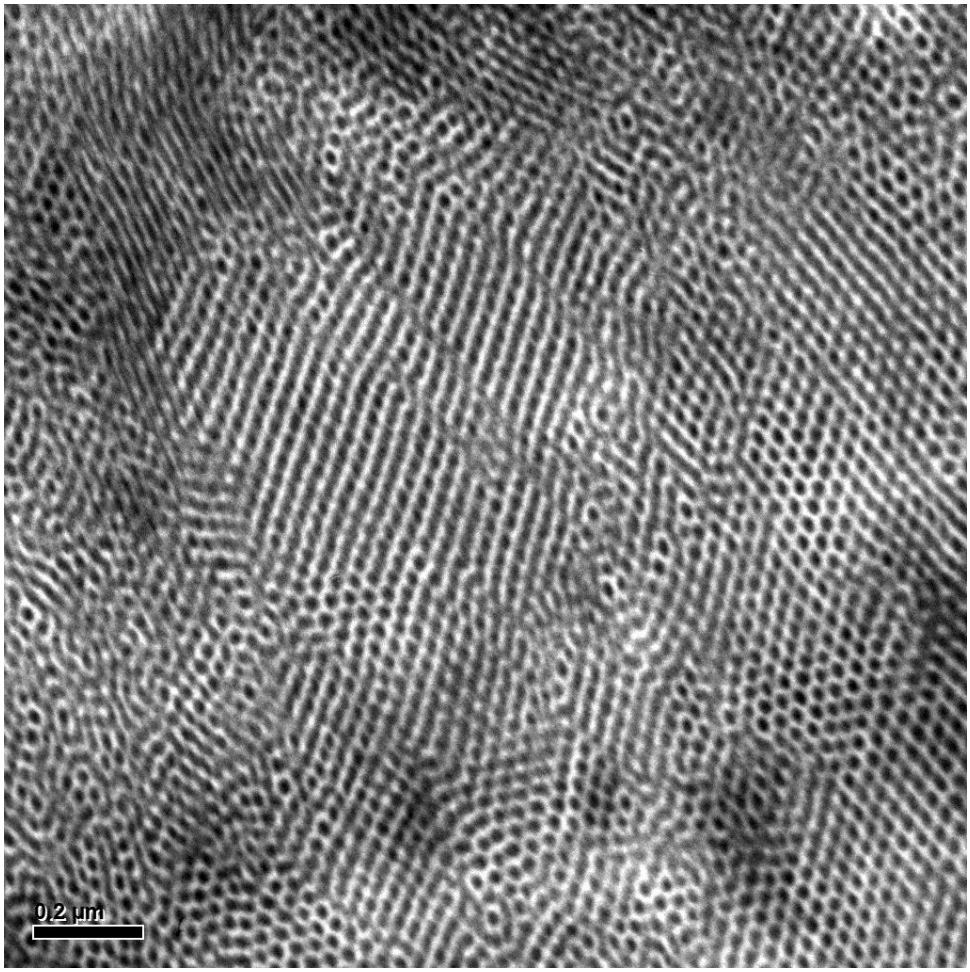

Figure 4.7. TEM images of the PS_2PI_2 miktoarm star, exhibiting features that are consistent with a cylindrical morphology.

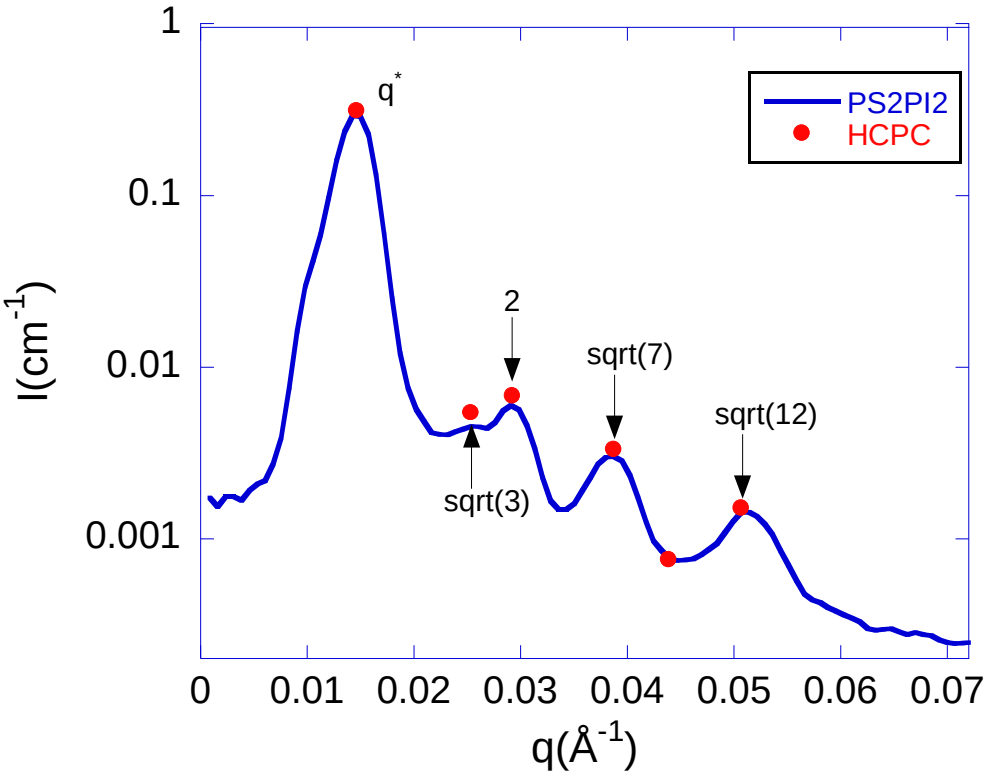

Figure 4.8. Small angle x-ray curve of the PS_2PI_2 miktoarm star plotted with peaks expected for cylindrical morphology

The domain spacing of the SCFT simulation is in good agreement with experiment for the PS-*b*-PI (~ 46nm) though underestimates the domain spacing in the PS_2PI_2 (~23nm). Possible reasons for this discrepancy include inadequate accounting for chain stretching at the junction point in the assumption of a Gaussian coil that is inherent in the SCFT calculation or uncertainty in the estimation of the χN used in the SCFT calculation, both of which may result in a more compact coil than is observed experimentally.

Clearly, the experimentally determined domain spacing of the 4-arm miktoarm star copolymer indicates that the connectivity of the blocks dramatically impacts the stretching of the blocks. In the 4-arm star, there exist two chains packed in each domain near one junction point. The result of excluded volume in this region is that each arm must extend away from the junction point more rapidly than in a linear diblock, resulting in chain stretching. This chain stretching near the junction point dominates the chain conformation, resulting in a domain size for the PS_2PI_2 miktoarm star that is significantly larger than 63% of the linear PS-*b*-PI domain size.

An understanding of the role of asymmetric chain connectivity on the copolymer morphology can be gleaned by comparing these two cylindrical morphologies to those of the PS_2PI and $PSPI_2$ branched block copolymers. Multiple TEM images of the PS_2PI sample exhibit the morphological characteristics of body centered cubic (BCC) spheres. An exemplary image of the PS_2PI sample is shown in Figure 4.9, where the PI chains (dark phase) form the spheres in this sample, and the matrix is composed of the PS component. The SAXS results of the PS_2PI sample (Figure 4.10), exhibit peaks that also match those that are expected from a spherical morphology. Thus, placing the junction

point between components in the middle of the PS block, rather than the end, results in the formation of a morphology with higher curvature, spheres. The high curvature of this morphology is a result of the requirement that two PS arms be connected to the junction point and pack into the domain. This packing of relatively rigid PS arms requires significant surface area, which in turn results in the highly curved spherical morphology.

Electron microscopy clearly shows that the PS-PI_2 copolymer exhibits a gyroid (bicontinuous) morphology, as shown in Figure 4.11. Thus, placing the junction point in the middle of the (more flexible) PI block results in a morphology with lower curvature (gyroid vs. cylinder). This again is driven by the packing requirement of the two PI arms, which must be connected at the junction point. In this case, the shorter, more flexible PI arms require less surface area than the longer PI arm of the linear diblock, which results in the lower curvature morphology.

4.3.1Comparison between Experimental and Computational Results

Comparison of the computational and experimental results provides additional insight into the fundamental driving forces that control the observed morphology of these architecturally dissimilar diblocks. The simulations are in qualitative agreement with the experimental results for the PS_2-PI and PS-PI_2 samples, but are not as conclusive as the more precise correlation that exists between computation and experiment for the PS_2-PI_2 and linear PS-PI samples. Figure 4.4 shows the density contours for the PS-*b*-PI linear diblock system from numerical SCFT simulations for v_{PS}=70%. Experimental results show that this sample forms hexagonal cylinders, as expected from numerous theoretical treatments and other SCFT calculations. Figure 4.12 shows the density contours for the PS_2-PI_2 sample from numerical SCFT simulations for v_{PS}=70%, where the experimental

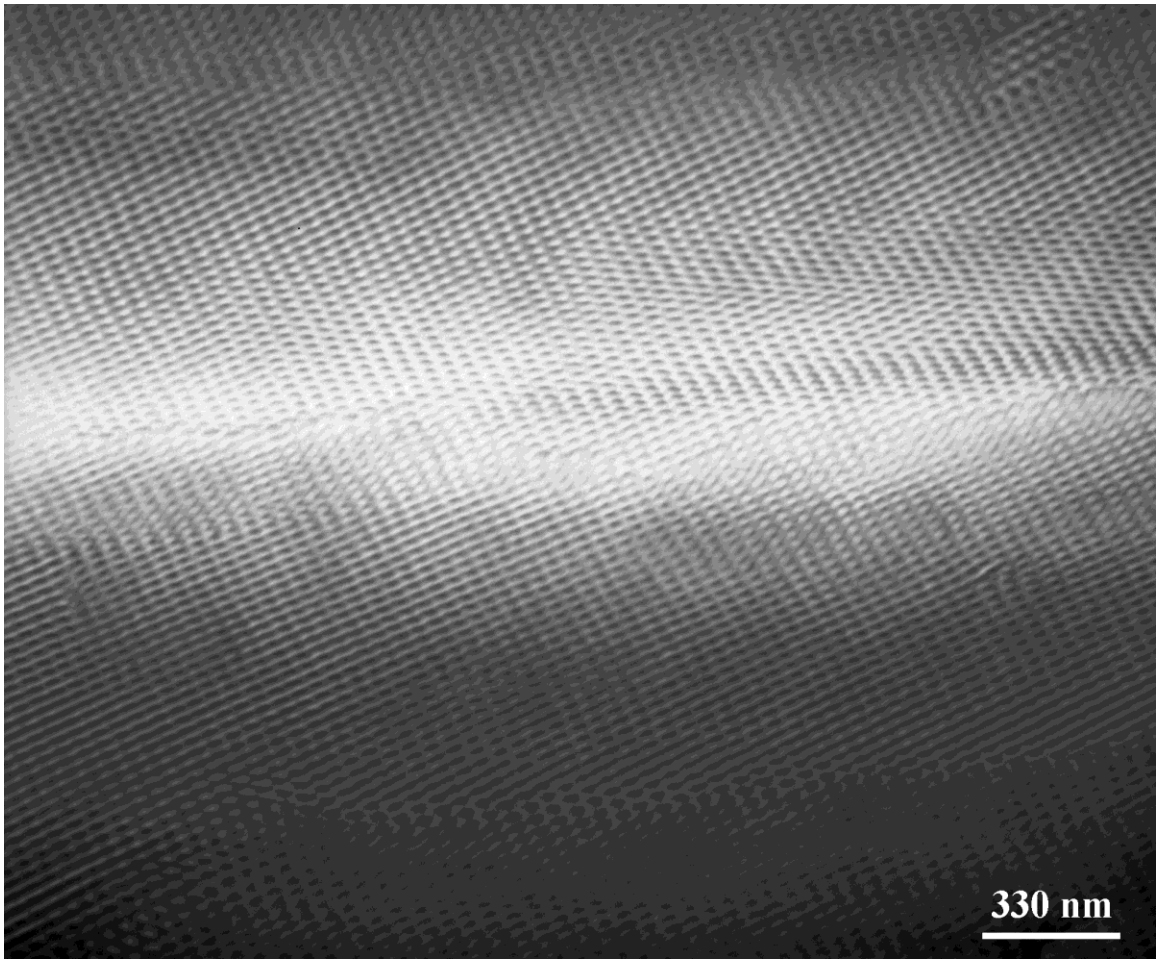

Figure 4.9. A representative TEM image of the PS_2PI miktoarm star copolymer exhibiting features that are consistent with spherical morphology.

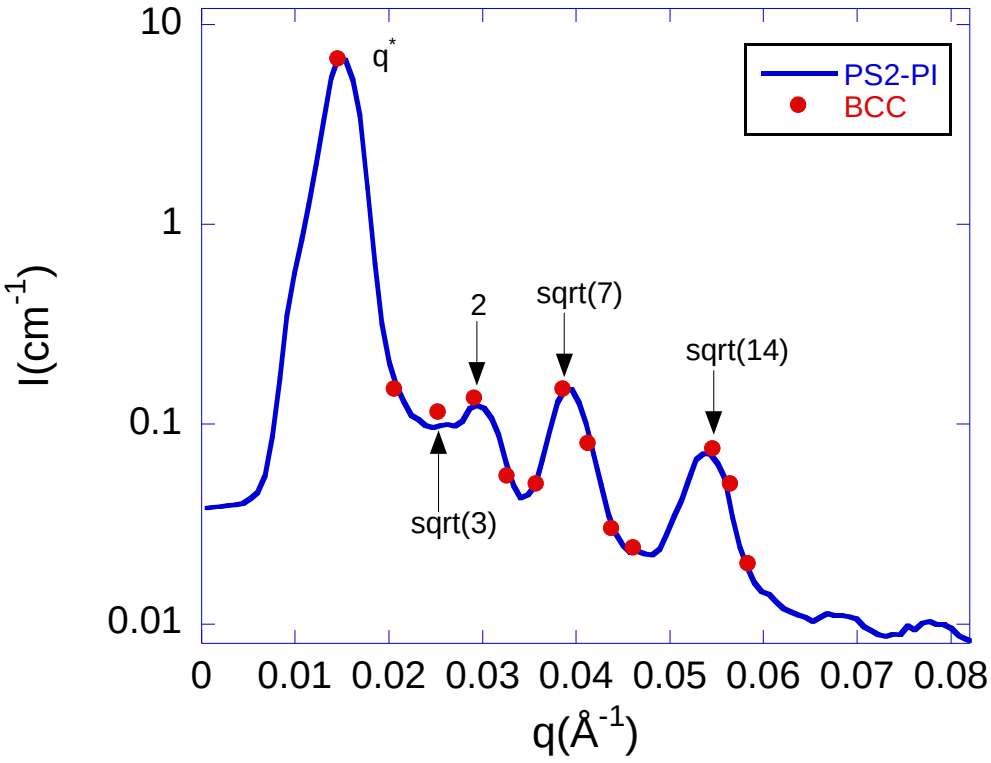

Figure 4.10. A SAXS curve of the PS_2PI miktoarm star copolymer plotted with peaks expected for BCC spheres.

results also exhibit hexagonal cylinders, in good agreement with the simulations. In addition, the domain size of the cylinders in PS_2PI_2 decreases relative to those in the PS-PI linear diblocks, also in qualitative agreement with experiment. Additional SCFT simulations on the PS_2-PI_2 sample were completed, where the segregation strength and PS volume fraction were varied. These calculations also show the formation of hexagonal cylinder morphologies, indicating this PS_2-PI_2 system is well within the hexagonal cylinder region of the phase diagram.

Figure 4.13 shows the density contours for the PS-PI_2 system from numerical SCFT simulations for v_{PS}=74% with spectral filtering turned off. NMR results show that v_{PS} is higher in this sample than the other branched structures; therefore the SCFT simulations for this sample were performed for a v_{PS} of 74%. These results are consistent with a bicontinuous gyroid morphology with defects, which agrees with the TEM and SAXS results. Figure 4.14 shows density contours for the PS_2-PI system from numerical SCFT for v_{PS}=70% and with spectral filtering turned on. The well-ordered BCC phase shown in Figure 4.14 does not have the lowest free energy for the simulations runs, however, the free energy is extremely close to that of the lowest free energy value.

Thus, these results indicate that the incorporation of branched junctions in block copolymers alters the packing of the blocks and shifts the phase boundaries in the resultant block copolymer. The results presented here offer insight into the detailed role this change in architecture has on the packing of the blocks, and therefore polymer chains into microphase separated structures. The linear diblock copolymer in this study forms a cylindrical morphology, while the branched copolymers form cylindrical (PS_2PI_2), spherical (PS_2PI), and gyroid ($PSPI_2$), morphologies. The alteration in morphology with

block connectivity is interpreted to be the result of the packing of the additional blocks in the major and minor phase, all of which are confined to a junction point. This local packing constraint leads to an increase in curvature with the packing of the additional blocks in the major phase at the junction or a decrease in curvature with the packing of the chains in the minor phase.

Table 4.3 shows a summary of the results of this study. This table shows general agreement between our experimental results, SCFT computational studies, and previously reported theoretical work.[107,113] To compare to previous theoretical work, the architectural asymmetry parameter, $\varepsilon=(n_A/n_B)(l_A/l_B)^{1/2}$, is calculated. In this calculation, n_i represents the number of arms of type *i*, and $l_i=v_i/b_i^2$, where v_i and b_i are the segmental volume and the statistical segment length of component *i* ; v_{PS} = 176 Å^3, v_{PI} = 132 Å^3, b_{PS} = 6.9 Å, b_{PI} = 6.8 Å.[143] One discrepancy lies in the PS-PI_2 results, where a co-continuous morphology is observed experimentally and corroborated by SCFT calculations, however the Milner theory predicts a lamellar morphology. It should be pointed out, however, that the theory qualitatively agrees with the experimental findings in that it predicts a morphology with decreased curvature, consistent with the result reported here. One explanation for this discrepancy lies in the estimation of conformational flexibility predicted by the Milner theory. An underestimation of the conformational flexibility leads to a prediction of a lower curvature morphology (lamellar). The conformational flexibility used in the Milner theory (via the segmental volume and the statistical segment length) estimates that the PI chains will adopt a stretched conformation, effectively predicting that the enthalpic penalty incurred to increase the interfacial area (lamellar) between blocks is less than the entropic penalty of a stretched conformation that is

needed to produce a form a morphology with decreased interfacial area, but more curvature (gyroid). In this way, the theory underestimates the ability of the PI chains to stretch out to decrease the interfacial area, and predicts the higher interfacial area (lamellar) morphology. However, gyroid is experimentally observed indicating that the two PI chains are able to accommodate an entropic penalty by stretching out in order to minimize excluded volume interactions. This entropic penalty appears to be favored over a greater enthalpic penalty that would result from the formation of the lower curvature lamellar morphology.

4.4. Conclusions

The structure-property relationships of four block copolymers were investigated documenting the effect of block connectivity on the microphase separated morphology of the copolymers. Experimental and computational results that document the morphologies of the block copolymers consisting of styrene and isoprene are reported, where generally good agreement is found. The reported results indicate that the excluded volume of packing multiple blocks into a domain at a junction point dominates the formation of the resultant morphologies. For instance, introducing a branch point in the majority (PS) block (i.e., the PS_2-PI copolymer) leads to the formation of a spherical morphology, whereas the linear PS-PI diblock copolymer exhibits a cylindrical morphology. The formation of this higher curvature morphology is the result of packing two PS chains into the matrix at a single junction point. Similarly, the introduction of a branch point in the flexible minor phase (PS-PI_2) leads to the formation of the gyroid morphology, which is the consequence of packing two PI chains into the minor phase, which forms a lower

curvature morphology. Therefore, the formation of the new morphology is governed by the minimization of chain crowding at the junction point. The morphology of the four

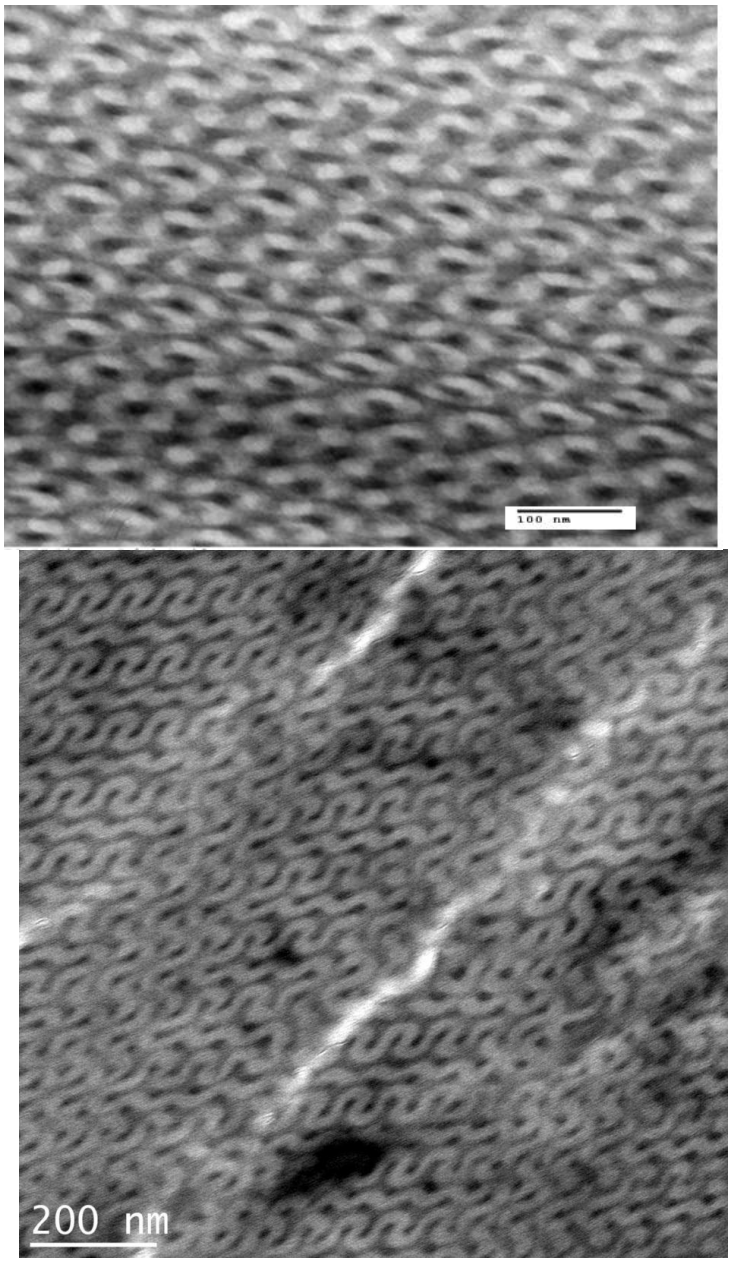

Figure 4.11. A TEM image of the $PSPI_2$ miktoarm star copolymer exhibiting the characteristic patterns of the gyroid morphology.

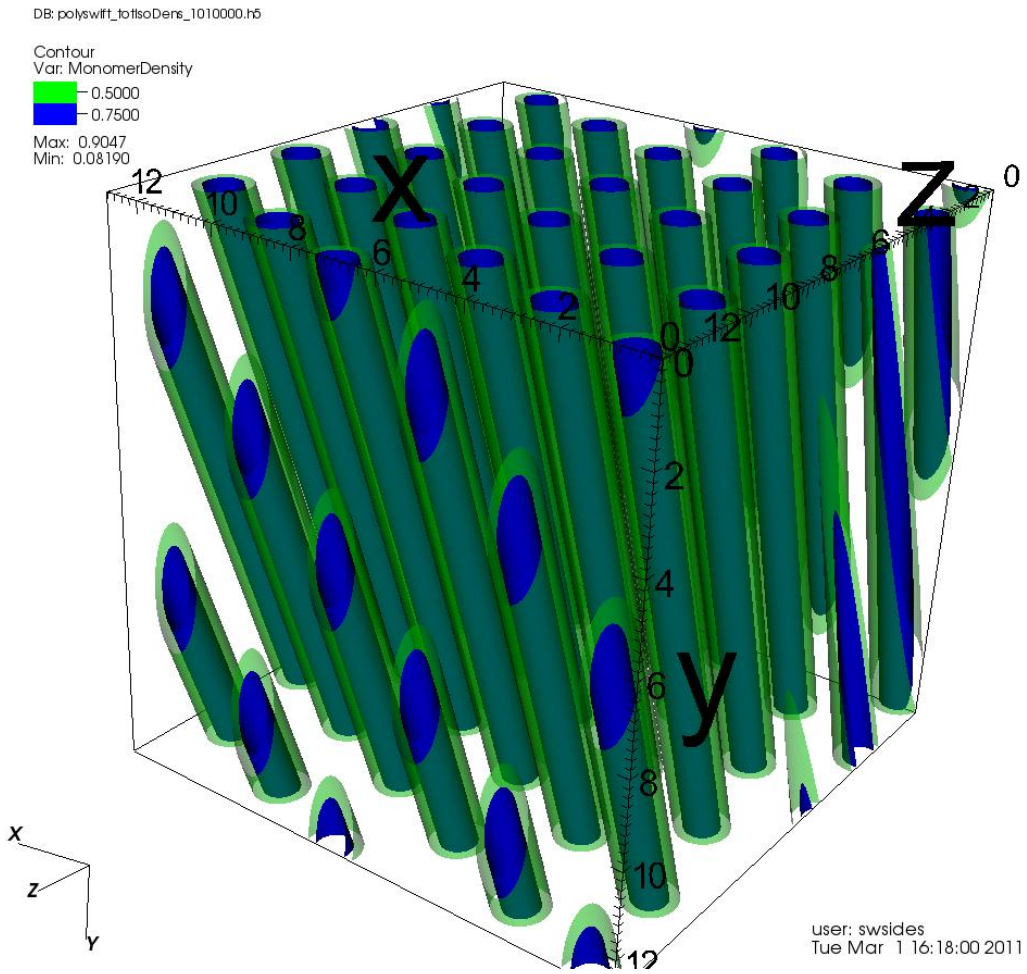

Figure 4.12. Density contours from numerical SCFT simulation of the PS_2-PI_2 diblock in bulk (PS volume fraction = 0.70 PI volume fraction = 0.30). Spectral filtering is turned on and results in the lowest free-energy among all runs performed on this sample

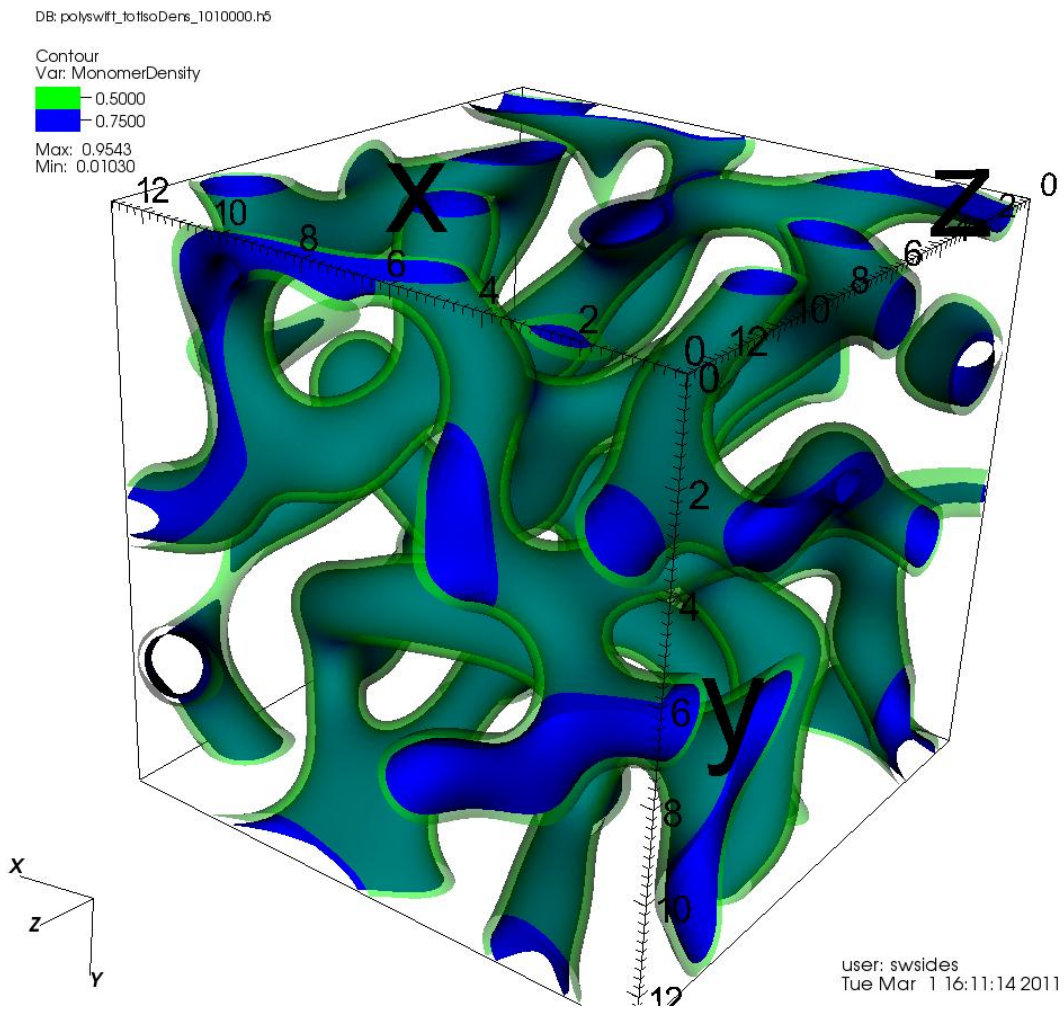

Figure 4.13. Density contours from numerical SCFT simulation of PS-PI_2 diblock in bulk (PS volume fraction = 0.74 PI volume fraction = 0.26. Spectral filtering is turned off and the morphology is not completely ordered. While the free energy of this configuration is not the lowest among all the spectral filtering runs, it is within a few percent of the lowest free-energy value obtained. This configuration is consistent with a gyroid morphology with defects.

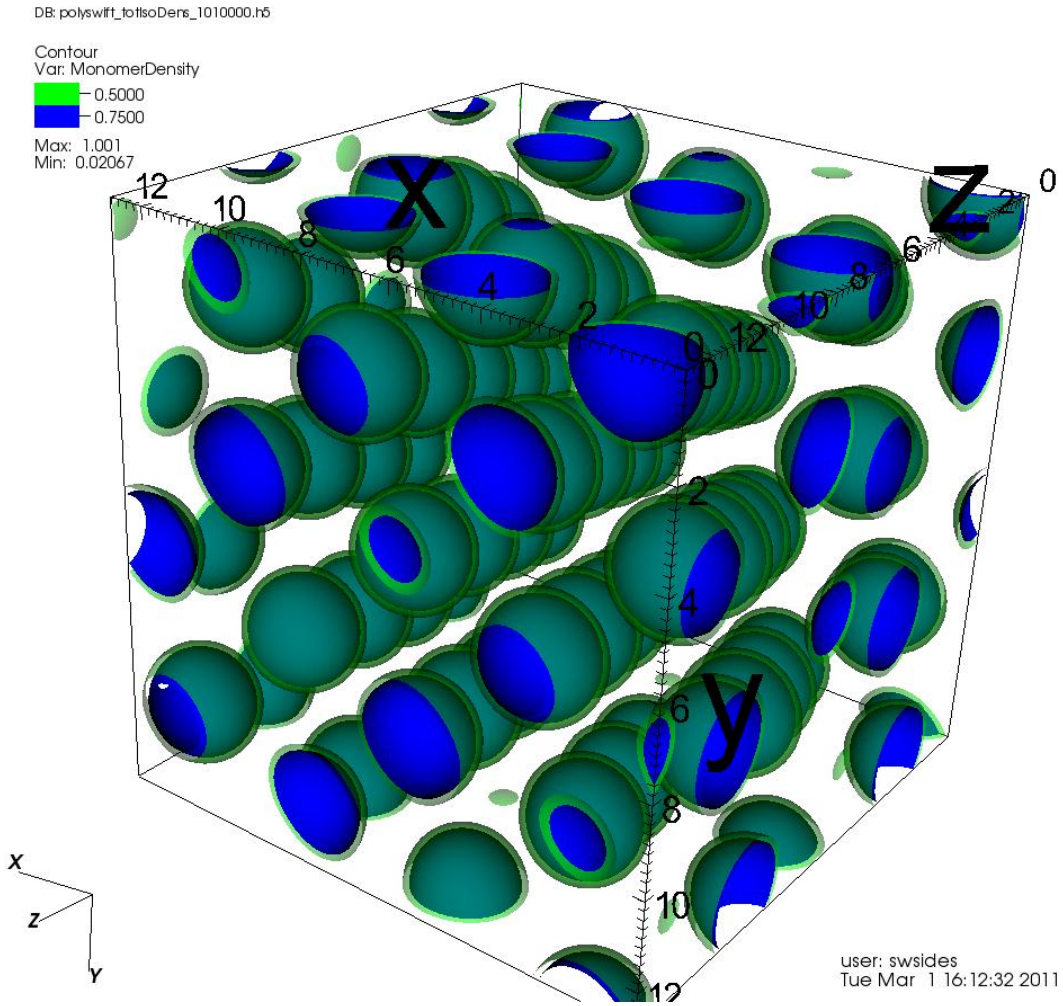

Figure 4.14. Density contours from numerical SCFT simulation of PS_2-PI diblock in bulk (PS volume fraction = 0.70 PI volume fraction = 0.30). Spectral filtering is turned on and shows well-ordered spheres. While this does not represent the lowest free-energy state, it is within a few percent of the lowest free-energy value.

Table 4.3. Morphologies observed for the four PS-PI block copolymers showing general agreement between theory, experiment and simulation.

	Experiment	**Simulation**	**Theory**
PS-b-PI	Cylinder	Cylinder	Cylinder
PS_2-PI	Spheres	Spheres	Spheres
PS-PI_2	Gyroid	Gyroid	Lamellar
PS_2-PI_2	Cylinder	Cylinder	Cylinder

arm star follows this trend, in that the size of the domain is dominated by the excluded volume of the chain pairs on each side of the interphase, resulting in significant chain stretching that minimizes the domain size reduction that results from smaller block lengths.

CHAPTER 5:FUTURE WORK AND CONCLUSIONS

5.1 Conclusion

Over the past half-century, considerable research in industrial and academic institutions has produced significant advances in understanding the variables that control the structure and properties of multi-component polymer systems. Nevertheless, many questions remain regarding the effect that one component has on the dynamics and structure of the other component in the multi-component system. This dissertation focuses on the advancement of fundamental understandings of some of the open-ended questions regarding dynamics and phase-behavior of multi-component polymer systems. The research presented here focuses on structure-property relationships, where Chapters 2 and 3 contribute to a better understanding of blending compatible polymer blends at a molecular level, and Chapter 4 provides insight into the impact of bonding schemes on the morphology of block copolymers.

A series of cellulose acetate blends are investigated where the difference in acetate substitution along the backbone of the two components is systematically increased. Small-angle neutron scattering is used to explore the miscibility of the blends indicating a decrease in miscibility as the structural differences between blend components is initially increased. This is attributed to diminishing favorable van der Waals interactions between blend components. These results indicate that the structures of the individual blend components are also an important factor in blend miscibility. Analysis of the data indicates that specific substituents can form beneficial intermolecular

interactions that promote mixing between components, which can improve miscibility even when diminishing other favorable interactions.

Thus, these results provide evidence that the ability to form beneficial specific interactions can lead to improved miscibility, where the materials with more hydroxyl substituents form these interactions, while blend components having more acetate substituents do not. One explanation is that the hydroxyls in the lower DS cellulose acetates actuate favorable hydrogen bonding. FT-IR data indicates an increase in hydrogen bonding in a blend having a cellulose acetate with more hydroxyl groups. The results, therefore, demonstrate that both variation in component substituent and the precise structure of the components impact the interactions and determine miscibility in cellulose acetate blends. These experiments highlight the role of specific non-bonding interactions and the effect of degree substitution on blend miscibility, providing detailed insight of important variables that affect phase behavior of cellulose acetate blends.
The impact of non-bonding interactions in polymer blends was further explored in Chapter 3, focusing on the role thermodynamic interactions play in polymer blend dynamics. A rheological study was completed on a series of polystyrene/PMMA homopolymer/copolymer blends, increasing the styrene content over the range of copolymer blends considered. The Arrhenius model was utilized to obtain the zero shear viscosity of a PS-*ran*-PMMA copolymer as it exists in a PMMA homopolymer matrix. These data are further analyzed to obtain the segmental friction factor of each copolymer. The results indicate that copolymer composition significantly impacts the dynamics of the random copolymer demonstrating a friction factor that falls below what is expected from a compositional average. This indicates a larger contribution from styrene than what

is suggested by stoichiometry. The Lodge-McLeish model, which predicts a self-concentration of a polymer chain based on connectivity of the polymer segments, does not quantitatively predict the experimentally determined friction factors of the copolymers; indicating the presence of other factors that influence the dynamics of these blends, for which the model does not account. Considering that the L-M predicted self-concentration is an entirely intramolecular effect (i.e. based on connectivity), we interpret this result to mean that intermolecular thermodynamic interactions significantly contribute to the copolymer dynamics. Further analysis of the L-M model indicates that there is an effective styrene concentration around the copolymer that is significantly richer than the global concentration of the blend. This explains the decrease in the monomeric friction factor of the copolymer observed in the experimentally determined friction factors.

Continuing to explore structure-property relationships of multi-component polymer systems, Chapter 4 investigates the role of connectivity on the morphology of linear and star copolymers. Block copolymers have the unique ability to order into microphase separated domains; however multiple molecular characteristics (such as molecular weight and composition) play a crucial role in determining the ordering of the microphase. The research in Chapter 4 focuses on variation of the connectivity of the blocks, which is a parameter that has only recently realized exploration. This is due, in large part, to current advances in synthetic control allowing the fabrication of well-defined copolymers of varying architectures.

This investigation combines experimental, computational and theoretical results to examine four PS-PI copolymers, holding the composition and molecular weight constant while varying the connectivity of each copolymer. The architecture varies from a linear PS-PI block copolymer, to three arm and four arm stars (PS_2-PI, PS-PI_2, and PS_2-PI_2). The experimental and computational morphological results of each copolymer are generally in good agreement. The results indicate that the excluded volume of packing multiple blocks into a domain at a junction point dominates the formations of the resultant morphologies. Specifically, introducing a branch point in the majority (PS) block in the PS_2-PI copolymer leads to the formation of a higher curvature spherical morphology whereas the linear PS-PI diblock copolymer exhibits a cylindrical morphology. The higher curvature (spherical) morphology of the PS_2-PI copolymer is the result of packing two PS chains into the matrix at a single junction point. Similarly, the introduction of a branch point in the flexible minor phase leads to a lower curvature co-continuous (gyroid) morphology as a result of packing two PI chains into the minor phase. Thus, compared to the morphology of a linear diblock copolymer with the same composition, the PS_2-PI and PS-PI_2 each form a new morphology which is governed by minimization of chain crowding at the junction point. The four arm star (PS_2-PI_2) follows this trend in that the reduction in domain size is minimized due to chain stretching at the junction point.

The experimental work featured in this dissertation focuses on advancing a fundamental understanding of structure-property relationships in multi-component polymer systems. These systems offer attractive solutions for the creation of new materials and expanded

applications, however predicting and understanding even basic properties can be challenging. The work completed in this dissertation provides a better understanding of factors that impact these properties, highlighting the role of non-bonding interactions on dynamics and miscibility of polymer blends and the effect of connectivity on the morphology of block copolymers.

5.2 Future Work

5.2.1 Cellulose Acetate Blends

The cellulose acetate blends in this study indicate that blends with a lower DS cellulose acetate (i.e. more hydroxyl groups) exhibit more hydrogen bonding thus improving miscibility, whereas blends containing higher DS cellulose acetates (i.e. more acetate groups) are governed by van der Waals interactions. The results also indicate that the van der Waals interactions become less favorable as the difference between the two components is increased, which results in increased miscibility when there is minimal hydrogen bonding between components. Testing this interplay between hydrogen bonding and van der Waals forces may lead to greater insight (and predictability) of the phase behavior of cellulose acetate blends. This can be tested using the following experimental design (and the same experimental techniques as in Chapter 2). One component in a series of blends is held constant where the constant blend component has an intermediate DS value (say a DS=2). The ΔDS of each blend is then systematically increased, such that the DS of the blend components are symmetric. In other words, two blends will each have a ΔDS=0.5 however one blend will contain components of DS=2 and 2.5 and the other blend will contain components of DS=2 and 1.5. Whereas each

blend has ΔDS=0.5, per the results in Chapter 2, the blends will have significantly different substituents and thus different interactions between blend components. Given a sufficient number of examined blends, a trend in the phase behavior should be observed, demonstrating an increase in miscibility with increasing hydroxyl content and a decrease in miscibility with decreasing hydroxyl content, for a given ΔDS. This will lead to greater understanding, potentially improving predictability of the phase behavior of these blends. There are other similar experiments that may provide further insight into the phase behavior of the blends considered here. One such experiment would follow the experimental design laid out above, however, instead of the blend component that is constant in the study having an intermediate DS, have the blend component that is constant have a higher DS (i.e. a majority of primarily acetate substituents). This experimental plan will emphasize the importance of the van der Waals interactions and their effect on phase behavior. Conversely the same experiment using a blend component that is constant with a lower DS (i.e. a majority hydroxyl substituents) will emphasize the impact of hydrogen bonding on the phase behavior of the blends. Additional experimental studies that quantify the extent of intermolecular hydrogen bonding using FTIR will also strengthen the correlation between these intermolecular interactions and blend miscibility.

5.2.2. Dynamics of Miscible Polymer Blends

The results of the dynamic studies on homopolymer/copolymer blends indicate that thermodynamic interactions between styrene and methyl methacrylate play an important role in the dynamics of these blends. Moving forward, there are two immediate pathways

where the properties elucidated in these studies may be applied. The first takes advantage of the extensive studies completed in this[3,145-147] and other labs[148,149] using copolymers as a compatibilizer in an immiscible blend. Many studies have investigated various structure-property relationships regarding the ability of a copolymer to increase interfacial strength between immiscible components. One important factor that determines a copolymer's ability to be an effective compatibilizer is how fast it can move to the interface of the phase separated components. Given the faster dynamics of the copolymers seen in this study, it would be interesting to further investigate the ability of these styrene-methyl methacrylate copolymers to diffuse through the PMMA matrix which would have implications regarding its effectiveness as a compatibilizer. One method to investigate this is fluorescence recovery after photobleaching (FRAP). In this experiment, a copolymer is tagged with a fluorescent monomer and blended with a component containing no fluorescent tags. FRAP is then used to create a "blank spot" (i.e. an area absent of fluorescent tags) in the sample and then monitors the diffusion of chains back into the blank spot by monitoring chains that still have fluorescent tags. The results presented in Chapter 3 imply that the faster dynamics of these copolymers in a PMMA matrix will improve their ability to be a compatibilizer.

The second (and less straight-forward) development that can take advantage of these findings is improving the ability of the L-M model to predict the dynamics of miscible polymer blends. As mentioned in Chapter 3, The Lodge-McLeish model ignores thermodynamic interactions, focusing instead on connectivity of the component on its dynamics. The ultimate goal of any model is to be simple and (more importantly) accurate and thus the broad success of this approach is notable and promising. For the

system employed here, however, the model must be modified and extended to be able to make quantitative predictions of ζ. An effort to modify the L-M model to fit the experimental data should be the goal of this future work. The results provided in Chapter 3 provide focus and direction when considering ways to apply this model to blends where thermodynamics play a significant role.

CHAPTER 6:LIST OF REFERENCES

References

(1)Anastasiadis, S. H.; I, G.; Koberstein, J. T. *Macromolecules* **1989**, *22*, 1449.
(2)Eastwood, E. A.; Dadmun, M. D. *Polymer* **2002**, *43*, 6707.
(3)Eastwood, E. A.; Dadmun, M. D. *Macromolecules* **2002**, *35*, 5069.
(4)Macosko, C. W.; Guegan, P.; Khandpur, A. K.; Nakayama, A.; Marechal, P.; Inoue, T. *Macromolecules* **1996**, *29*, 5590.
(5)Legge, N. R. *Rubber Chem Technol* **1987**, *60*, G83.
(6)Legge, N. R.; Holden, G. H.; Schroeder, H. E. *Eds. Thermoplastic Elastomers. Munich: Hanser* **1987**.
(7)Wellinghoff, S. T.; Koenig, J. L.; Baer, E. *Journal of Polymer Science Part B-Polymer Physics* **1977**, *15*, 1913.
(8)Shultz, A. R.; Beach, B. M. *Macromolecules* **1974**, *7*, 902.
(9)Koningsveld, R.; Kleintjens, L. A.; Schoffeleers, H. M. *Pure Appl Chem* **1974**, *39*, 1.
(10)Robeson, L. M. *Polymer blends : a comprehensive review*; Hanser: Munich ; Cincinnati, 2007.
(11)Edgar, K. J.; Buchanan, C. M.; Debenham, J. S.; Rundquist, P. A.; Seiler, B. D.; Shelton, M. C.; Tindall, D. *Prog Polym Sci* **2001**, *26*, 1605.
(12)Thummler, K. G.; Volkert, B.; Hettrich, K.; Fischer, S. *Abstr Pap Am Chem S* **2008**, *235*.
(13)Buchanan, C. M.; Gedon, S. C.; White, A. W.; Wood, M. D. *Macromolecules* **1992**, *25*, 7373.
(14)Buchanan, C. M.; Gedon, S. C.; White, A. W.; Wood, M. D. *Macromolecules* **1993**, *26*, 2963.
(15)White, A. W.; Buchanan, C. M.; Pearcy, B. G.; Wood, M. D. *J Appl Polym Sci* **1994**, *52*, 525.
(16)Ceccorulli, G.; Pizzoli, M.; Scandola, M. *Macromolecules* **1993**, *26*, 6722.
(17)Zhou, Q.; Zhang, L.; Ming, Z. B.; Wang, B.; Wang, S. J. *Polymer* **2003**, *44*, 1733.
(18)Kokot, S.; Czarnik-Matusewicz, B.; Ozaki, Y. *Biopolymers* **2002**, *67*, 456.
(19)Rao, V.; Ashokan, P. V.; Shridhar, M. H. *Polymer* **1999**, *40*, 7167.
(20)Slonimskii, G. L. *J Polym Sci* **1958**, *30*, 625.
(21)Komarek, R. J.; Gardner, R. M.; Buchanan, C. M.; Gedon, S. *J Appl Polym Sci* **1993**, *50*, 1739.
(22)Buchanan, C. M.; Gardner, R. M.; Komarek, R. J. *J Appl Polym Sci* **1993**, *47*, 1709.
(23)Buchanan, C. M.; Dorschel, D.; Gardner, R. M.; Komarek, R. J.; Matosky, A. J.; White, A. W.; Wood, M. D. *Abstr Pap Am Chem S* **1996**, *212*, 60.
(24)Aparicio, R. P.; Arbe, A.; Colmenero, J.; Frick, B.; Willner, L.; Richter, D.; Fetters, L. J. *Macromolecules* **2006**, *39*, 1060.
(25)Mukhopadhyay, R.; Alegria, A.; Colmenero, J.; Frick, B. *J Non-Cryst Solids* **1998**, *235*, 233.
(26)Genix, A. C.; Arbe, A.; Alvarez, F.; Colmenero, J.; Willner, L.; Richter, D. *Phys Rev E* **2005**, *72*.

(27)Cendoya, I.; Alegria, A.; Alberdi, J. M.; Colmenero, J.; Grimm, H.; Richter, D.; Frick, B. *Macromolecules* **1999**, *32*, 4065.
(28)Watanabe, H.; Urakawa, O. *Korea-Aust. Rheol. J.* **2009**, *21*, 235.
(29)Roovers, J.; Toporowski, P. M. *Macromolecules* **1992**, *25*, 3454.
(30)Trask, C. A.; Roland, C. M. *Macromolecules* **1989**, *22*, 256.
(31)Miller, J. B.; Mcgrath, K. J.; Roland, C. M.; Trask, C. A.; Garroway, A. N. *Macromolecules* **1990**, *23*, 4543.
(32)Chung, G. C.; Kornfield, J. A.; Smith, S. D. *Macromolecules* **1994**, *27*, 5729.
(33)Kamath, S.; Colby, R. H.; Kumar, S. K.; Karatasos, K.; Floudas, G.; Fytas, G.; Roovers, J. E. L. *Journal of Chemical Physics* **1999**, *111*, 6121.
(34)Tomlin, D. W.; Roland, C. M. *Macromolecules* **1992**, *25*, 2994.
(35)Alegria, A.; Colmenero, J.; Ngai, K. L.; Roland, C. M. *Macromolecules* **1994**, *27*, 4486.
(36)Arendt, B. H.; Kannan, R. M.; Zewail, M.; Kornfield, J. A.; Smith, S. D. *Rheol Acta* **1994**, *33*, 322.
(37)Zawada, J. A.; Fuller, G. G.; Colby, R. H.; Fetters, L. J.; Roovers, J. *Macromolecules* **1994**, *27*, 6861.
(38)Arendt, B. H.; Krishnamoorti, R.; Kornfield, J. A.; Smith, S. D. *Macromolecules* **1997**, *30*, 1127.
(39)Arbe, A.; Alegria, A.; Colmenero, J.; Hoffmann, S.; Willner, L.; Richter, D. *Macromolecules* **1999**, *32*, 7572.
(40)Hoffmann, S.; Willner, L.; Richter, D.; Arbe, A.; Colmenero, J.; Farago, B. *Phys Rev Lett* **2000**, *85*, 772.
(41)Hirose, Y.; Urakawa, O.; Adachi, K. *Macromolecules* **2003**, *36*, 3699.
(42)Chung, G. C.; Kornfield, J. A.; Smith, S. D. *Macromolecules* **1994**, *27*, 964.
(43)Min, B. C.; Qiu, X. H.; Ediger, M. D.; Pitsikalis, M.; Hadjichristidis, N. *Macromolecules* **2001**, *34*, 4466.
(44)Haley, J. C.; Lodge, T. P.; He, Y. Y.; Ediger, M. D.; von Meerwall, E. D.; Mijovic, J. *Macromolecules* **2003**, *36*, 6142.
(45)Haley, J. C.; Lodge, T. P. *Colloid Polym Sci* **2004**, *282*, 793.
(46)Lutz, T. R.; He, Y. Y.; Ediger, M. D.; Pitsikalis, M.; Hadjichristidis, N. *Macromolecules* **2004**, *37*, 6440.
(47)Kornfield, J. A.; Chung, G. C. *Abstr Pap Am Chem S* **1994**, *208*, 112.
(48)Saxena, S.; Cizmeciyan, D.; Kornfield, J. A. *Solid State Nucl Mag* **1998**, *12*, 165.
(49)Hirose, Y.; Urakawa, O.; Adachi, K. *Macromolecules* **2004**, *37*, 10215.
(50)Hirose, Y.; Urakawa, O.; Adachi, K. *Journal of Polymer Science Part B-Polymer Physics* **2004**, *42*, 4084.
(51)Lemenestrel, C.; Kenwright, A. M.; Sergot, P.; Laupretre, F.; Monnerie, L. *Macromolecules* **1992**, *25*, 3020.
(52)Pathak, J. A.; Colby, R. H.; Floudas, G.; Jerome, R. *Macromolecules* **1999**, *32*, 2553.
(53)Alegria, A.; Gomez, D.; Colmenero, J. *Macromolecules* **2002**, *35*, 2030.
(54)Leroy, E.; Alegria, A.; Colmenero, J. *Macromolecules* **2002**, *35*, 5587.
(55)Lorthioir, C.; Deloche, B.; Alegria, A.; Colmenero, J.; Auroy, P.; Gallot, Y. *Eur Phys J E* **2003**, *12*, S121.
(56)Lorthioir, C.; Alegria, A.; Colmenero, J. *Eur Phys J E* **2003**, *12*, S127.

(57)Miwa, Y.; Usami, K.; Yamamoto, K.; Sakaguchi, M.; Sakai, M.; Shimada, S. *Macromolecules* **2005**, *38*, 2355.
(58)Lutz, T. R.; He, Y. Y.; Ediger, M. D. *Macromolecules* **2005**, *38*, 9826.
(59)Lartigue, C.; Guillermo, A.; CohenAddad, J. P. *Journal of Polymer Science Part B-Polymer Physics* **1997**, *35*, 1095.
(60)Lutz, T. R.; He, Y. Y.; Ediger, M. D.; Cao, H. H.; Lin, G. X.; Jones, A. A. *Macromolecules* **2003**, *36*, 1724.
(61)Cao, H. H.; Lin, G. X.; Jones, A. A. *Journal of Polymer Science Part B-Polymer Physics* **2005**, *43*, 2433.
(62)Farago, B.; Chen, C. X.; Maranas, J. K.; Kamath, S.; Colby, R. H.; Pasquale, A. J.; Long, T. E. *Phys Rev E* **2005**, *72*.
(63)Lodge, T. P.; Wood, E. R.; Haley, J. C. *Journal of Polymer Science Part B-Polymer Physics* **2006**, *44*, 756.
(64)Tyagi, M.; Arbe, A.; Colmenero, J.; Frick, B.; Stewart, J. R. *Macromolecules* **2006**, *39*, 3007.
(65)Urakawa, O.; Ujii, T.; Adachi, K. *J Non-Cryst Solids* **2006**, *352*, 5042.
(66)Tyagi, M.; Arbe, A.; Alegria, A.; Colmenero, J.; Frick, B. *Macromolecules* **2007**, *40*, 4568.
(67)Wolak, J. E.; White, J. L. *Macromolecules* **2005**, *38*, 10466.
(68)Krygier, E.; Lin, G. X.; Mendes, J.; Mukandela, G.; Azar, D.; Jones, A. A.; Pathak, J. A.; Colby, R. H.; Kumar, S. K.; Floudas, G.; Krishnamoorti, R.; Faust, R. *Macromolecules* **2005**, *38*, 7721.
(69)Gell, C. B.; Graessley, W. W.; Fetters, L. J. *Journal of Polymer Science Part B-Polymer Physics* **1997**, *35*, 1933.
(70)Lodge, T. P.; McLeish, T. C. B. *Macromolecules* **2000**, *33*, 5278.
(71)Zhao, J. S.; Ediger, M. D. *Macromolecules* **2011**, *44*, 9046.
(72)Arrese-Igor, S.; Alegria, A.; Colmenero, J. *Macromolecules* **2010**, *43*, 6406.
(73)Bedrov, D.; Smith, G. D. *Macromolecules* **2006**, *39*, 8526.
(74)Es-Haghi, S. S.; Yousefi, A. A.; Oromiehie, A. *Journal of Polymer Science Part B-Polymer Physics* **2007**, *45*, 2860.
(75)He, Y. Y.; Lutz, T. R.; Ediger, M. D. *Journal of Chemical Physics* **2003**, *119*, 9956.
(76)He, Y. Y.; Lutz, T. R.; Ediger, M. D. *Macromolecules* **2004**, *37*, 9889.
(77)He, Y. Y.; Lutz, T. R.; Ediger, M. D.; Lodge, T. P. *Macromolecules* **2003**, *36*, 9170.
(78)He, Y. Y.; Lutz, T. R.; Ediger, M. D.; Pitsikalis, M.; Hadjichristidis, N.; von Meerwall, E. A. *Macromolecules* **2005**, *38*, 6216.
(79)Herrera, D.; Zamora, J. C.; Bello, A.; Grimau, M.; Laredo, E.; Muller, A. J.; Lodge, T. P. *Macromolecules* **2005**, *38*, 5109.
(80)Hirose, Y.; Adachi, K. *Macromolecules* **2006**, *39*, 1779.
(81)Kamath, S. Y.; Arlen, M. J.; Hamilton, W. A.; Dadmun, M. D. *Macromolecules* **2008**, *41*, 3339.
(82)Kumar, S. K.; Shenogin, S.; Colby, R. H. *Macromolecules* **2007**, *40*, 5759.
(83)Painter, P.; Coleman, M. *Macromolecules* **2009**, *42*, 820.
(84)Roland, C. M.; Casalini, R. *Macromolecules* **2007**, *40*, 3631.
(85)Zeroni, I.; Ozair, S.; Lodge, T. P. *Macromolecules* **2008**, *41*, 5033.

(86)Zhang, L.; Lutz, T. R.; Zhao, J. S.; Ediger, M. D. *Journal of Polymer Science Part B-Polymer Physics* **2007**, *45*, 2252.
(87)Liu, W. J.; Bedrov, D.; Kumar, S. K.; Veytsman, B.; Colby, R. H. *Phys Rev Lett* **2009**, *103*.
(88)Kamath, S. Y.; Dadmun, M. D. *Journal of Chemical Physics* **2006**, *125*.
(89)Milhaupt, J. M.; Lodge, T. P.; Smith, S. D.; Hamersky, M. W. *Macromolecules* **2001**, *34*, 5561.
(90)Kamath, S. Y.; Dadmun, M. D. *Macromolecular Theory and Simulations* **2005**, *14*, 519.
(91)Bates, F. S.; Fredrickson, G. H. *Annu Rev Phys Chem* **1990**, *41*, 525.
(92)Russell, T. P. *Curr Opin Colloid In* **1996**, *1*, 107.
(93)Bates, F. S.; Fredrickson, G. H. *Phys Today* **1999**, *52*, 32.
(94)Bi, L. K.; Fetters, L. J. *Macromolecules* **1976**, *9*, 732.
(95)Hadjichristidis, N.; Roovers, J. *Journal of Polymer Science Part B-Polymer Physics* **1978**, *16*, 851.
(96)Falk, J. C.; Schlott, R. J.; Hoeg, D. F. *J Macromol Sci Chem* **1973**, *A 7*, 1647.
(97)Falk, J. C.; Schlott, R. J. *J Macromol Sci Chem* **1973**, *A 7*, 1663.
(98)Falk, J. C.; Hoeg, D. F.; Schlott, R. J.; Pendleto.Jf *J Macromol Sci Chem* **1973**, *A 7*, 1669.
(99)Falk, J. C.; Schlott, R. J.; Hoeg, D. F.; Pendleto.Jf *Rubber Age* **1973**, *105*, 52.
(100)Falk, J. C.; Schlott, R. J.; Hoeg, D. F.; Pendleton, J. F. *Rubber Chem. Technol.* **1973**, *46*, 1044.
(101)Pitsikalis, M.; Pispas, S.; Mays, J. W.; Hadjichristidis, N. *Adv Polym Sci* **1998**, *135*, 1.
(102)Mays, J. W. *Polym Bull* **1990**, *23*, 247.
(103)Iatrou, H.; Hadjichristidis, N. *Macromolecules* **1992**, *25*, 4649.
(104)Iatrou, H.; Hadjichristidis, N. *Macromolecules* **1993**, *26*, 2479.
(105)Iatrou, H.; Siakalikioulafa, E.; Hadjichristidis, N.; Roovers, J.; Mays, J. *Journal of Polymer Science Part B-Polymer Physics* **1995**, *33*, 1925.
(106)Pispas, S.; Pitsikalis, M.; Hadjichristidis, N. *Abstr Pap Am Chem S* **1997**, *213*, 5.
(107)Beyer, F. L.; Gido, S. P.; Buschl, C.; Iatrou, H.; Uhrig, D.; Mays, J. W.; Chang, M. Y.; Garetz, B. A.; Balsara, N. P.; Tan, N. B.; Hadjichristidis, N. *Macromolecules* **2000**, *33*, 2039.
(108)Lee, C.; Gido, S. P.; Poulos, Y.; Hadjichristidis, N.; Tan, N. B.; Trevino, S. F.; Mays, J. W. *Polymer* **1998**, *39*, 4631.
(109)Lee, C.; Gido, S. P.; Pitsikalis, M.; Mays, J. W.; Tan, N. B.; Trevino, S. F.; Hadjichristidis, N. *Macromolecules* **1997**, *30*, 3732.
(110)Lee, C.; Gido, S. P.; Poulos, Y.; Hadjichristidis, N.; Tan, N. B.; Trevino, S. F.; Mays, J. W. *Journal of Chemical Physics* **1997**, *107*, 6460.
(111)Hadjichristidis, N.; Iatrou, H.; Behal, S. K.; Chludzinski, J. J.; Disko, M. M.; Garner, R. T.; Liang, K. S.; Lohse, D. J.; Milner, S. T. *Macromolecules* **1993**, *26*, 5812.
(112)Pochan, D. J.; Gido, S. P.; Pispas, S.; Mays, J. W.; Ryan, A. J.; Fairclough, J. P. A.; Hamley, I. W.; Terrill, N. J. *Macromolecules* **1996**, *29*, 5091.
(113)Milner, S. T. *Macromolecules* **1994**, *27*, 2333.
(114)Bates, F. S.; Berney, C. V.; Cohen, R. E. *Macromolecules* **1983**, *16*, 1101.

(115)Helfand, E.; Wasserman, Z. R. *Macromolecules* **1976**, *9*, 879.
(116)Hashimoto, T.; Todo, A.; Itoi, H.; Kawai, H. *Macromolecules* **1977**, *10*, 377.
(117)Whistler, R. L.; Wolfrom, M. L.; BeMiller, J. N. *Methods in carbohydrate chemistry*; Academic Press: New York,, 1962.
(118)Buchanan, C. M.; Edgar, K. J.; Hyatt, J. A.; Wilson, A. K. *Macromolecules* **1991**, *24*, 3050.
(119)Buchanan, C. M.; Edgar, K. J.; Wilson, A. K. *Macromolecules* **1991**, *24*, 3060.
(120)Higgins, J. S.; Benoît, H. *Polymers and neutron scattering*; Clarendon Press ; Oxford University Press: Oxford
New York, 1994.
(121)Roe, R. J. *Methods of X-ray and neutron scattering in polymer science*; Oxford University Press: New York, 2000.
(122)Lynn, G. W.; Heller, W.; Urban, V.; Wignall, G. D.; Weiss, K.; Myles, D. A. A. *Physica B* **2006**, *385-86*, 880.
(123)Bledzki, A. K.; Reihmane, S.; Gassan, J. *J Appl Polym Sci* **1996**, *59*, 1329.
(124)Rosato, D. V.; Rosato, D. V.; Society of Plastics Engineers. Injection Molding Division. *Injection molding handbook : the complete molding operation : technology, performance, economics*; Van Nostrand Reinhold: New York, 1986.
(125)Gardner, K. H.; Blackwel.J *Biochim Biophys Acta* **1974**, *343*, 232.
(126)Yin, J. H.; Xue, C.; Alfonso, G. C.; Turturro, A.; Pedemonte, E. *Polymer* **1997**, *38*, 2127.
(127)Wu, H. D.; Chu, P. P.; Ma, C. C. M.; Chang, F. C. *Macromolecules* **1999**, *32*, 3097.
(128)Rasheed, A.; Dadmun, M. D.; Ivanov, I.; Britt, P. F.; Geohegan, D. B. *Chem Mater* **2006**, *18*, 3513.
(129)San Roman, A. M., E.L.; Del Puerto, M.A. *Macromol. Chem.* **1980**, *86*, 1.
(130)Fetters, L. J.; Lohse, D. J.; Milner, S. T.; Graessley, W. W. *Macromolecules* **1999**, *32*, 6847.
(131)Doi, M.; Edwards, S. F. *The theory of polymer dynamics*; Clarendon Press ; Oxford University Press: Oxford [Oxfordshire]
New York, 1986.
(132)Ferry, J. *Viscoelastic properties of polymers*; 3d ed.; Wiley: New York, 1980.
(133)Friedman, E. M.; Porter, R. S. *T Soc Rheol* **1975**, *19*, 493.
(134)Gisser, D. J.; Ediger, M. D. *J Phys Chem-Us* **1993**, *97*, 10818.
(135)Stockmayer, W. H.; Kennedy, J. W. *Macromolecules* **1975**, *8*, 351.
(136)Haley, J. C.; Lodge, T. P. *J Rheol* **2004**, *48*, 463.
(137)Hadjichristidis, N.; Pispas, S.; Floudas, G. *Block copolymers : synthetic strategies, physical properties, and applications*; Wiley-Interscience: Hoboken, N.J., 2003.
(138)Uhrig, D.; Mays, J. W. *J Polym Sci Pol Chem* **2005**, *43*, 6179.
(139)Hadjichristidis, N.; Iatrou, H.; Pispas, S.; Pitsikalis, M. *J Polym Sci Pol Chem* **2000**, *38*, 3211.
(140)Fredrickson, G. H.; Ganesan, V.; Drolet, F. *Macromolecules* **2002**, *35*, 16.
(141)Sides, S. D.; Fetter, N. L.; Glisson, R.; Nunley, J. A. *Foot Ankle Int* **2006**, *27*, 821.
(142)Fetters, L. J.; Lohse, D. J.; Richter, D.; Witten, T. A.; Zirkel, A. *Macromolecules* **1994**, *27*, 4639.

(143)Beyer, F. L.; Gido, S. P.; Velis, G.; Hadjichristidis, N.; Tan, N. B. *Macromolecules* **1999**, *32*, 6604.
(144)*http://lammps.sandia.gov/*.
(145)Arlen, M. J.; Dadmun, M. D. *Polymer* **2003**, *44*, 6883.
(146)Eastwood, E.; Viswanathan, S.; O'Brien, C. P.; Kumar, D.; Dadmun, M. D. *Polymer* **2005**, *46*, 3957.
(147)Ashcraft, E.; Ji, H. N.; Eastwood, E.; Mays, J.; Dadmun, M. *Abstr Pap Am Chem S* **2011**, *242*.
(148)Galloway, J. A.; Jeon, H. K.; Bell, J. R.; Macosko, C. W. *Polymer* **2005**, *46*, 183.
(149)Ajji, A.; Utracki, L. A. *Polym Eng Sci* **1996**, *36*, 1574.

APPENDIX

A.1. ρ calculation of Deuterated Cellulose Acetate Copolymer

When calculating the ρ of the deuterated component, it is important to keep in mind the experimental details and specific atomistic changes thereof. Synthesis of the deuterated material started with a fully deuterated triacetate and was hydrolyzed with a protonated hydroxyl group. Thus the calculation of ρ for the deuterated CA, having a DS of 2.19, considers 100 repeat units where 19 are a fully deuterated triacetate (DS=3) and 81 repeat units are a diacetate having two deuterated acetate groups and one protonated hydroxyl group (DS=2), averaging out to have a DS of 2.19. This is significant due to the large difference in scattering length between deuterium and hydrogen and this consideration substantially impacts the overall results.

A.2. SANS Data at Different Temperatures

The temperature ranges used in this study are room temperature (RT), 50°C, 100°C, and 150°C (excluding the 33hr blend which was not measured at RT). Figures A-1 through A-5 are the scattering curves for each sample at different temperatures. Generally, each temperature displayed overlap with other temperatures effectively indicating that there was no change in miscibility at temperatures considered. Figure A-6 is Chi as a function of temperature for each blend. The change in Chi is within error indicating that, for the temperature range used in this experiment, Chi is temperature independent. The Flory interaction parameter is often written as the sum of two terms:

$$\chi(T) \cong A + \frac{B}{T}$$

Where the temperature-independent term A is referred to as the entropic part of χ, and B/T is the enthalpic part. The temperature independence of Chi suggest the major

contribution of this system is seen in the temperature-independent A parameter. This indicates that the system is entropically driven.

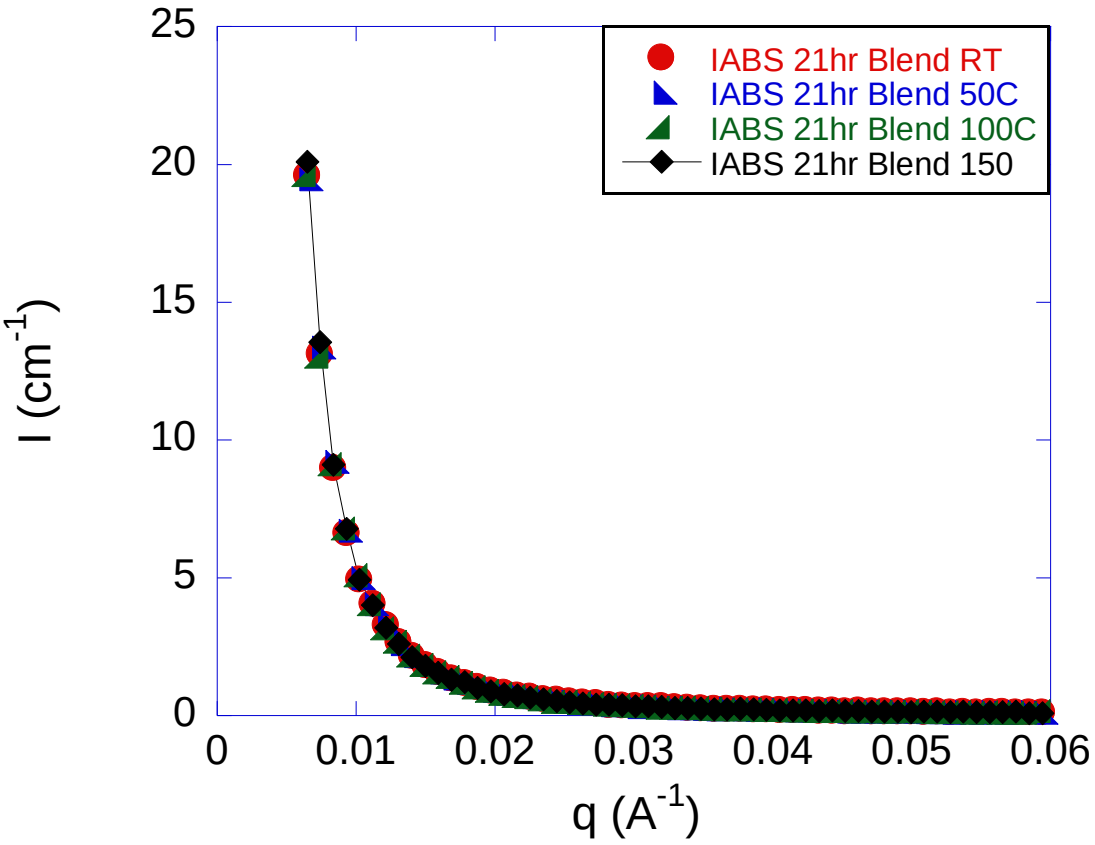

Figure A. 1. 21hr blend SANS data for all temperatures

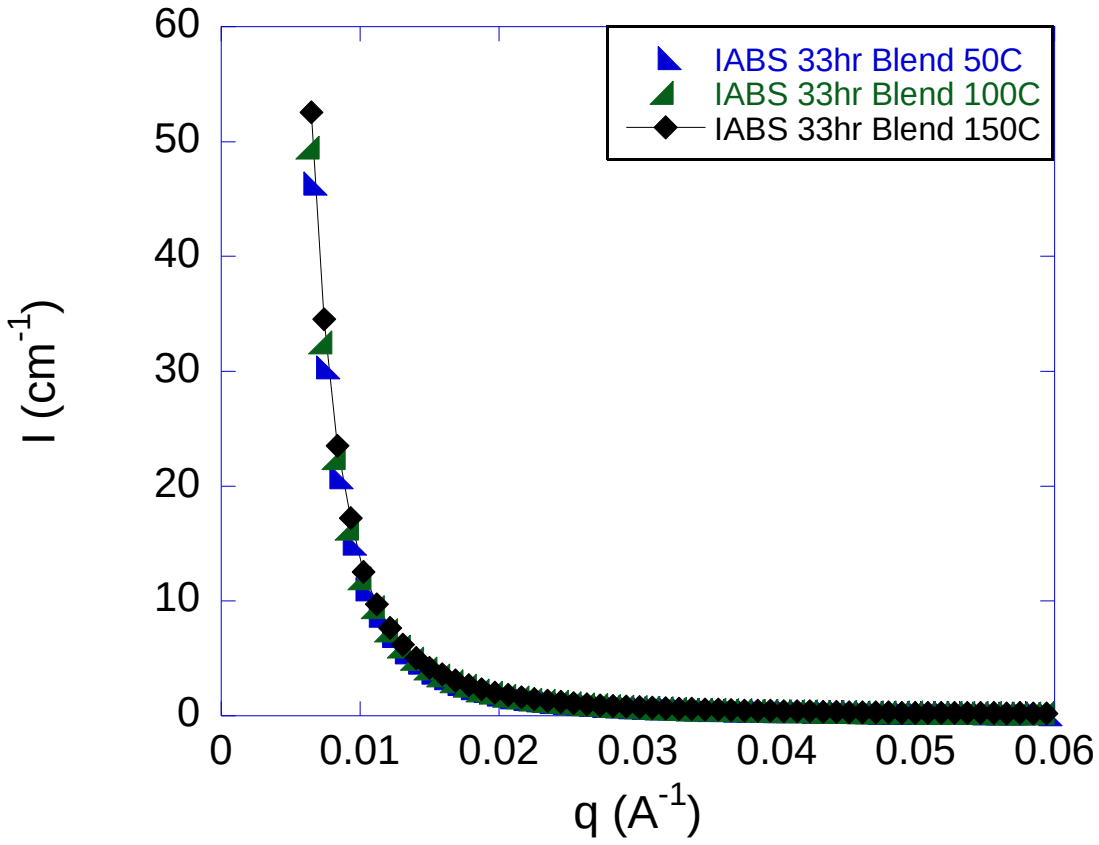

Figure A. 2. 33hr SANS data for all temperatures

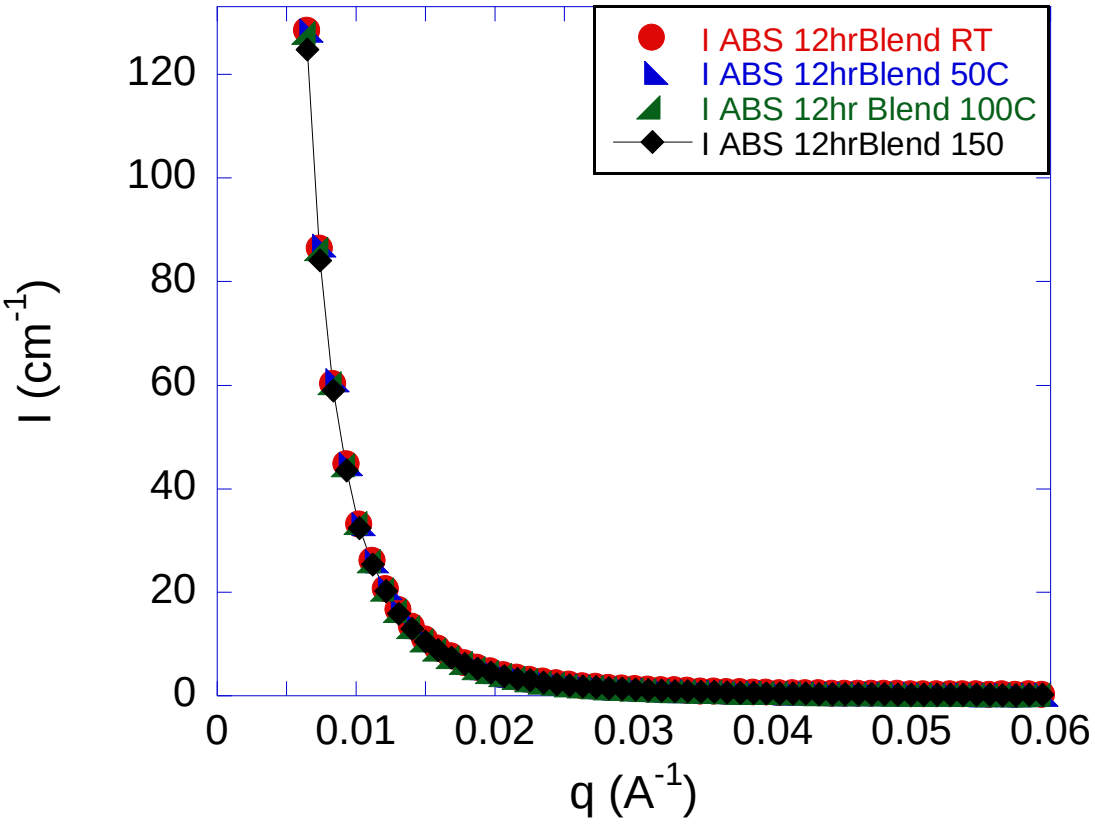

Figure A. 3. 12hr SANS data for all temperatures

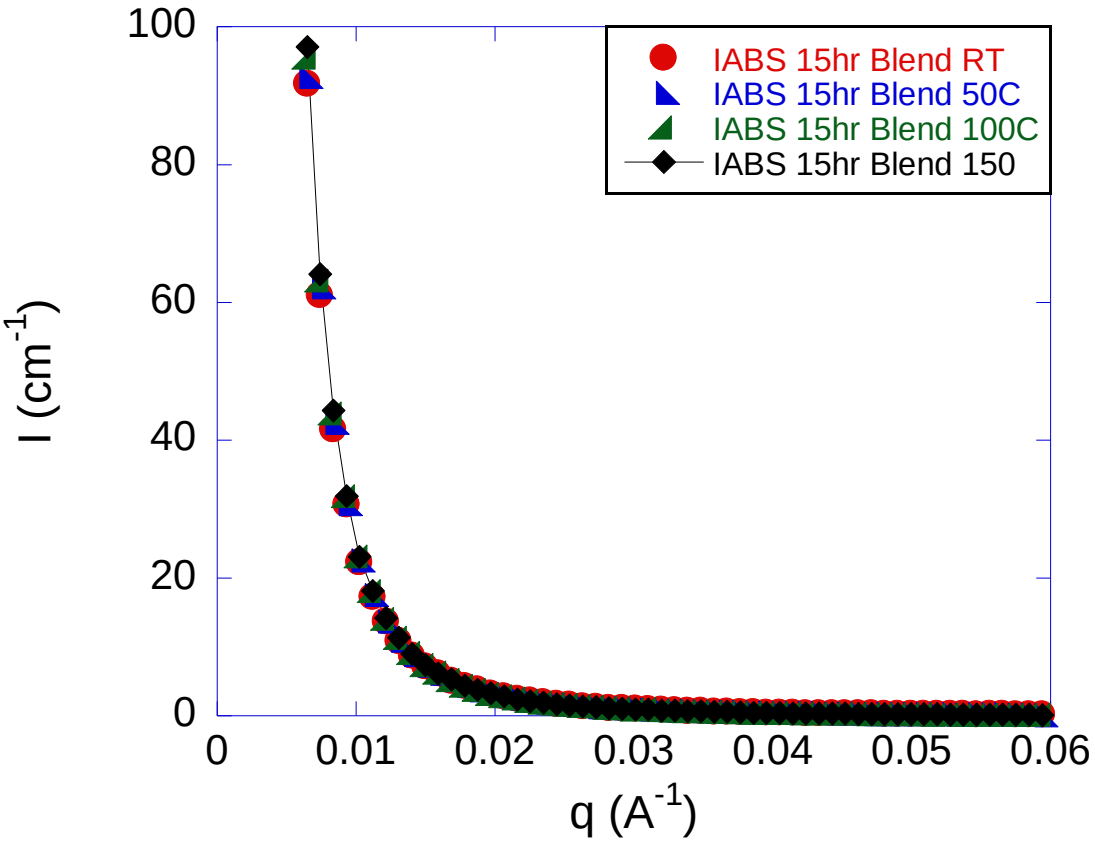

Figure A. 4. 15hr SANS data for all temperatures

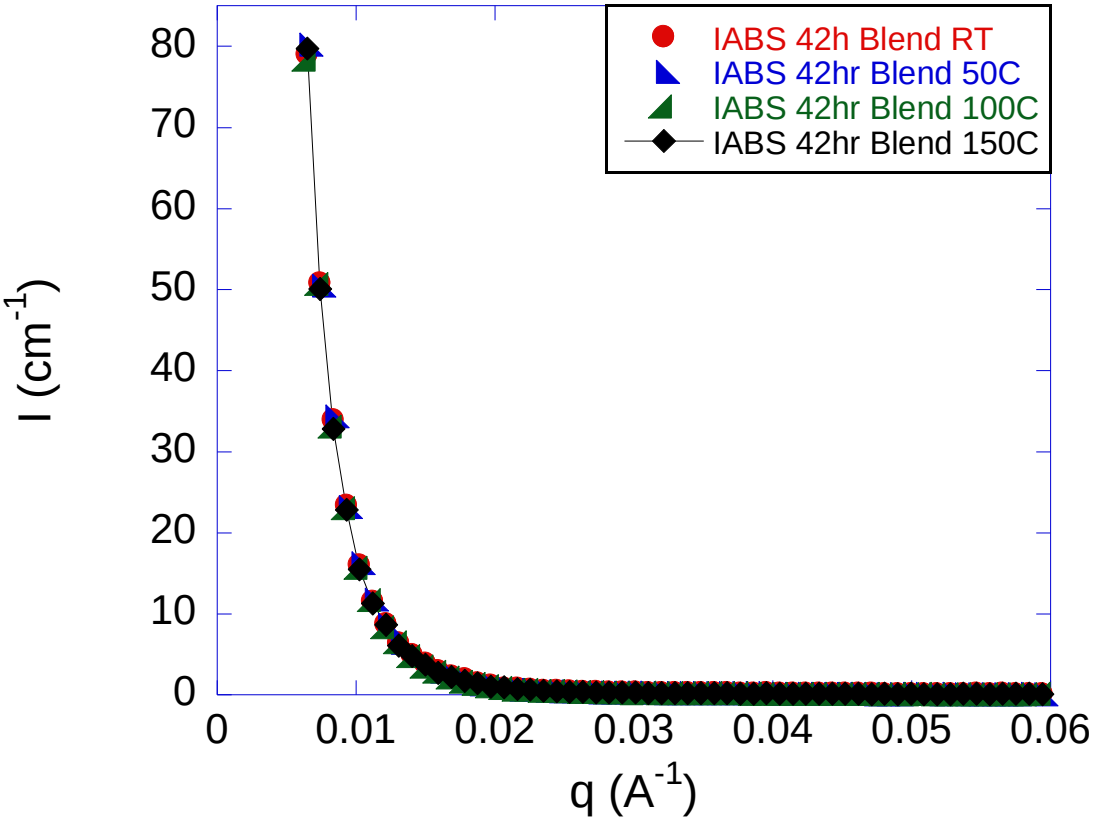

Figure A. 5. 42hr SANS data for all temperatures

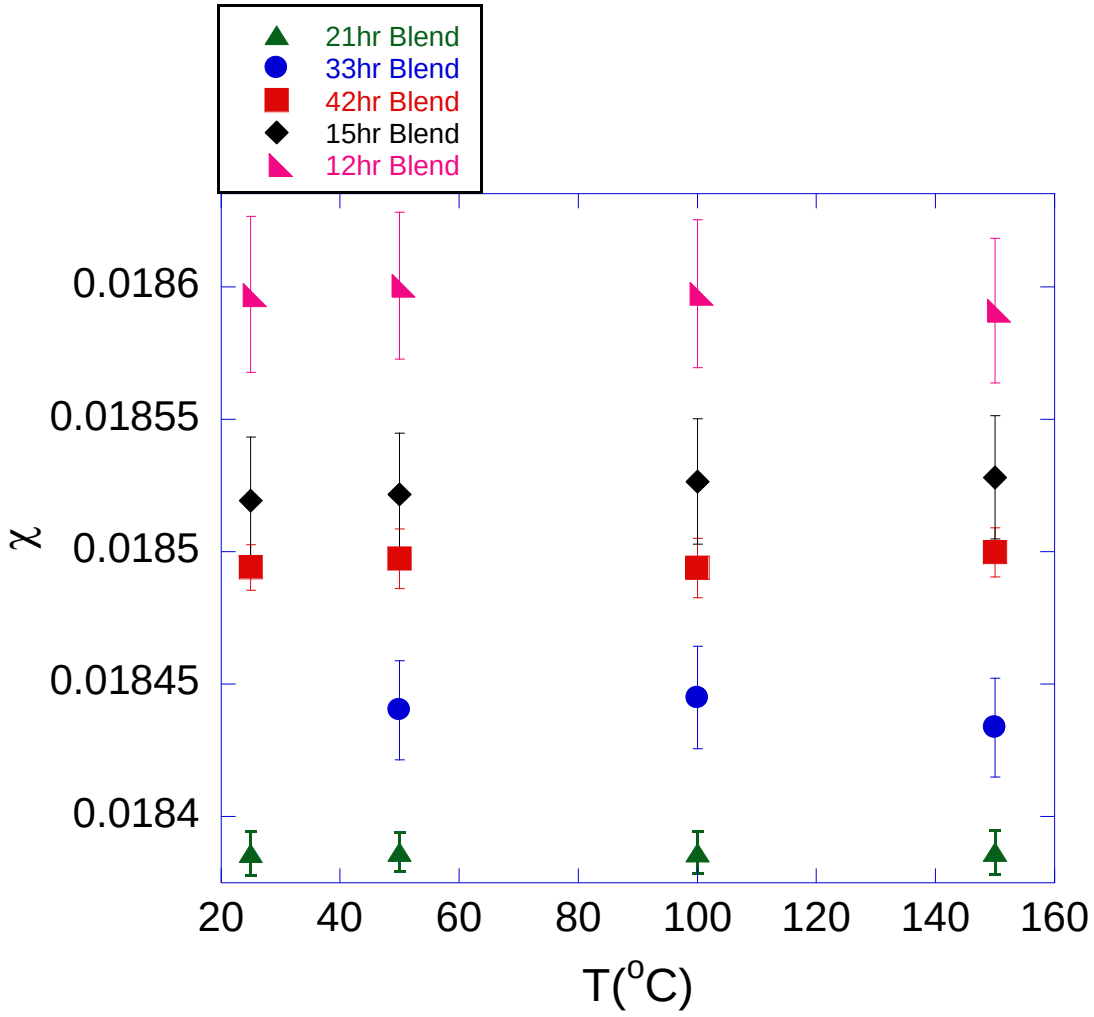

Figure A. 6. χ values for each cellulose acetate sample at each temperature

A.3. ^{1}H NMR Determination of Random Copolymer Composition

The copolymer composition for PS-*ran*-PMMA copolymers were determined by ^{1}H NMR Spectroscopy (Varian 300MHz). A typical spectra is shown in Figure A.1. For PMMA and PS there are 8 protons for each monomer. The normalized area per proton of the PMMA and PS are then given by

$$A_{PMMA} = \frac{Area\ of\ peak\ .5-4.0\ (5.68)}{8\ protons}$$

and

$$A_{PS} = \frac{Area\ of\ peaks\ 6.0-7.5\ (1.00)}{8\ protons}$$

The composition of the PS-*ran*-PMMA copolymers are determined by comparing the area under the non-aromatic PMMA peaks (6.0-7.5ppm) to the area of the aromatic PS peaks (.5-4.0ppm) as shown in Figure A.1. For PS-PMMA copolymer there are 5 aromatic hydrogens (denoted a-e in Figure A.1) and 3 non-aromatic hydrogens from styrene (f and g) therefore the area under the peak of the aromatic peak is divided by 5. The three non-aromatic peaks from styrene are subtracted from the non-aromatic region. %MMA is then given by

$$\text{mol\%PMMA} = \frac{A_{PMMA} - \frac{3}{5}A_{PS}\ (.71-.075)}{A_{PMMA}+A_{PS}\ (.71+.125)} \times 100\% = 76.04\%$$

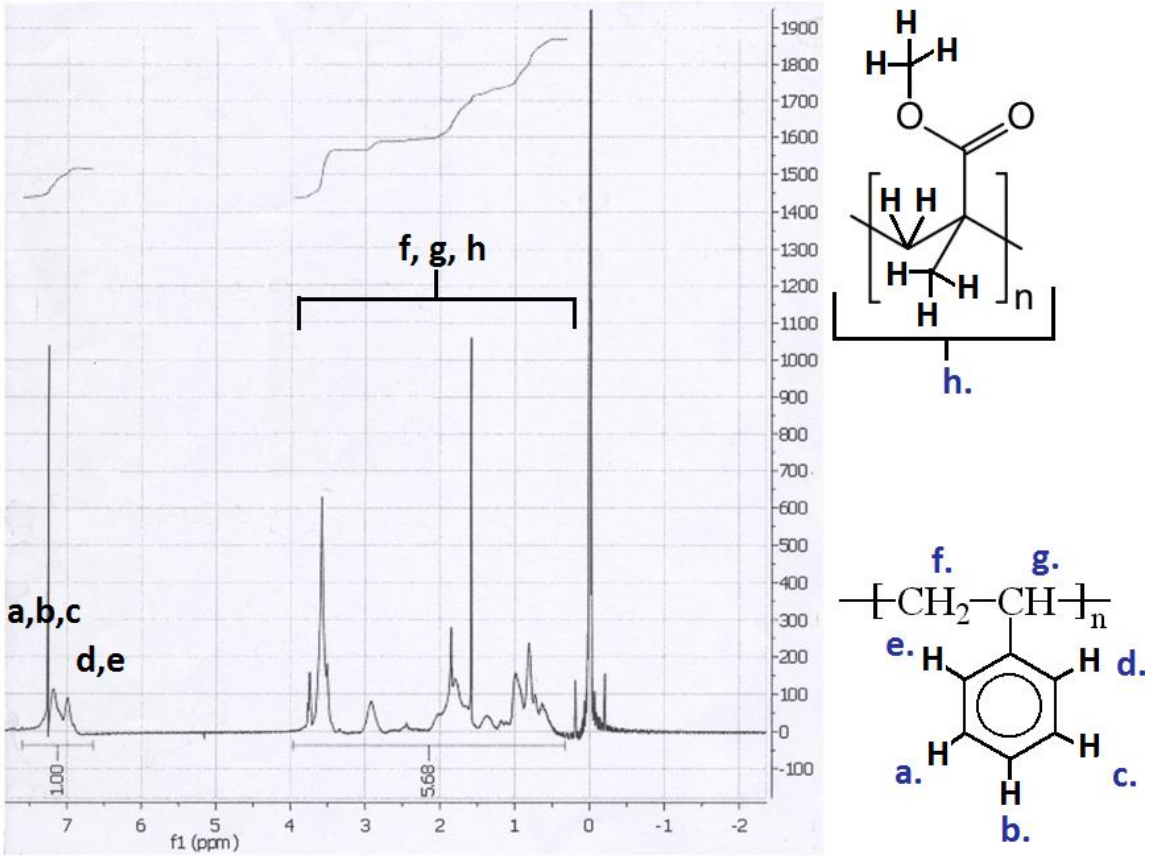

Figure A. 7. Typical ^{1}H NMR spectra of PMMA-*ran*-PS

VITA

Caleb Dyer was born on March 13th 1983 and grew up in the small town of Blairsville, Georgia. In May of 2001 he graduated from Union County High School. He attended Georgia College and State University from August 2001 to May 2005 where he received a B.S. in Chemistry with a minor in Spanish. In August 2005 he moved to Knoxville, TN to continue his graduate career with a specialization in Polymer Chemistry, under the direction of Professor Mark Dadmun. He successfully defended his Ph.D. dissertation in July of 2012. On July 9th 2012, he began work as a materials research scientist in the Polymer R&D division at Nike in Portland, Oregon.